Elasticity of polymers investigated by atomic-force microscopy

INAUGURALDISSERTATION

zur

Erlangung der Würde eines Doktors der Philosophie

vorgelegt der

Philosophisch-Naturwissenschaftlichen Fakultät

der Universität Basel

von

Alexander Bubendorf

aus Oberwil (BL)

Basel, 2017

Genehmigt von der Philosophisch-Naturwissenschaftlichen Fakultät

auf Antrag von:

Prof. Dr. Ernst Meyer
Prof. Dr. Martino Poggio

Basel, den 10 november 2015

Prof. Dr. Jörg Schibler, Dekan

Abstract

The elasticity of four different polymers, polystyrene (PS), polypropylene (PP), polytetrafluoroethylene (PTFE) and linear low-density polyethylene (LLDPE), and a self-assembled monolayer (SAM) of 1H,1H,2H,2H-perfluorodecyltrichlorosilane (FDTS) on a silicon oxide substrate perforated with circular holes prepared by polymer blend lithography was investigated by atomic force microscopy (AFM) by using two different methods: a static and a dynamic method, under nondry-air conditions and at ambient temperature. In the static method based on the method developed by Oliver and Pharr for rigid indenters [J. Mater. Res. 1992, 7, 1564−1583], the elastic modulus is determined from load-displacement curves obtained from indentations of the cantilever tip in the sample surface. The origin of the observed plastic and elastic deformation phases is explained. As indentations performed by cantilever tips differ from those done by rigid indenters, parameters, such as creep of the piezoelectric scanner, cold flow, thermal expansion of the sample and finite stiffness of the cantilever were investigated to make the results fit the theoretical model of Oliver and Pharr. The method was tested on PTFE and PS. In the dynamic method based on the AFM method devised by Herruzo et al. [Nat. Commun. 2014, 5, 3126], a more robust measurement method than the initial one is used to determine the frequency shifts necessary to compute the elastic modulus of samples. This method, that is based on the tracking of the two first flexural contact resonances, is especially well suited when measuring in ambient conditions. The normal force necessary for the measurements was assessed. The origin of the observed plastic and elastic deformation phases and the effect of the spring constant on the relation between the measured normal force and the displacement of the Z piezoelectric scanner in these phases are explained. The method was tested on LLDPE, PP, PS and the SAM. The storage modulus of LLDPE, PP, PS and FDTS was determined. The values for LLDPE, PP, and PS where compared with Young's modulus for bulk material. The value of the storage modulus for FDTS can be used as an estimation for the order of magnitude of Young's modulus of an FDTS monolayer. The measurements were performed with two controllers for scanning probe microscopes (SPM): Nanonis, a commercial controller from Specs (Zurich, Switzerland), and SAPHYR, whose hardware was developed by the Electronics Department of the Department of Physics of the University of Basel (Basel, Switzerland) in collaboration with Nanosurf (Liestal, Switzerland), a company specialized in SPM. The full software for the control of the different modules of SAPHYR was programmed in the LabVIEW environment during this work. The functions necessary to perform elasticity measurements with Oliver and Pharr's methods, but also to perform AFM imaging in general, were implemented. These functions are a Z controller for the control of the tip-sample surface distance, a scanner that can map all the necessary quantities (phase shifts, frequency shifts, dissipation, ...) and a Z spectroscopy function that can measure load-displacement curves. The initial method for the computation of phase shifts between an excitation signal and the cantilever response signal with SAPHYR lockin amplifiers was replaced by a more powerful algorithm developed by the

author. In the initial method, the phase shift was determined from the real-time computation of ratio $\frac{Y}{X}$ of the quadrature Y by the in-phase X components in the SAPHYR controller and the computation of $arctan(\frac{Y}{X})$ by the software for the control of SAPHYR. This algorithm, can compute $arctan(\frac{Y}{X})$ directly and precisely in the SAPHYR lockin amplifiers in real time. In addition, the algorithm overcomes the instabilities of the functioning of the initial phase-locked loops (PLLs) in SAPHYR based on the use of the approximation $arctan(\frac{Y}{X}) \simeq \frac{Y}{X}$ as a phase shift value, and due to magnitudes of phase shift and its variations greater than $0°$, that occur, for example, when the cantilever tip picks up material or the sample surface elastic properties change. As this method is a good solution for the actual state of the art of the lockin and PLL development for AFM, my proposition for its patenting was accepted by the University of Basel. Finally, an analytical expression for the computation of the normal contact stiffness of a clamped cantilever with its tip in contact with the sample surface was established. This formula, derived from the equations based on Rabe's work and published by Hurley and Turner in J. Appl. Phys. 2007, 102, 033509, avoids the usual numerical determination of normal contact stiffness by the extrapolation method.

Contents

List of abbreviations

AC:	Alternating current
AFM:	Atomic-force microscopy / atomic-force microscope
ADC:	Analog-digital converter
AM:	Amplitude modulation
BNC:	Bayonet Neill-Concelman
DAC:	Digital analog converter
DC:	Direct current
FDTS:	1H,1H,2H,2H-perfluorodecyltrichlorosilane
FM:	Frequency modulation
FM-AFM:	Frequency modulation atomic-force microscopy
FPGA:	Field programmable gate array
I/O:	Input/output
LLDPE:	Linear low-density polyethylene
NCO:	Numerically controlled oscillator
PBL:	Polymer blend lithography
PI:	Proportional integral
PLL:	Phase-locked loop
PM-AFM:	Phase modulation atomic-force microscopy
PP:	Polypropylene
PS:	Polystyrene
PTFE:	Polytetrafluoroethylene also called Teflon
SAM:	Self-assembled monolayer
SiOx:	Silicon oxide
SPM:	Scanning probe microscopy / scanning probe microscope
UI:	User's interface

Introduction

The elaboration of materials resistant to external elastic stresses is a need of utmost importance in everyday life. For instance the resistance of a material insures that a building resists during earthquakes or winds or that a plane keeps its shape despite the air pressure during a flight. This resistance to elastic stresses is called elastic modulus. At the nanoscale, knowledge of the local elasticity of samples is of high interest in many scientific domains, as many processes and physical quantities are correlated with the elastic modulus. In biology, for instance, studies showed that the elasticity of cells depends on their age, the stage of the cell cycle and the degree of differentiation [5]. In physics, the band gap size of nanocrystals and the presence of planar defects on nanotubes are a function of the elastic modulus [6, 7]. Probing local elasticity requires an instrumentation capable of operating with high resolution and under different conditions, such as variable temperature, pressure or humidity. Since its invention, the atomic force microscope (AFM) [8] has confirmed its value for locally determining nanomechanical properties, such as the elastic modulus, on sample surface. Initially, the measures were done qualitatively, with the cantilever operated in intermittent-contact mode by showing the phase shift contrast between regions with different elasticities [9], then quantitatively by various static and dynamic methods [10, 11]. Although the results obtained with these methods are in good agreement with theoretical data and data obtained from macroscopic experiments, difficulties in precisely determining the elastic modulus based on the theoretical model or in using the method may be encountered with dynamic mode AFM as is the case with the methods devised by Hurley and Turner [10] and Herruzo et al. [11]. In Hurley and Turner's [10] method, the stated equations for the computation of normal sample stiffness by numerical methods (analytical expression for normal sample stiffness formulated in appendix D) used to determine sample elasticity are based on the equations established by Rabe [12] and Rabe et al. [13] for atomic force acoustic microscopy (AFAM) [14–17] and describing the dynamics of a clamped cantilever elastically coupled with the sample surface at its tip end. These equations have the disadvantage of strongly depending on the dimensions of an ideal beam-shaped cantilever, which, however, differs from most cantilevers used for measurements. Thus, to achieve consistent results, the lengths and tip height have to be corrected. As to the multifrequency AFM [18, 19] method of Herruzo et al. which is based on the excitation of two cantilever eigenmodes [20–24], when the measurements are performed in nondry air, the instability of the tip-sample distance feedback loop, due to the use of frequency shift as control parameter, makes its application difficult if not impossible. However, despite these disadvantages, both methods are particularly interesting because of the complementarity of their advantages. The method of Hurley and Turner [10], which is based on tracking the first flexural and torsional contact resonances has the advantage of staying stable even if the measurements are performed in nondry air; in contrast, the method of Herruzo et al. [11] uses a simple theoretical model that depends only weakly on the dimensions of the cantilever. A new dy-

namic method for measuring a sample's elastic modulus that combines the simplicity of the theoretical model of Herruzo et al. [11] with the robustness of the measuring method based on contact resonances is presented in the present work. In 1992, Oliver and Pharr [25] published a reference article describing an improved method to determine the elastic modulus of a sample from a load-displacement curve obtained by indentation with a rigid indenter. Due to their shape, AFM cantilever tips are well suited to perform nanoindentations and hence to locally determine the elastic modulus of a sample by Oliver and Pharr's method. Additionally to the previous AFM-based method for the determination of the elastic modulus of samples, a study of the applicability of Oliver and Pharr's method to load-displacement curves obtained with cantilever tip indentation was undertaken. A controlling electronic system is mandatory to perform AFM experiments. Signals must be generated to move the cantilever over the sample, keep the cantilever tip at a certain distance from the sample surface or simply excite the cantilever. Moreover, electronic devices such as lockin amplifiers and PLLs for the treatment of excitation and response signals of the cantilever are required to extract information (frequency shift, cantilever oscillation amplitude, phase shift) from the response signal and adjust it to fit the parameters of theoretical models for the determination of interaction forces but also physical characteristics of samples such as elasticity. In 2008, the SAPHYR controller stemmed from a common project jointly devised by the Nanolino group of the Department of Physics of the University of Basel (Switzerland) and Nanosurf, based in Liestal (Switzerland) and specialized in scanning probe microscopy (SPM). At the beginning of the present work, the computation of the phase shift between the excitation signal and the response signal of the cantilever in SAPHYR was performed by computing ratio $\frac{Y}{X}$ of the quadrature Y to the in-phase X components in real time by a lockin amplifier and $arctan(\frac{Y}{X})$ with the software for the control of SAPHYR. The lockin-based PLLs in SAPHYR used the approximation $arctan(\frac{Y}{X}) \sim \frac{Y}{X}$ to determine the phase necessary for the computation of the frequency shift in real time. The problem with this approximation is that it restrains phase variations to values around 0°. Hence, the functioning of the PLL stays stable as long as no perturbation occurs. Perturbations (for example, when the cantilever picks up materials on the sample surface in FM-AFM or in case of large changes in material properties when measuring contact resonances) result in a large phase shift variation, far from 0°. In this case, due to the approximation, the error in the measured phase shift leads to the computation of erroneous frequency shift values. To overcome this drawback, a new algorithm was developed in the frame of this research and is summarized in the present work. Moreover, the initial software for the control of SAPHYR based on C++ language was incomplete and unable to perform mappings or elasticity measurements. Thus, a new software for the control of SAPHYR, programmed in LabVIEW environment, that can be used for mapping sample topography and performing elasticity measurement is proposed.

Chapter 1

Atomic Force Microscopy

In 1982, Binnig and Rohrer revolutionized the surface science and microscopy with the invention of the scanning tunneling microscope (STM) [26]. With this invention, it became possible, for the first time, to visualize the surface structure of conductive and semi-conductive samples at the micro- and nanoscale with a resolution in microscopy never reached in the past and that could show atomic contrast [27]. For this invention, Binnig and Rohrer received the Nobel price in 1986. The principle of the STM consists on a conducting sharp tip approached to the surface of the sample at a distance close enough (below 1 nm) to allow the flowing of a quantum mechanical tunneling current when a voltage is applied. The scanning of the surface enables a three-dimensional representation of the surface topography. The limitation of the STM, when applied to conductive and semi-conductive samples resulted in the developement of a new type of microscope, the atomic force microscope (AFM), by Binnig et al. [8] in 1986. In contrast to STM, this new microscope enables the topography of sample surfaces to be mapped independently of their conductive property. Its principle, which is similar to that of the STM, consists in bringing a tip close enough to the sample surface to interact with its atoms and molecules. However, instead of sensing the tunnel current, the AFM senses the various magnetic and electric interaction forces. Additionally to mapping the topography, the AFM enables probing and determining the local properties of sample surfaces. These properties, most of the time, are determined from mathematical models based on the measurement of the modifications of the characteristics of the vibrating cantilever in dynamic mode AFM, such as the amplitude, the frequency or the phase shift between the excitation and the response signals induced by the interaction between the tip and the sample surface. The variety of local properties that can be investigated by AFM led to a lot of measuring methods: we can cite, for example for electric and magnetic properties, the Kelvin probe force microscopy (KPFM), which measures the local contact potential difference, or the magnetic force microscopy (MFM), which maps the magnetic contrast on the sample surface. Besides the local electric and magnetic properties, the AFM can also probe the local mechanical properties, such as the Poisson's ratio [10], as well as the elastic modulus with the cantilever operated in static and dynamic modes as we will see in this thesis. The present chapter outlines the principle of AFM. The two methods used to investigate the elasticity of polymers in the present work are presented as well.

1.1 AFM principle

To visualize the structures at the micro-/nanoscale, the AFM cantilever tip senses the different forces created at each point of the surface by the atoms and molecules of the sample.

1.1.1 Interaction forces [1–4]

In the nature, four fundamental forces govern interactions : the strong and the weak interactions, the gravitational force and the electromagnetic force. The two first interactions govern the behavior of the protons, neutrons, electrons and other elementary particles at a very short range around 1 fm. The gravitational force is a very-long range interaction that governs the motion of massive bodies such as planets, stars and other celestial bodies but also the attraction of all creatures and solids by the earth. The last fundamental force, the electromagnetic interaction, governs all interactions at the microscopic level and the large variety of forces that govern the interaction between the tip and the sample surface in AFM stem from this interaction. These forces can be separated in two groups: long-range and short-range forces.

Long-range forces

The most important of them are the Van der Waals and the electrostatic forces.

Van der Waals forces

The van der Waals interaction is caused by fluctuations in the electric dipole moment of atoms and their mutual polarization. Van der Waals forces exist between all types of atoms and molecules and describe interactions generated by dipole moments; they appear in all AFM measurements. Three different forces contribute the Van der Waals interaction and are all proportional to the inverse of the power 6 of the distance between atoms or molecules r $1/r^6$:

$-$ the orientation or Keesom force, which is the angle-averaged dipole-dipole interaction between two atoms and molecules and is described by the potential

$$V_{Keesom} = -\frac{u_1^2 u_2^2}{3(4\pi\epsilon_0\epsilon)^2 k_B T r^6} = -\frac{C_K}{r^6},$$

where u_1 and u_2 are the dipole moments of the molecules, ϵ the dielectric constant of the medium, k_B the Boltzmann constant and T the temperature;

$-$ the induction or Debye force, which is the angle-averaged dipole-induced interaction between two atoms or molecules

$$V_{Debye} = -\frac{u_1^2\alpha_{02}+u_2^2\alpha_{01}}{(4\pi\epsilon_0\epsilon)^2 r^6} = -\frac{C_D}{r^6},$$

where α_{01} and α_{02} are the electronic polarizabilities of the molecules,

$-$ the dispersion or London force, which is the most important contribution to the Van der Waals force; it acts between all molecules or atoms. It is an attractive or repulsive force generated by the instantaneous dipole-induced dipole interaction and is of quantum-mechanical origin

$$V_{London} = -\frac{3}{2}\frac{\alpha_{01}\alpha_{02}}{(4\pi\epsilon_0\epsilon)^2 r^6}\frac{h\nu_1 h\nu_2}{h\nu_1 + h\nu_2} = -\frac{C_L}{r^6},$$

where $h\nu_1$ and $h\nu_2$ are the first ionization potentials of the molecules and h the Planck constant.

The total Van der Waals potential can be written as follows

$$V_{VdW} = -\frac{1}{(4\pi\epsilon_0\epsilon)^2 r^6}\left(\left(u_1^2\alpha_{02} + u_2^2\alpha_{01}\right) + \frac{u_1^2 u_2^2}{3k_B T} + \frac{3\alpha_{01}\alpha_{02}}{2}\frac{h\nu_1 h\nu_2}{h\nu_1 + h\nu_2}\right) = -\frac{C_K + C_D + C_L}{r^6}$$

Electrostatic forces

Electrostatic forces stem from the distribution of the free or attached electric charges over the sample surface and obey to the Coulomb law. When the tip and sample are both conductive and have an electrostatic potential difference $U \neq 0$, electrostatic forces are important. The force sensed by the cantilever tip $F_{electrostatic}$ is the result of the contribution of two distinct forces: the charge force F_{charge} and the capacitive force $F_{capacitive}$,

$$F_{electrostatic} = F_{charge} + F_{capacitive},$$

F_{charge} corresponds to the force between a nonconductive sample surface and a conductive tip and is expressed by

$$F_{charge} = q_i E_z,$$

where q_i is the induced charge on the tip and E_z, the electrical field in the direction z normal to the sample surface. The induced charge has two contributions:

$$q_i = -(q_s + CV),$$

where q_s is the charge induced on the tip by the surface charge distribution and CV originates from the voltage, V, between the tip and back electrode with capacitance C. The contribution of the capacitive force $F_{capacitive}$ to $F_{electrostatic}$

$$F_{capacitive} = \tfrac{1}{2}\tfrac{\partial CV^2}{\partial z} = \tfrac{1}{2}V^2 C',$$

where C is the capacitance between the electrodes. For a spherical tip of radius R above a flat sample and a tip-sample distance that is small compared to R, $F_{capacitive}$ is approximately given by

$$F_{capacitive} = -\pi\epsilon_0 R\tfrac{V^2}{z_{eff}},$$

The electrostatic force can hence be written

$$F_{electrostatic} = -(q_s + CV)E_z + \tfrac{1}{2}V^2 C',$$

where z_{eff} is the effective distance between tip and sample. $z_{eff} = z_0 + h/\epsilon$ depends on the thickness h of the insulating film with dielectric constant ϵ. $F_{capacitive}$ is independent of the surface charge, but can be used to measure local variations of the dielectric constant or to estimate the tip radius R.

Short-range forces

In contrast to long-range forces, short range forces do not interact with the whole tip but only with a small part of the tip apex called 'nanotip'. The interaction of an atom of this 'nanotip' with the sample surface is responsible for the atomic resolution. The most important of these forces are called physisorption, chemisorption and Pauli repulsion.

1.1.2 Structure of an AFM microscope

An AFM microscope consists in four units: the sensing, detection, feedback and scanning units. The main unit of an AFM microscope, i.e. the sensing unit, consists of the cantilever and its tip. The tip senses the interaction forces generated by the atoms and molecules of the sample surface. The intensity and the direction of the forces acting on the tip and modifying the shape of the cantilever are then detected by the detection unit. Several types of methods exist for detecting the deflections; we can cite, among others, capacitance, optical interferometry or electronic tunneling. In the most frequently used method, i.e. laser beam, the cantilever vertical and lateral deflection is measured from the reflection of a laser beam on the back of the cantilever. The deflections are measured from the position of the beam in a four-quadrant photodiode system. The vertical deflection signal is used by the feedback unit to regulate the tip-sample distance by computing a value for voltage V_Z necessary to expand or retract the Z piezoelectric scanner by means of a proportional integral (PI) controller. In addition, in the dynamic mode, the PLL and lockin amplifiers integrated in the unit generate the signal u_{exc} that excites the cantilever. The feedback unit generally consists in a module of a controller for AFM, as we will see in the next chapters with SAPHYR. The three-dimensional mapping of topography is done by the mapping unit. It consists of three piezoelectric scanners that expand and retract in the X, Y and Z directions. The voltage necessary to expand or retract the scanners are generated by a module of the microscope controller that furnishes constant signals V_X and V_Y for the X and Y directions and by the feedback unit for the Z direction. These potentials are read by the software of the AFM controller, and their calibration enables the mapping of sample topography.

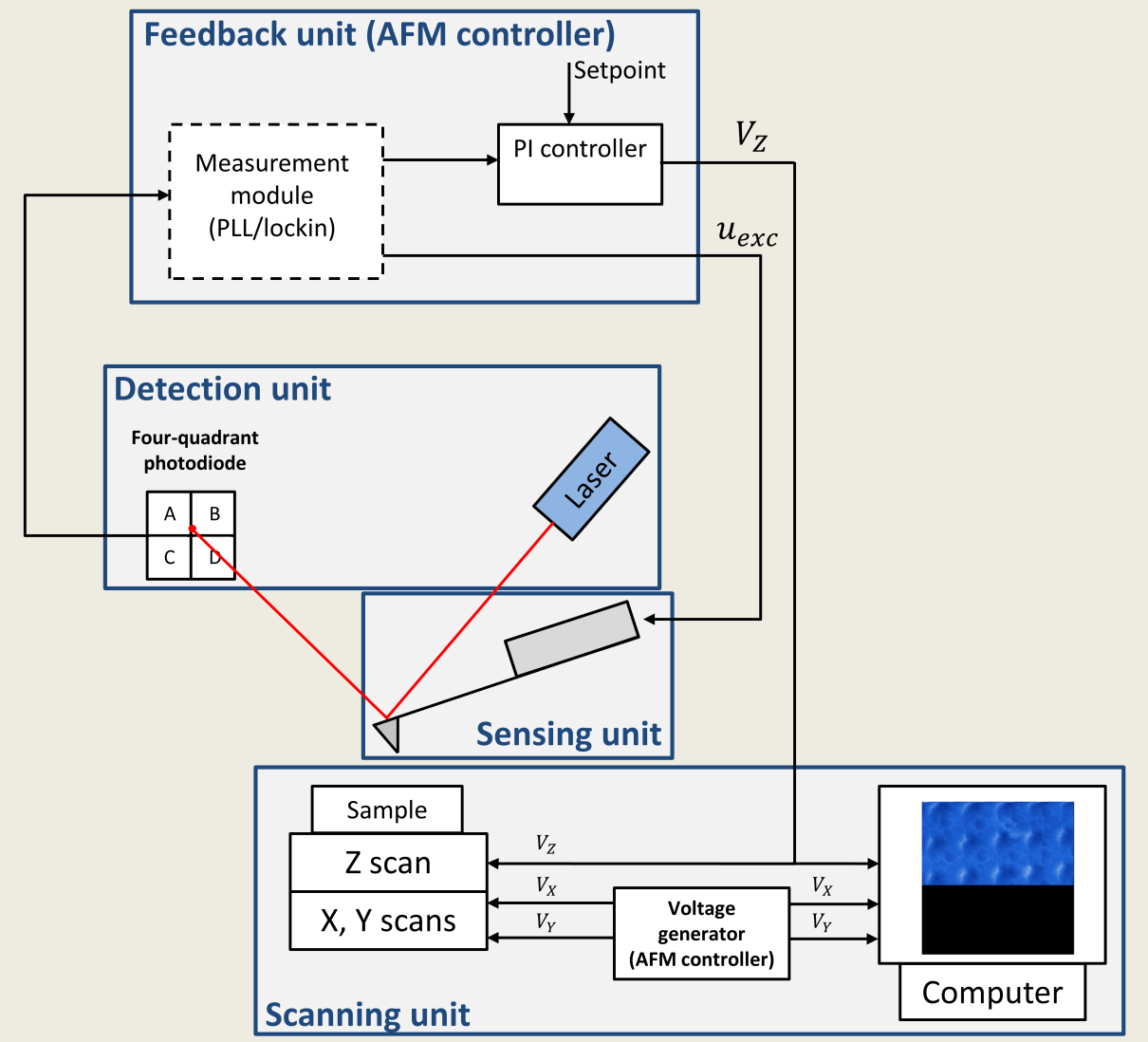

Figure 1: Setup of an AFM microscope. The AFM microscope consists of four different units, i.e. the sensing, detection, feedback and scanning units. In the sensing unit, the tip senses the interaction forces generated by the surface with the cantilever tip. In the detection unit, the bending of the cantilever is detected by the reflection of a laser beam on the back of the cantilever. The amplitude of the bending of the cantilever is given by the position of the beam on a four-quadrant photodiode system. In the feedback unit, the tip-sample distance is regulated by the computation of voltage V_Z necessary to expand or retract the Z scanner by a PI controller; the value is computed either from the vertical deflection signal or from the value measured by a module of the AFM controller – either a lockin or a PLL. In the mapping unit, the voltages V_X and V_Y are generated by a voltage generator of the AFM controller to move the X and Y scanners. V_X, V_Y and V_Z voltages are read by the controlling software to map the sample topography.

1.2 Imaging modes for the measurement of topography by AFM

Two modes are used to measure sample topography, a static and a dynamic mode. Both modes depend on the type of feedback used. In static mode, the interaction forces are detected from the bending of the cantilever. In dynamic mode, the cantilever is excited by means of a piezo-electric shaker at the resonance frequency of the first flexural mode, as illustrated in figure 1.2. When the tip interacts with the sample, the oscillation amplitude and resonance frequencies of the cantilever are changed. The interaction forces is controlled from the oscillation amplitude or from the frequency shift of the resonance.

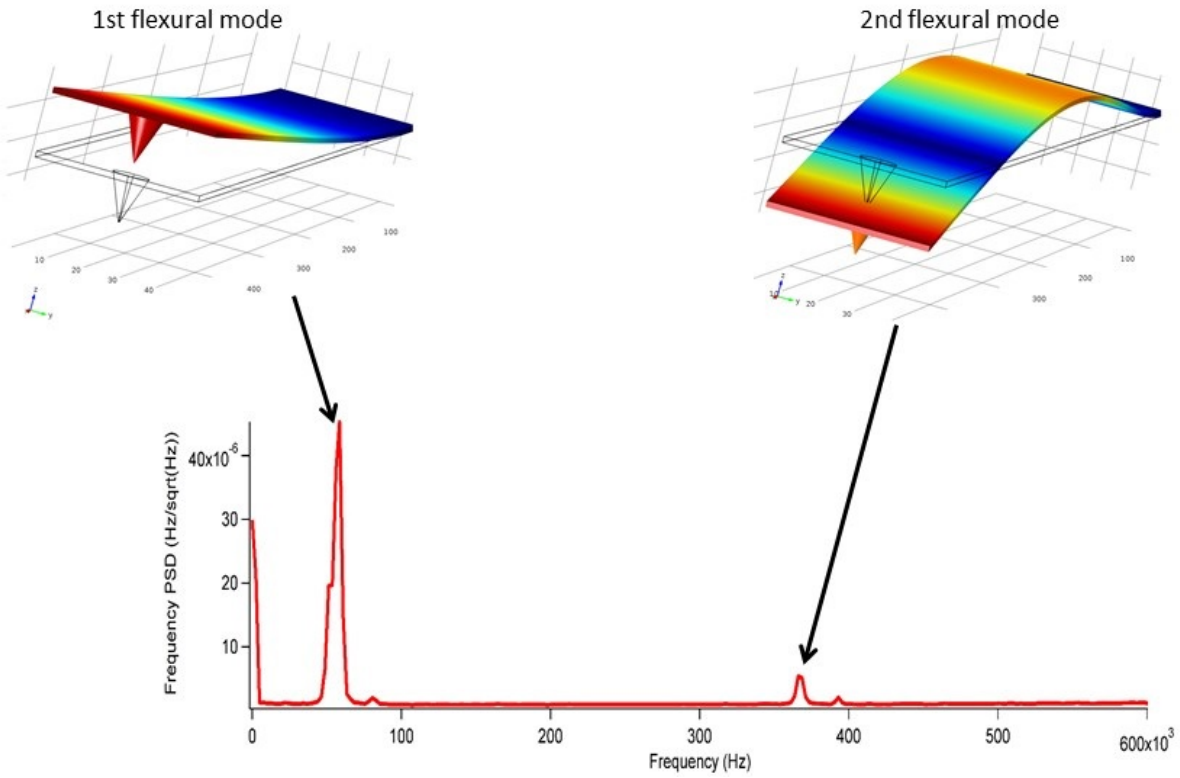

Figure 2: Spectrum of the resonance frequencies associated with the first and second flexural modes of a cantilever. The first mode is generally used in dynamic mode AFM to measure the topography of samples.

1.2.1 Contact or friction mode AFM

Contact or friction mode AFM is the first mode that was used to image the topography of samples. Due to its invasivity, this mode is especially adapted for imaging the surface of hard samples, where the lateral forces are not expected to modify the features of the surface while scanning. This mode enabled, for the first time, atomic and molecular resolution of crystals such as mica, Au(111), such as salts NaCl and KBr or chalcogenides of transition metals. Contact AFM consists in measuring the corrugation of surfaces by sweeping the surface with the tip in permanent contact. No excitation signal u_{exc} is used. The principle for measuring topography consists in maintaining the applied vertical force equal to user-defined setpoint $F_{N,set}$. The measured force value represented by the vertical deflection is directly applied to the PI controller of the feedback unit (figure 3) that computes the voltage V_Z necessary to keep the deflection constant.

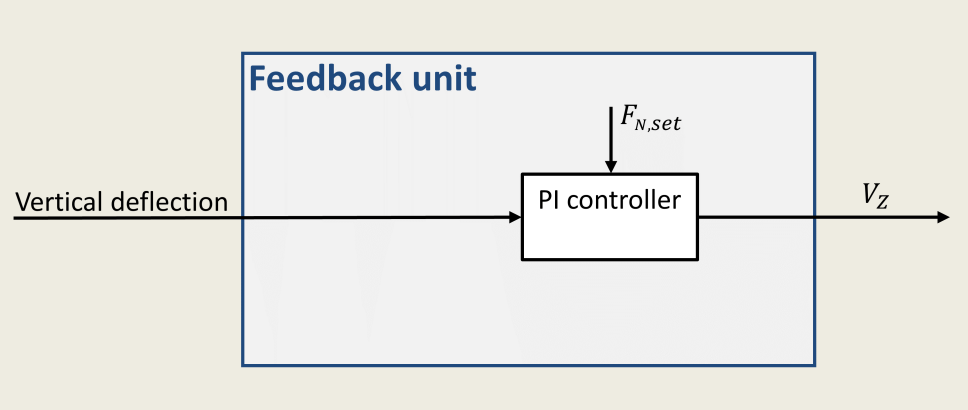

Figure 3: Structure of the feedback unit used when measurements are performed in contact mode. The vertical deflection signal is directly applied to the PI controller that computes the voltage V_Z necessary to regulate the tip-sample distance; the vertical deflection signal is regulated to setpoint $F_{N,set}$. No excitation signal u_{exc} is applied to the cantilever.

1.2.2 Intermittent-or AM-mode AFM

Intermittent-mode AFM, also called amplitude modulation (AM) mode, belongs to the dynamic modes for imaging the topography of surfaces. This technique of imaging was introduced by Bruker to enable the measurement of the topography of soft materials. The principle for measuring topography consists in exciting the cantilever at a frequency close to the resonance of the first flexural mode and maintaining the amplitude of oscillation of the cantilever as close as possible to setpoint A_{set}. For this purpose, the feedback unit integrates a lockin amplifier (figure 4) that measures oscillation amplitude of the cantilever A from the vertical deflection signal. The tip-sample distance is regulated with a user-defined setpoint A_{set}, by means of a PI controller that generates voltage V_Z. In addition, the lockin amplifier generates signal u_{exc} for the excitation of the cantilever.

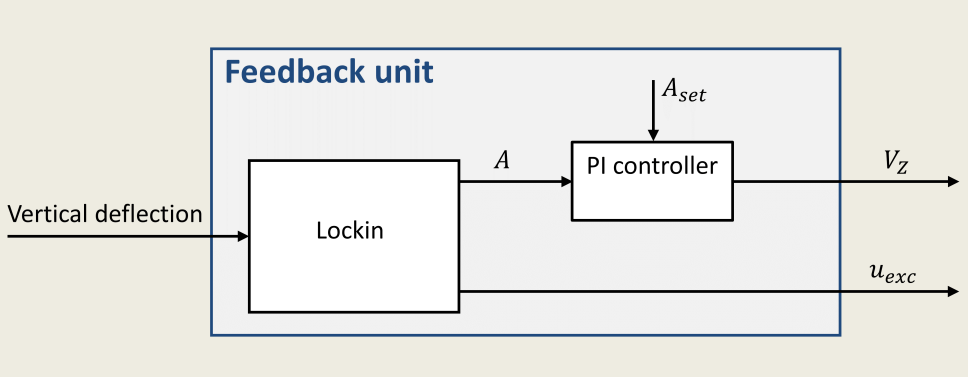

Figure 4: Structure of the feedback unit used when measurements are performed in AM mode. Oscillation amplitude of cantilever A is measured from the vertical deflection signal by a lockin amplifier and applied to the PI controller that computes the voltage V_Z necessary to regulate the tip-sample distance; the oscillation is regulated to setpoint A_{set}. The lockin amplifier generates the excitation signal u_{exc} applied to the cantilever.

1.2.3 FM mode

Frequency-modulation (FM) mode AFM exhibits among the three different modes of operation the best resolution. The first atomic resolution using the AFM was obtained for a surface of silicon(111) by Giessibl in 1994 [28]. In this dynamic mode, the tip oscillates periodically at the resonance frequency of the first flexural mode of the cantilever without touching the sample surface; measurements are generally performed in ultra high vacuum. Oscillation amplitudes are much smaller than for AM mode. Due to the interaction between the tip and the atoms and molecules of the surface the resonance frequency is shifted: the tip-sample distance is regulated by keeping the frequency shift equal to user-defined setpoint Δf_{set}. For this purpose a PLL is integrated to the feedback unit (figure 5). The PLL measures the frequency shift Δf from the vertical deflection signal: the signal is used by the PI controller to compute the voltage V_Z. Additionally, the PLL generates the signal u_{exc} for the excitation of the cantilever.

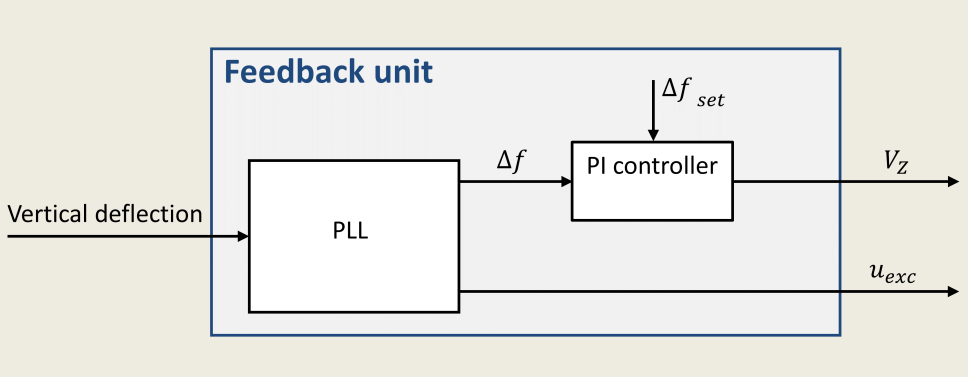

Figure 5: Structure of the feedback unit used when measurements are performed in FM mode. Frequency shift of resonance of cantilever Δf is measured from the vertical deflection signal with a PLL and applied to the PI controller that computes the voltage V_Z necessary to regulate the tip-sample distance; the frequency shift is regulated to setpoint Δf_{set}. The PLL generates the excitation signal u_{exc} applied to the cantilever.

1.3 Methods for the measurement of Young's modulus

Initially, AFM was devised to map the topography of sample surfaces, but it soon showed great potential for probing and determining the local properties of sample surfaces. This led to different measuring methods depending on the type of properties, such as electrical or magnetic properties; we would like to mention among others, the Kelvin probe force microscopy (KPFM), which measures the local contact potential difference, or the magnetic force microscopy (MFM), which maps the magnetic contrast. Besides local electric and magnetic properties, the AFM can also probe local mechanical properties, such as Poisson's ratio [10] as well as the elastic modulus, [14] [11].

1.3.1 Oliver and Pharr's static method for rigid indenters

In 1992, Oliver and Pharr [25] published a reference article describing an improved method to determine the elasticity modulus of a sample from a load-displacement curve obtained by indentation with a rigid indenter. Due to their shape, AFM cantilever tips are well suited to perform nanoindentations and hence to locally determine the elasticity modulus of a sample by Oliver and Pharr's method.

Principle of Oliver and Pharr's method

The method, based on the work of Doerner and Nix [29], was developed to determine the hardness and elasticity of a sample from a load-displacement curve (figure 7) obtained by the indentation of a rigid, sharp, geometrically self-similar indenter like the Berkovich triangular pyramid, as illustrated in figure 6. Afterwards, they showed that the model could be applied to a variety of indenters with an axisymmetry geometry like spheres [30].

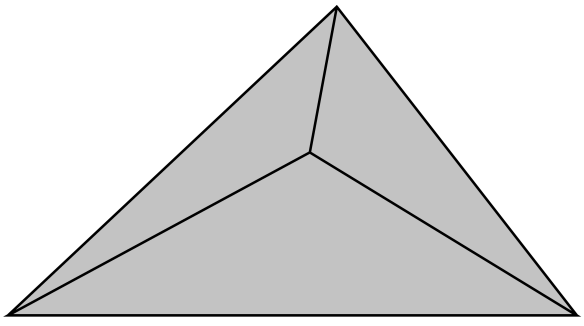

Figure 6: Profile of the Berkovich tip of a rigid indenter.

The model they developed is based on the contact model of Hertz, where the normal contact stiffness $k_{sample,norm}$ is related to effective Young's modulus of the sample E_{eff} and the contact

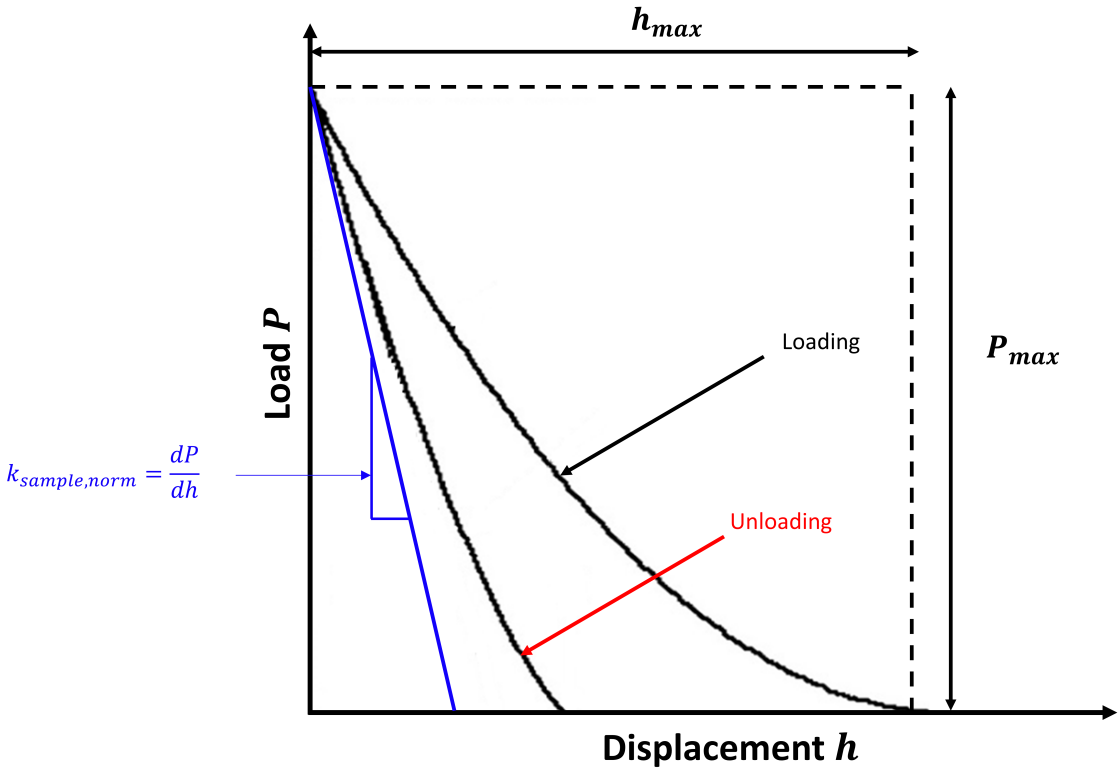

Figure 7: Characteristic load-displacement curve obtained by indentation done with a rigid indenter [25, 30].

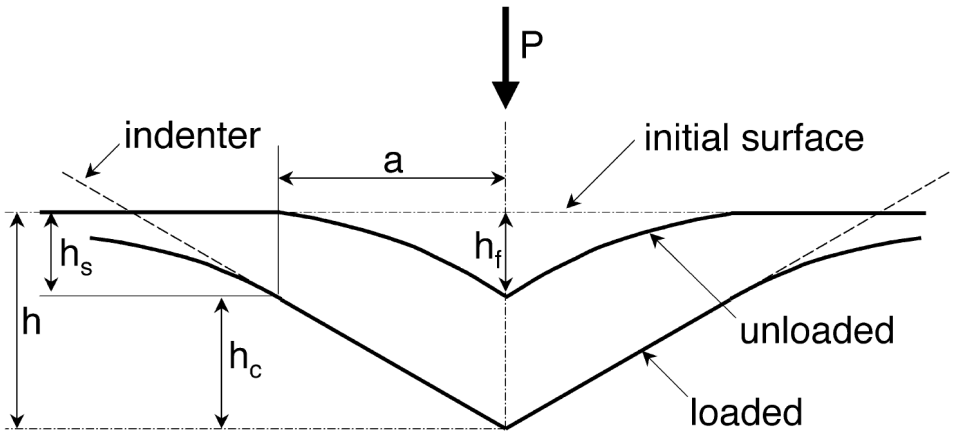

Figure 8: Profile of an indentation, due to loading and unloading, and parameters that characterize it [25, 30].

radius a by the relation

$$k_{sample,norm} = 2aE_{eff}. \tag{1.1}$$

By relating the contact radius a to the projected contact area A of the elastic contact

$$A = \pi a^2,$$

equation 1.1 can be written

$$k_{sample,norm} = 2\sqrt{\frac{A}{\pi}}E_{eff},$$

and the effective Young's modulus of sample E_{eff}

$$E_{eff} = \frac{1}{2}\sqrt{\frac{\pi}{A}}k_{sample,norm}. \tag{1.2}$$

Contact stiffness $k_{sample,norm}$ and the projected contact area A are determined from the load/unload-displacement curves, as illustrated in figure 7. In the model, the indenter penetrates to a depth $h = h_{max}$ with a load P_{max}, during loading and then retracts. Loading is accompanied by an elastic and a plastic deformation. The unloading curve describes the recovery of the elastic displacement and can be accurately described by the power law relation

$$P = \alpha(h - h_f)^m, \tag{1.3}$$

where P corresponds to the load, h to the displacement and h_f to the residual hardness impression. Parameters α and m are obtained by fitting the curve. The derivate of the power law function gives the value of the contact stiffness $k_{sample,norm}$. The load-displacement curve also gives the parameters of the profile of the indentation (figure 8). These parameters are necessary to compute the contact area. An approximation of A, for a Berkovich indenter, is defined as

$$A = 24.5h_c^2, \tag{1.4}$$

where h_c corresponds to the contact depth and is defined as

$$h_c = h_{max} - h_s. \tag{1.5}$$

The contact perimeter h_s is defined from the maximum load P_{max}, from contact stiffness $k_{sample,norm}$ and from a parameter ε depending on the geometry of the indenter and of values ε =0.72 for a conical indenter, ε =0.75 for a paraboloid of revolution and ε =1 for a flat punch.

$$h_s = \varepsilon\frac{P_{max}}{k_{sample,norm}}. \tag{1.6}$$

Finally, sample elasticity E_{sample} can be determined from the knowledge of the indenter Poisson's ratio $\nu_{indenter}$ and Young's modulus $E_{indenter}$ and from the sample Poisson's ratio ν_{sample} and E_{eff} by the relation

$$\frac{1}{E_{eff}} = \frac{1-\nu_{sample}}{E_{sample}} + \frac{1-\nu_{indenter}}{E_{indenter}}.$$

Hence,

$$\boxed{E_{sample} = \frac{(1-\nu_{sample})E_{eff}E_{indenter}}{E_{indenter} - (1-\nu_{indenter})E_{eff}}}. \tag{1.7}$$

Additionally to Young's modulus, the method enables the determination of the hardness as the mean pressure that the material supports under the load.

$$H = \frac{P_{max}}{A}. \tag{1.8}$$

1.3.2 Herruzo and Garcia's dynamic bimodal method

The method is based on the simultaneous excitation of the first and second cantilever flexural modes (figure 1.2) to determine the elasticity of a sample. From the values of the measured frequency shift in the two modes during the contact of the tip with the sample, the elasticity of the sample can be established. The indentations are done with an oscillation amplitude of the first flexural mode larger than the length scale of the interaction force. The mathematical relation linking Young's modulus of the sample to the measured frequency shifts is established by first assuming that the amplitude of the first flexural mode of the cantilever is larger than the length scale of the interaction force. This assumption enables the frequency shift in the first flexural mode Δf_1 to be determined by considering the frequency shift as the convolution of the interaction force with the function $\frac{2}{\pi A_1^2\sqrt{A_1^2-u^2}}$ [23]

$$\Delta f_1(d_m) \approx -\frac{f_{0,1}}{\pi k_1 A_1^2}\int_{-A_1}^{A_1} F_{TS}(d_m + A_1 + u)\frac{u}{\sqrt{A_1^2-u^2}}\mathrm{d}u, \tag{1.9}$$

if $\Delta f_1(d_m) \ll f_{0,1}$ [31], where $f_{0,1}$, k_1, A_1, F_{TS}, d_m stand for the resonance frequency of the first flexural mode, the spring constant and the oscillation amplitude of the first flexural mode, the tip-sample interaction force and the closest distance between tip and sample in an oscillation cycle.

d_m is defined [11] as a function of the amplitudes A_1 and A_2 of the first and second flexural modes and the mean tip-surface separation z_c by

$$d_m = z_c - A_1 - A_2.$$

The frequency shift of the second flexural mode $\Delta f_2(d_m)$ is then determined from the virial of the second flexural mode $V_{TS}(2)$ [23]

$$V_{TS}(2) = \frac{1}{T}\int_0^T F_{TS}(t) z_2(t) \mathrm{d}t, \tag{1.10}$$

where $z_2(t)$ corresponds to a solution of the system of differential equations describing the dynamics of the cantilever-tip system [18]. The tip deflection $z(t)$ can be described by the function [23]

$$z(t) \approx z_0 + z_1(t) + z_2(t) = z_0 + A_1 cos\left(2\pi f_{0,1} t - \frac{\pi}{2}\right) + A_2 cos\left(2\pi f_{0,2} t - \frac{\pi}{2}\right), \tag{1.11}$$

where z_0 stands for the mean deflection [23]. By substituing equation 1.11 into equation 1.10, a first expression for $V_{TS}(2)$ can be found

$$V_{TS}(2) \approx -k_2 A_2^2 \frac{\Delta f_2(d_m)}{f_{0,2}}. \tag{1.12}$$

A second relation for the virial can be established by assuming $A_1 \gg A_2$: in this case, $z(t)$ can be expanded in power series of $A_2 cos\left(2\pi f_{0,2} t - \frac{\pi}{2}\right)$

$$V_{TS}(2) \approx \frac{A_2^2 f_{0,1}}{2} \int_{-\frac{1}{2f_{0,1}}}^{\frac{1}{2f_{0,1}}} F'_{TS}\left(z_c + A_1 cos\left(2\pi f_{0,1} t - \frac{\pi}{2}\right)\right) \mathrm{d}t, \tag{1.13}$$

where F'_{TS} stands for the force gradient.

By combining equations 1.12 and 1.13, an expression for $\Delta f_2(d_m)$ can be found [23] that is similar to the one established by Kawai et al. [32] and links $\Delta f_2(d_m)$ to the average gradient of the interaction force over one period of oscillation of the first mode when $A_1 \gg A_2$

$$\Delta f_2(d_m) \approx -\frac{f_{0,1} f_{0,2}}{2k_2} \int_{-\frac{1}{2f_{0,1}}}^{\frac{1}{2f_{0,1}}} F'_{TS}\left(d_m + A_1 + A_1 cos\left(2\pi f_{0,1} t - \frac{\pi}{2}\right)\right) \mathrm{d}t.$$

By defining a new variable $u = A_1 cos\left(2\pi f_{0,1} t - \frac{\pi}{2}\right)$ the expression for $\Delta f_2(d_m)$ can be rewritten as the convolution of the force gradient with the function $\frac{1}{\pi \cdot \sqrt{A_1^2 - u^2}}$

$$\Delta f_2(d_m) \approx -\frac{f_{0,2}}{2\pi k_2} \int_{-A_1}^{A_1} F'_{TS}\left(d_m + A_1 + u\right) \frac{1}{\sqrt{A_1^2 - u^2}} \mathrm{d}u. \tag{1.14}$$

The two established expressions for $\Delta f_1(d_m)$ and $\Delta f_2(d_m)$ in 1.9 and 1.14 can be rewritten as a half integral and a half derivative of F_{TS}

$$\Delta f_1(d_m) = \frac{f_{0,1}}{k_1 \sqrt{2\pi A_1^3}} I_-^{\frac{1}{2}} F_{TS}\left(d_m\right),$$

and

$$\Delta f_2(d_m) = \frac{f_{0,2}}{2k_2\sqrt{2\pi A_1}} D_-^{\frac{1}{2}} F_{TS}\left(d_m\right),$$

where

$$I_-^{\frac{1}{2}} F_{TS}\left(z\right) = \frac{1}{\Gamma\left(\frac{1}{2}\right)} \int_z^{\infty} \frac{F_{TS}\left(z\right)}{\sqrt{t-z}} \mathrm{d}t,$$

and

$$D_-^{\frac{1}{2}} F_{TS}\left(z\right) = \frac{-1}{\Gamma\left(\frac{1}{2}\right)} \frac{\mathrm{d}}{\mathrm{dz}} \int_z^{\infty} \frac{F_{TS}\left(z\right)}{\sqrt{t-z}} \mathrm{d}t.$$

The calculation of the fractional integral and derivative by using the Riemann-Liouville fractional calculus and taking as expression for the tip-surface interaction F_{TS}

$$F_{TS}\left(d\right) = F_{con} + F_{dis} = \frac{4}{3} E_{eff}\sqrt{R}\delta^{\frac{3}{2}} - \eta\sqrt{R\delta}\dot{\delta},$$

where F_{con} and F_{dis} correspond to the conservative and dissipative interactions modelized, respectively, by Hertz contact mechanics and the linear viscoelastic theory, R, δ and η for the effective tip radius, the indentation depth and viscous coefficient, yields the expressions for $\Delta f_1(d_m)$ and $\Delta f_2(d_m)$

$$\Delta f_1(d_m) = \sqrt{\frac{R}{8A_1^3}} \frac{f_{0,1}}{k_1} E_{eff}\delta^2, \tag{1.15}$$

and

$$\Delta f_2(d_m) = \sqrt{\frac{R}{8A_1}} \frac{f_{0,2}}{k_2} E_{eff}\delta. \tag{1.16}$$

From equations 1.15 and 1.16, the expresion of E_{eff} as a function of $\Delta f_1(d_m)$ and $\Delta f_2(d_m)$ is established [11]

$$\boxed{E_{eff} = \sqrt{\frac{8}{RA_1}} \frac{k_2^2 f_{0,1}}{k_1 f_{0,2}^2} \frac{\Delta f_2(d_m)^2}{\Delta f_1(d_m)}}. \tag{1.17}$$

If Young's modulus of the tip E_{tip} is two orders of magnitude larger than Young's modulus of the sample E_{sample}, the following approximation can be made

$$\boxed{E_{eff} \backsim E_{sample}}. \tag{1.18}$$

Chapter 2

SAPHYR, a controller for SPM experiments

A controlling electronic system is mandatory to perform SPM experiments. Signals must be generated to move the cantilever over the sample, keep the cantilever tip at a certain distance from the sample surface or simply excite the cantilever. Additionally, electronic devices, such as lockin amplifiers and PLLs for the treatment of excitation and response signals of the cantilever, are required to extract information (frequency shift, cantilever oscillation amplitude, phase shift) from the response signal and adjust it to fit the parameters of theoretical models for the determination of interaction forces but also physical characteristics of samples such as elasticity. However, a good electronic system must satisfy certain requirements. For instance, the control system must be fast enough to measure the variations in time of the studied phenomenon, enable a high enough resolution of their ADCs and DACs to obtain precise values and low noise. Additionally, the development of new theoretical models in recent years requires an increasing amount of PLLs and lockin-like devices but also devices that can generate signals with user-defined shapes different from the sinusoid for the extraction of information. This increase in the number of PLLs, lockins and other electronic devices takes up much space. A compact system embedding all of them would save much space. However, it is also necessary to reduce the noise generated by the interconnections between different units. In 2008, the SAPHYR controller stemmed from a common project jointly devised by the Nanolino group of the Department of Physics of the University of Basel (Switzerland) and Nanosurf, based in Liestal (Switzerland) and specialized in SPM, with the aim of developing a controller satisfying to these requirements. It is fundamental for scientists to understand the functioning of the devices for analyzing and generating signals as they need to know what to measure and how to configure the devices in order to obtain correct results. An important part of the present work focuses on the SAPHYR controller: the software for its control and an algorithm to improve the computation of the phase shift in the lockins of its electronics were developed and measurements were performed with it. For these reasons, the SAPHYR controller will be presented in this chapter.

Figure 9: Front view of the SAPHYR controller.

Figure 10: Back view of the SAPHYR controller.

2.1 Structure of SAPHYR

SAPHYR is a compact system that embeds different devices, called modules, for the generation, conditioning and treatment of signals, as seen in figures 9 and 10. It can contain up to 4 PLL modules or 3 PLL modules and 1 Kelvin module, 2 Math modules each containing 2 PI controllers and a Subharmonic module for the generation of user-defined periodic pulse signals. SAPHYR is a half-analog half-digital system. The digital part, represented by an FPGA, is the heart component of the controller where the lockin amplifiers, PLLs, PI controllers and other devices are programmed and where information on the frequency shifts, oscillation amplitudes of the cantilever and other quantities is computed and conditioned to be sent to the computer by a USB interface. The FPGA is located on a mainboard which also contains the connectors where the analog part of the modules and other input/output interfaces are plugged in, as illustrated in figure 12. The analog part of the modules and the input interfaces essentially condition the signals that must be treated by the digital part of the modules by filtering, compensating, amplifying or attenuating and by adding offsets before their digitizing. It also conditions the output signals and, in addition, permits the visualization of signals. In general, the output connectors of the modules and input/output interfaces are of the BNC type whereas the input connectors are of the 2-pole LEMO type, as seen in figure 11.

Figure 11: SAPHYR module interfaces. From left to right: PLL, Kelvin, Math and Subharmonic. The output connectors are of the BNC type whereas the input connectors are of the 2-pole LEMO type.

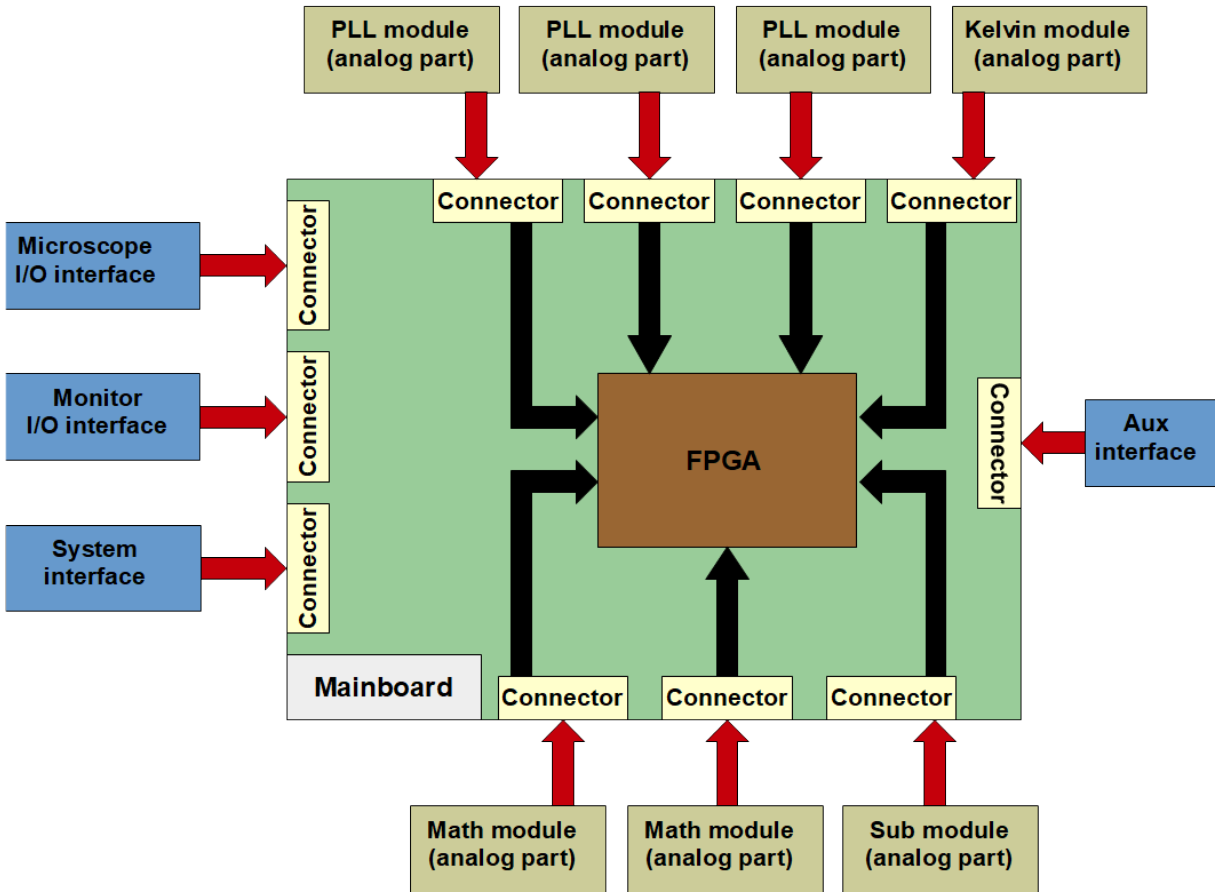

Figure 12: Interconnection of the modules and input/output (I/O) interfaces with the mainboard in SAPHYR. The FPGA represents the digital part of SAPHYR where the lockin amplifiers, PLLs, PI controllers and other devices are programmed. The analog part of the modules and the input/output interfaces essentially condition the signals.

2.2 Description of the modules

2.2.1 PLL module

The PLL module can be configured in two different working modes: the lockin amplifier and the PLL. As their functioning principles will be described in more detail in chapter 4, they will be outlined only briefly here. As shown in figure 13, lockin amplifiers compute the oscillation amplitude of the cantilever $A(f) = |\overline{H}(f)|U_0$ and the phase shift $\varphi(f)$ between the excitation signal $u_{exc}(t) = U_0 sin(2\pi ft + \phi_0)$ and the response signal of the cantilever $u_{resp}(t) = |\overline{H}(f)|U_0 sin(2\pi ft + \phi_0 + \varphi(f))$, where $|\overline{H}(f)|$ is the module of the transfer function of the cantilever, U_0 the amplitude of excitation of the cantilever, f the frequency of the excitation signal, t the time and ϕ_0 the phase at origin.

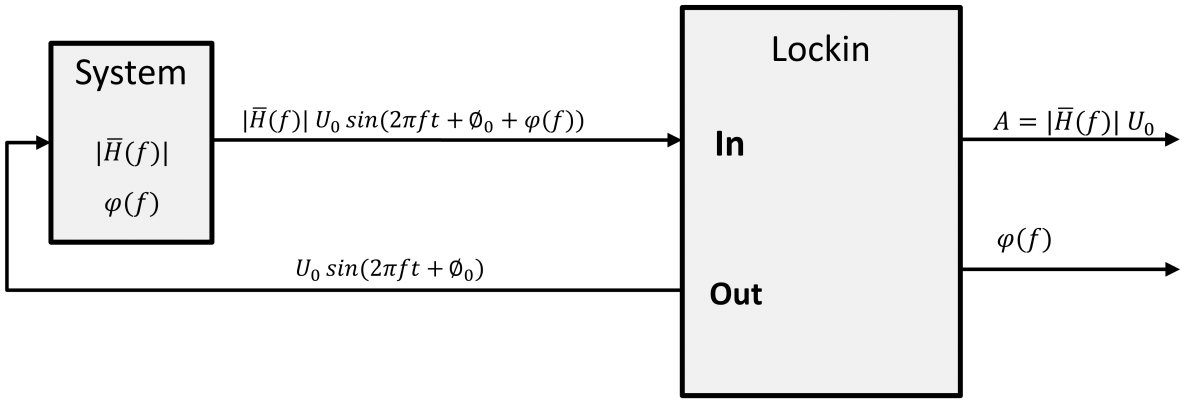

Figure 13: Schematic diagram of a lockin amplifier: the device computes the oscillation amplitude $A(f) = |\overline{H}(f)|U_0$ of the cantilever response signal u_{resp} and the phase shift $\boldsymbol{\varphi(f)}$ between the excitation signal u_{exc} and u_{resp}. $|\overline{H}(f)|$ corresponds to the modulus of the transfer function of the cantilever; U_0, f and ϕ_0 stand for the oscillation amplitude, frequency and phase at the origin of u_{exc}, and t for time.

PLLs maintain a phase shift $\varphi(f)$ equal to a value specified by a setpoint φ_{set} by modifying the frequency of the excitation signal. Their stucture generally includes a lockin amplifier to measure the phase shift. The PLL module of SAPHYR implements the general structure of a digital PLL that can be used in lockin or PLL mode, as shown in figure 14. This structure consists of three different parts: the measurement of the phase shift (part 1), the control (part 2) and the modification of the excitation frequency (part 3). In part 1, phase shift $\varphi(f)$ and oscillation amplitude $A(f)$ are measured by a lockin amplifier. In part 2, both quantities are used to compute the frequency shift Δf that is added to the reference signal f_{ref} in part 3, and the new oscillation amplitude $U_{0,PI}$ of the excitation signal u_{exc}. Δf and $U_{0,PI}$ are computed by subtracting, respectively, $\varphi(f)$ and $A(f)$ from a setpoint value φ_{set} and A_{set} and applying the differences $\Delta\varphi$ and ΔA to a proportional/integral (PI) controller. Both quantities are computed by the PI controllers as follows

$$\Delta f = K_P \Delta\varphi(t) + K_I \int \Delta\varphi(t)dt, \tag{2.1}$$

$$U_{0,PI} = K'_P \Delta A(t) + K'_I \int \Delta A(t) dt, \tag{2.2}$$

where K_P and K'_P are the proportional gains, and K_I and K'_I, the integral gains of constant values of the PI controllers. This part is important if the phase shift $\varphi(f)$ or/and the oscillation amplitude $A(f)$ must be maintained equal to a setpoint value φ_{set} and A_{set}. For this purpose, part 2 computes a Δf and/or a $U_{0,PI}$ with the PI controller until $\varphi(f) = \varphi_{set}$ and $A(f) = A_{set}$. The working mode of the PLL module can be chosen in part 3. In the lockin mode, the reference frequency f_{ref} is used as the frequency of the sinusoidal signal $sin(2\pi ft + \phi_0)$ generated by the numerically controlled oscillator (NCO). The signal is multiplied by an amplitude U_0 either of constant value $U_{0,ref}$ – defined by the controlling software – or $U_{0,PI}$ – computed with the PI controller. In the PLL mode, the frequency of the sinusoid generated by the NCO is the sum of the frequency shift Δf computed with the PI controller with the reference frequency f_{ref}. As in lockin mode, the signal is multiplied by an amplitude U_0 either of constant value $U_{0,ref}$ – defined by the controlling software – or $U_{0,PI}$ – computed with the PI controller. The structure of the PLL implemented in SAPHYR is illustrated in figure 15. The three previously described structures can be distinguished. In addition, the NCO is used to generate a compensation signal (figure 15) that can be subtracted directly from the signal at the input of the PLL module (figure 16). The quantities measured and computed, i.e. oscillation amplitude A, phase shift $\varphi(f)$, frequency shift Δf, amplitude of the excitation U_0, excitation signal u_{exc} and the compensation signal are digitized by an ADC and displayed at the outputs of the PLL module interface outputs – DAC R, DAC φ, DAC Δf, DAC excitation, DAC reference and DAC compensator. Instead of the oscillation amplitude A and the phase shift $\varphi(f)$, the in-phase X and quadrature Y components (see subsection 3.2.1) may be applied at DAC R and DAC φ outputs.

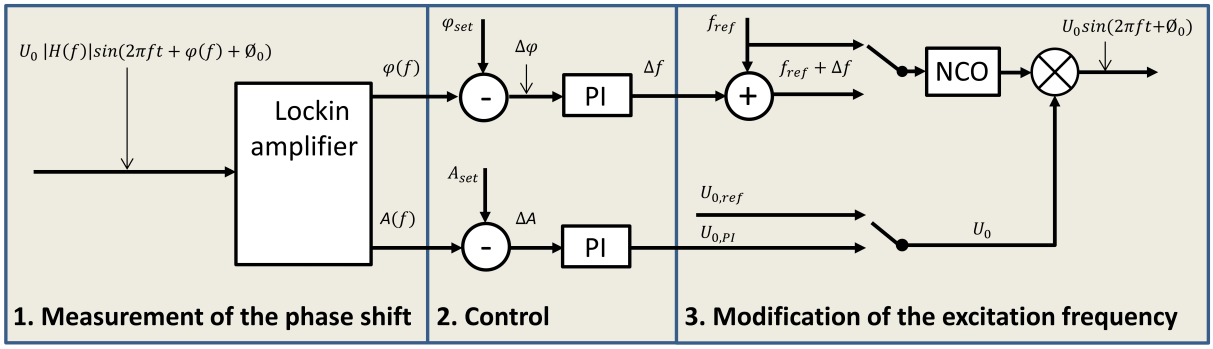

Figure 14: Structure of a digital PLL. It consists of three different parts, namely measurement of the phase shift (part 1), control (part 2) and modification of the excitation frequency (part 3). The oscillation amplitude of the cantilever and the phase shift are measured in part 1. The frequency shift Δf and amplitude of the excitation signal $U_{0,PI}$ are computed in part 2. The working mode of the PLL module can be chosen in part 3: either lockin amplifier mode or PLL mode.

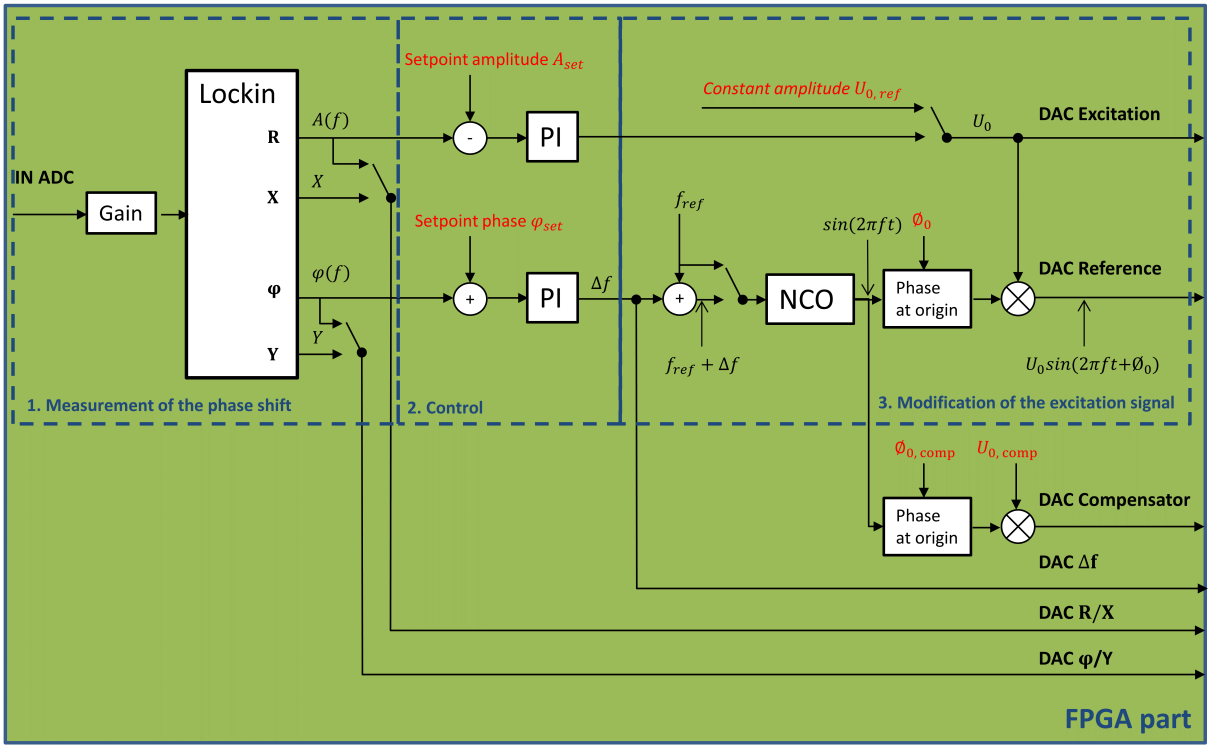

Figure 15: Structure of the digital part of the PLL module. The three structures mentioned in figure 14, namely measurement of the phase shift, control and modification of the excitation frequency are shown. In addition, the NCO is used to generate a compensation signal that can be directly subtracted from the signal at the input of the PLL module. The quantities measured and computed, i.e. oscillation amplitude A, phase shift $\varphi(f)$, frequency shift Δf, amplitude of the excitation U_0 , excitation signal u_{exc} and the compensation signal, are digitized by an ADC and displayed at outputs of the PLL module interface $-$ DAC R, DAC φ, DAC Δf, DAC excitation, DAC reference and DAC compensator. Instead of oscillation amplitude A and phase shift $\varphi(f)$, the in-phase and quadrature components (subsection 3.2.1) may be applied at the DAC R and DAC φ outputs.

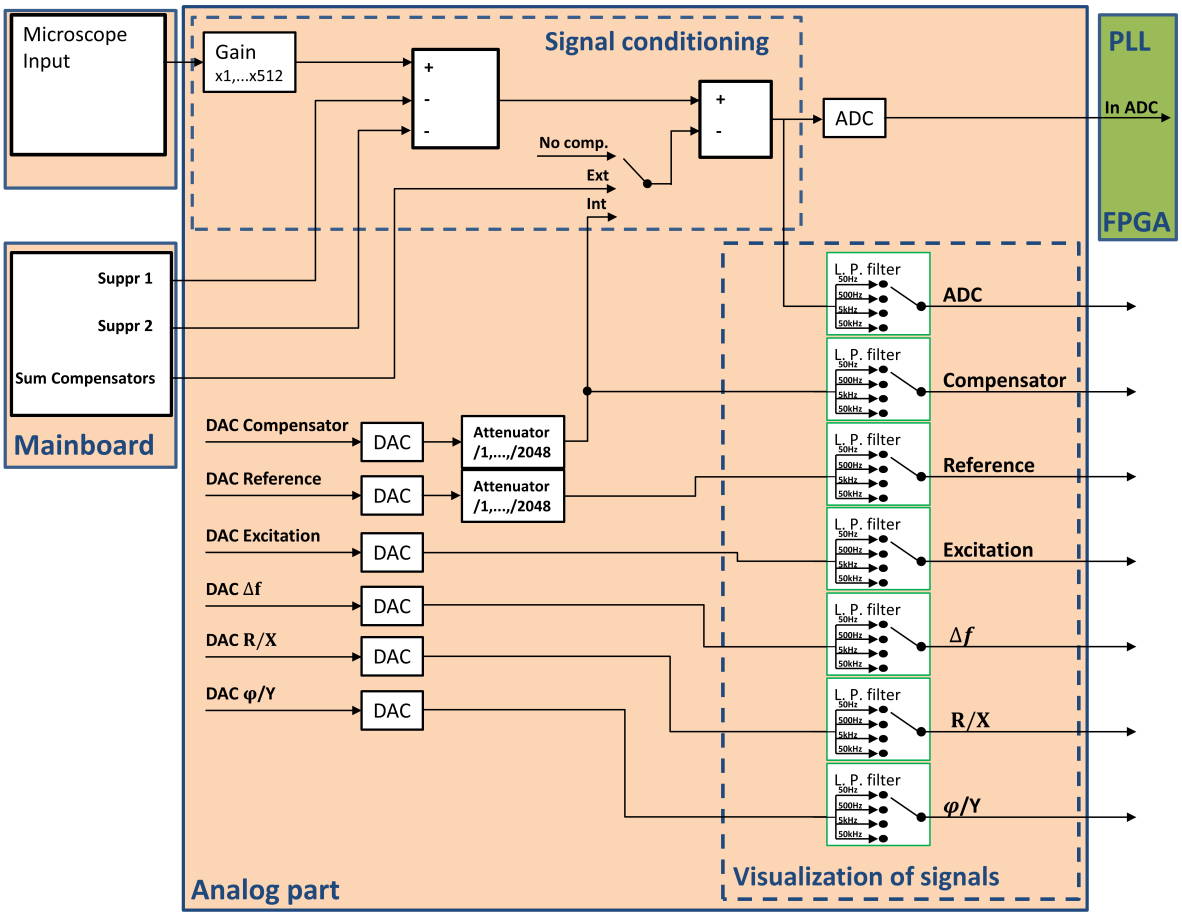

Figure 16: Structure of the analog part of the PLL module. The selected input signal from the Microscope input part (figure 20) is multiplied by a gain before its digitization to increase its resolution. In addition, two suppression signals and a compensation signal consisting either of the compensation signal generated by the NCO of the PLL module or of the sum of selected compensation signals from all PLL modules can be subtracted from it before digitization. The digital signals computed by the digital part of the PLL module – DAC R, DAC φ, DAC Δf, DAC excitation, DAC reference and DAC compensator – after their conversion to an analog signal by DACs and the input signal that must be digitized can be filtered with a lowpass Butterworth filter with cutoff frequencies of 50 Hz, 500 Hz, 5 kHz or 50 kHz befored being displayed at outputs R, φ, Δf, Excitation, Reference, Compensator and ADC in the PLL module interface (figure 11).

2.2.2 Math module

The Math module (figure 17) consists of two identical submodules that can be used in two separate modes: the acquisition and signal generation mode for the acquisition and generation of constant signals and the PI controller mode that enables the regulation of a selectable input signal by means of a PI controller. Each input of the submodules can be filtered by a Butterworth lowpass filter with a set cutoff frequency of 20 MHz to suppress the noise, whereas the output signal can be filtered by a Butterworth lowpass filter with selectable cutoff frequencies of 50 Hz, 500 Hz, 5 kHz or 50 kHz.

Acquisition and signal generation mode

In this mode, the signals at the inputs In A, In B, In C and In D are digitized and can be read by the software. At the same time, a signal of constant value can be generated at outputs Out A, Out B, Out C and Out D from values entered in the software. This mode enables the digitization of the value of the vertical and lateral cantilever deflection signals from the photodiode. Additionally, the signals necessary for the scanners to move the tip in the three-dimensional space can be generated at the different outputs.

PI controller mode

Regulation feedback loops can now be found nowadays everywhere, let us cite among many examples the speed regulation of a car, the phase shift regulation in PLLs as previously explained or the control of the tip-sample distance. They consist of a loop where the excitation and answer signals of a system are controlled by a controlling structure called corrector or controller. In this kind of loop, the answer of the system must always stay as close as possible to a setpoint value. As soon as a perturbation occurs in the system, its answer signal is modified and differs from the setpoint value. This difference is called ‘error signal’. To recover an answer value of the system close to the setpoint, the controlling structure computes a new value for the excitation signal from the error signal via a PI controller. In PI controller mode, a signal selected among In A, In C and the oscillation amplitude and frequency shift of a PLL module can be regulated. The setpoint value is fixed either from a value entered in the controlling software or from a voltage applied at inputs In B or In D. A safe-tip function, that is useful when using a submodule as Z controller to control the tip-sample distance, can be used to avoid tip crashes. The regulated and error signals are displayed, respectively, at outputs Out A, Out C and Out B, Out D.

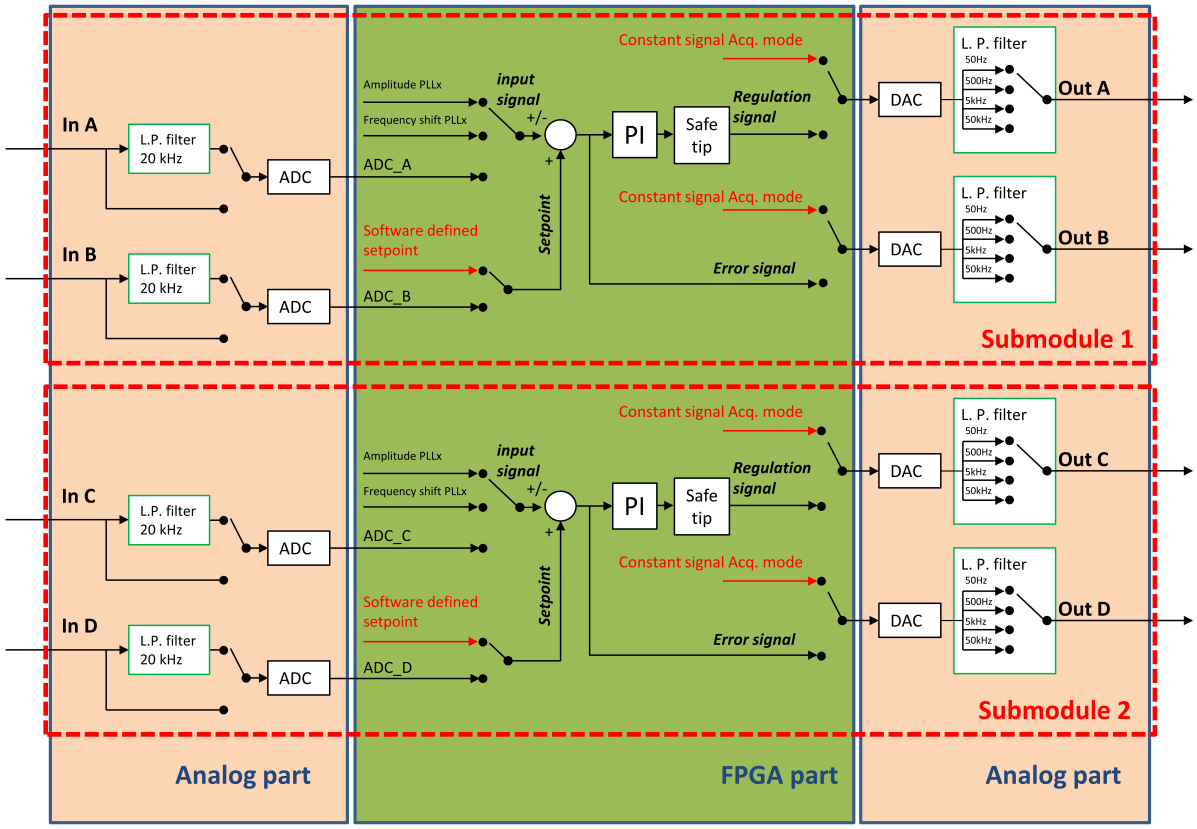

Figure 17: Structure of the Math module. The module consists of two identical submodules that can be used in acquisition and signal generation mode or in PI controller mode. In the acquisition mode, signals at inputs In A, In B, In C and In D are digitized and their value read by the controlling software. In addition, signals of constant value can be generated at outputs Out A, Out B, Out C and Out D. In PI controller mode, a signal selected among In A, In C and the oscillation amplitude and frequency shift of a PLL module can be regulated. The setpoint value is fixed either from a value entered in the controlling software or from a voltage applied at inputs In B or In D. A safe-tip function, that is useful when using a submodule as Z controller to control the tip-sample distance can be used to avoid tip crashes. The regulated and error signals are displayed, respectively, at outputs Out A, Out C and Out B, Out D . Butterworth filters with cutoff frequencies of 20 kHz for the inputs and 50 Hz, 500 Hz, 5 kHz or 50 kHz for the outputs can be applied to supress the noise.

2.2.3 Subharmonic module

The Subharmonic module is a four-channel pulse-sequence generator. Each channel enables the generation of different periodic pulse signals of user-defined duration. The pattern of the signals are shown in figure 18. The channels are all synchronized with the NCO of one of the four PLL/Kelvin modules. The period of the signals at outputs A, B and C consists of a number n of periods of oscillation of the reference signal generated by the NCO and of duration T_{NCO}. For the output D, the period is $2nT_{NCO}$. At outputs A and B, a signal consists of two pulses of user-defined duration $Li1$ and $Li2$, where $i = 1$ corresponds to output A and $i = 2$ to output B. For each signal, a shift of value $S11$ for channel A and $S21$ for channel B can be set between the reference signal and the first pulse. At the same time, a phase shift of value $S12$ for channel A and $S22$ for channel B can be set between the two generated pulses. At output C, a square wave with a set duty cycle of 50% can be generated. Similarly, the signal at output D consists of a square wave with a set duty cycle of 50% and phase shifted with $S4$ with regard to the start of the reference signal. Protocols such as oscillating cantilever driven adiabatic reversal (OSCAR), or interrupted OSCAR (iOSCAR) in magnetic resonance force microscopy (MRFM) [33] can be generated. The module is useful for all experiments involving long time constants in sensor reaction and in which long measurement cycles have to be used, for instance in fluorescence experiments on biomaterial.

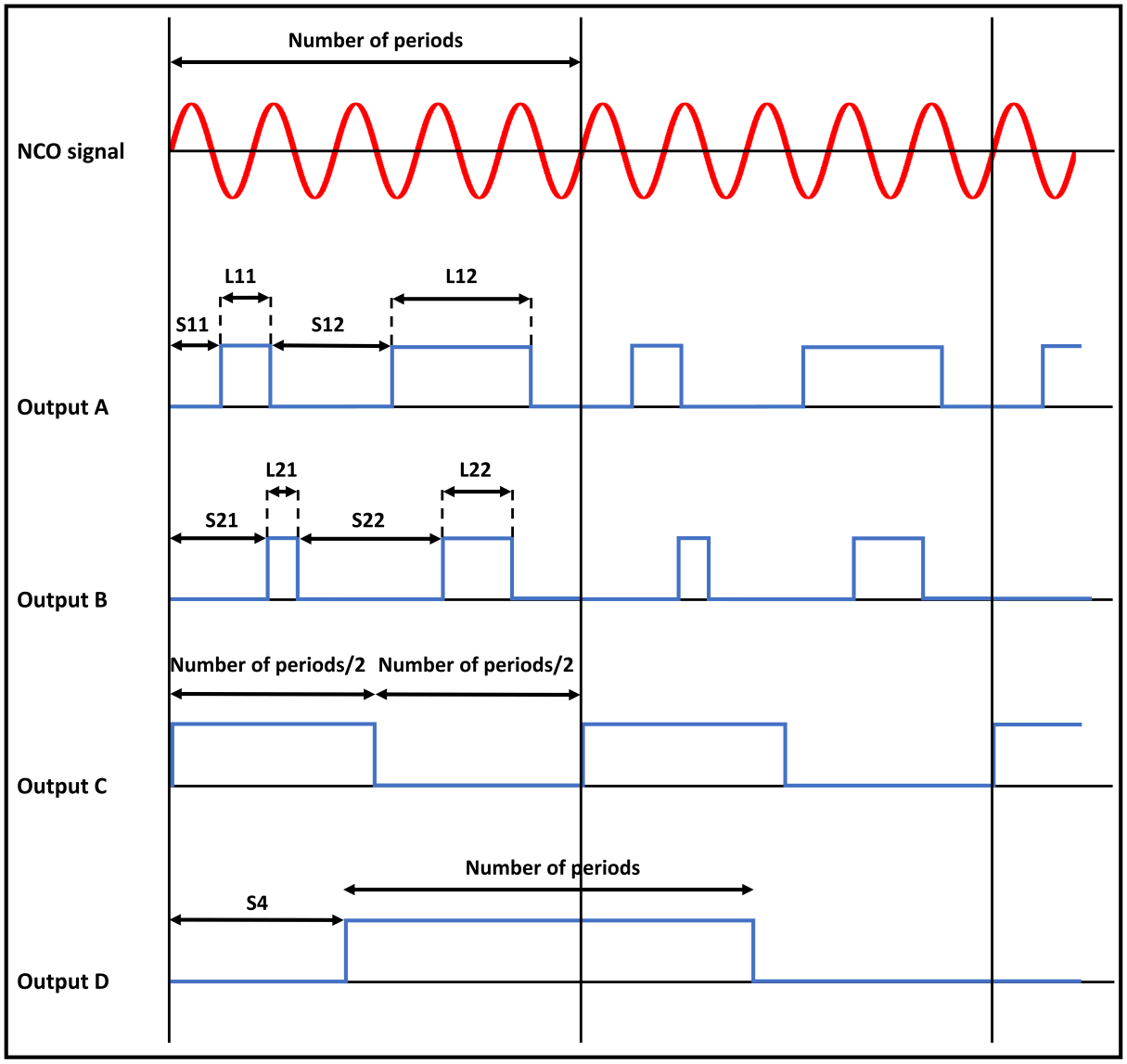

Figure 18: Patterns of pulse-sequence signals that can be generated at the four outputs of Subharmonic module. The signals are synchronized with the NCO of one of the four PLL/Kelvin modules. At outputs A and B, two pulses of user-defined duration can be generated. In addition, a shift between the reference signal and the first pulse and a shift between both pulses can be set. At outputs C and D, square waves with a set duty cycle of 50% can be generated.

2.3 Input/Output interfaces

In addition to the modules, SAPHYR has four input/output (I/O) interfaces, namely Microscope, Aux, Monitor and System, as shown in figure 19. The inputs and outputs of the Microscope interface are the physical nodes between the Microscope and the PLL/Kelvin modules in the measurement loop for dynamic SPM experiments. The excitation signals from the Microscope Output interface, for instance, are directly applied to the piezoelectric shaker of the Microscope head to excite the cantilever. Each voltage from the photodiode corresponding to the response signals of the cantilever in the vertical and lateral directions can be applied to one of the four Microscope inputs to be treated by a PLL or Kelvin module. The Aux interface furnishes additional power supplies. The Monitor interface enables the visualization of specific signals of the Microscope interface input/output parts and the System interface interfaces the external clock that can be used for the synchronization of the FPGA and the communication between the controlling software and SAPHYR.

Figure 19: View of the SAPHYR input/output (I/O) interfaces. From left to right: Microscope, Aux, Monitor and System interfaces.

2.3.1 Microscope interface

The Microscope interface consists of two parts: an input part and an output part.

Microscope input part

The Microscope input part consists of four inputs of two-pole LEMO type connectors named Microscope Input A, B, C and D. The four outputs are directly connected to the input of the four PLL/Kelvin modules and their signals can be visualized on connectors Input A, B, C and D of the Monitor Input interface. Its function is to condition each of the input signals with an Attenuator block by dividing their amplitude by 1 or 10 and by keeping or suppressing their constant component with the AC/DC function as illustrated in figure 20. Once the signals are conditioned, they can be assigned to an output via a system of switches.

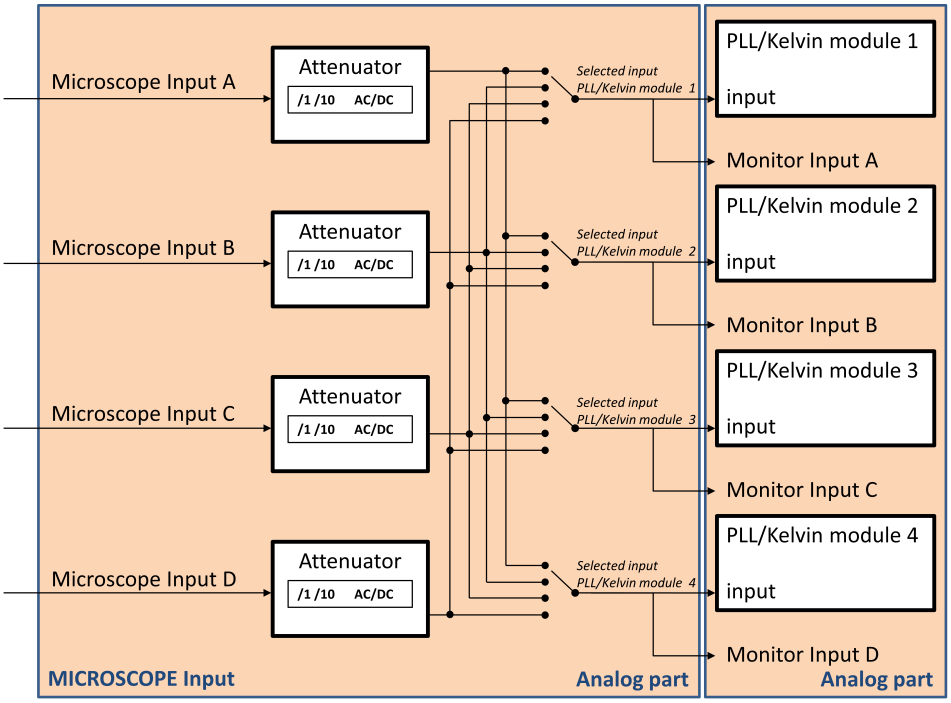

Figure 20: Structure of the Microscope Input part and its connections with the PLL/Kelvin modules and the Monitor Input connectors. Its function is to condition the input signals Microscope Input A, B, C and D by attenuating them or suppressing their DC component, and assign them to an output. The four outputs are directly connected to the input of the four PLL/Kelvin modules. The Microscope input A, B, C, and D signals can be visualized on the Monitor input A, B, C and D.

Microscope outputs part

The Microscope output part consists of four outputs. Its function is to generate for each output, Microscope Output A, B, C and D, an excitation signal that is a selection of the output signals of the PLL/Kelvin modules and the Aux interface by means of an adder and a system of switches, as illustrated in figure 21.

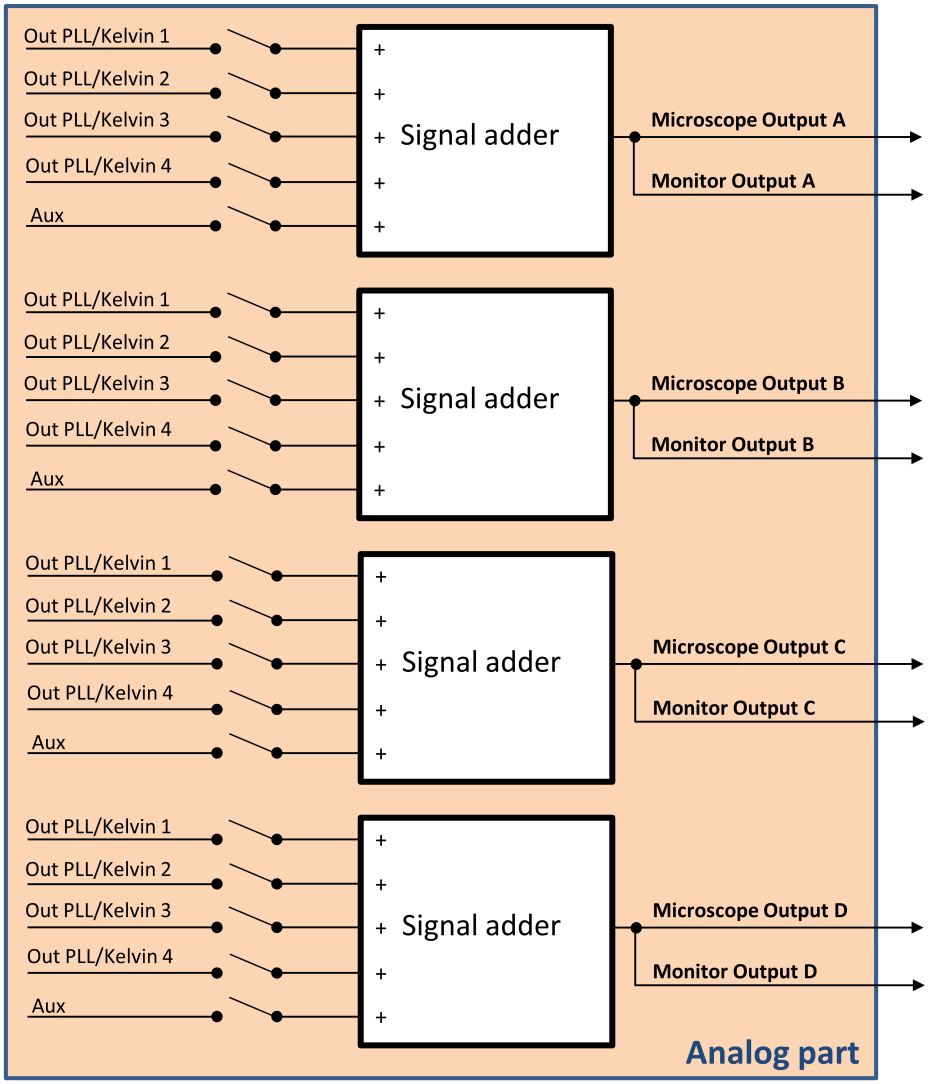

Figure 21: Structure of the Microscope output part and its connections with the PLL/Kelvin modules, Aux bloc and the Monitor Output connectors. The signal at the Microscope Output A, B, C and D outputs consists of the addition of selected signals among the PLL/Kelvin output signals and the constant signal from the Aux interface. The Microscope output A, B, C and D signals can be visualized on the Monitor outputs A, B, C and D.

2.3.2 Aux interface

The Aux interface, or Auxiliary interface, consists of one input and three outputs. It has different functions such as the conditioning of the Aux Input signal that can be added to the PLL/Kelvin output signals in the Microscope Output interface. The conditioning consists of the same Attenuator structure as in the Microscope Input interface structure (figure 20). Besides this, it can generate a constant signal of amplitude ± 10 V on the Aux output from a value entered in the controlling software. Its last function is to provide two secondary Power supplies from the SAPHYR power supply on the two outputs Aux Power A and B of four-pole LEMO type connectors.

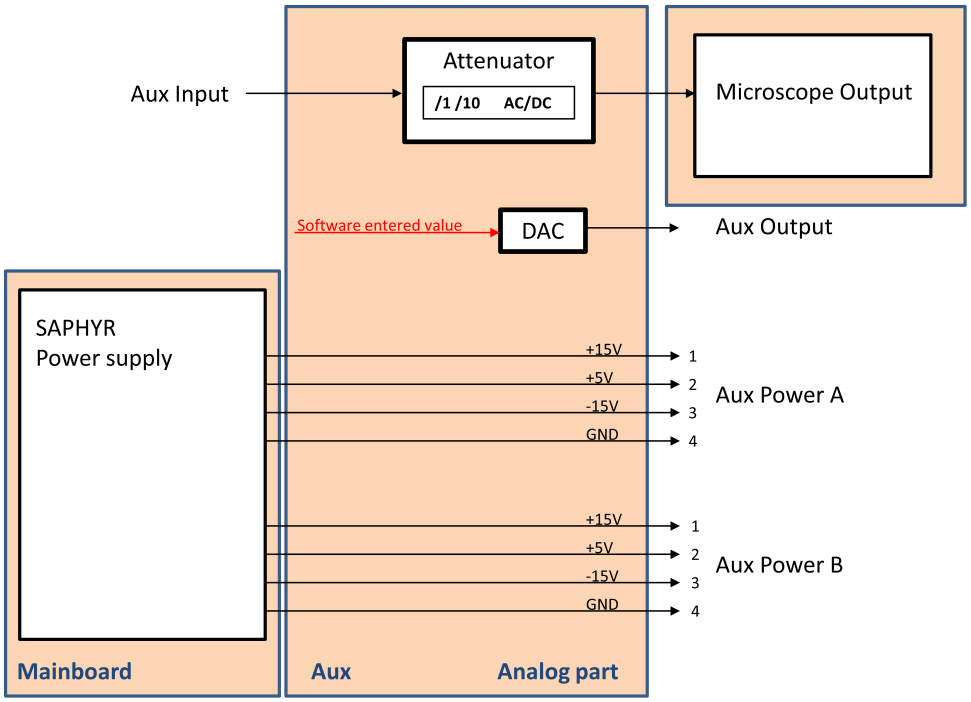

Figure 22: Scheme of the Aux interface. The structure interfaces the Aux Input signal used in the Microscope Output interface with an attenuator structure for its conditioning where an attenuation by a factor 10 or an AC/DC function can be applied. Additionally, it provides three outputs; one for the generation of a software-defined constant signal called Aux Output and two secondary power supplies Aux Power A and B from the SAPHYR Power supply.

2.3.3 Monitor interface

The Monitor interface is used for the visualization of the previously mentioned signals Microscope Input A, B, C and D and Microscope Output A, B, C and D belonging to the Microscope interface.

2.3.4 System interface

The System interface contains the USB interface for the communication between the FPGA and the computer with the installed controlling software. External clocks for the synchronization of the FPGA instead of the internal quartz, can be plugged in the BNC Clock Input connector. The clock signal used for the synchronization of the FPGA can be visualized on the BNC Clock Output connector.

Chapter 3

Working principle of lockin amplifiers and PLLs, and algorithm for phase shift computation

Lockin amplifiers and PLLs are fundamental devices in dynamic AFM. For example, lockin amplifiers are generally used to measure the oscillation amplitude of the cantilever and the phase shift relative to the excitation signal for a given frequency. In intermittent-contact mode AFM, the value for the oscillation amplitude is used as a control parameter in the Z controller to map the sample topography. In PM-AFM [34], measurement of the phase shift variations during the interaction between the tip and the sample permits the determination of the conservative and dissipative forces. Besides this, the amplitude and phase shift values are used as control parameters by PLLs. PLLs maintain the phase shift between the input and output signals to a value defined by a setpoint. In FM-AFM, the quantity measured by the PLL, i.e. the frequency shift, is directly proportional to the interaction force gradient for small oscillation amplitudes [31]. To introduce the next chapter and complete the chapter about the SAPHYR controller, their principle will be explained in the present chapter.

3.1 Description of physical systems by a linear-system model

Before starting to explain the functioning principle of a lockin amplifier, the characteristics of linear systems will be introduced to understand which relative quantities are measured by a lockin amplifier. Linear systems are mathematical models that can be used to describe most physical systems. Under certain conditions, even highly nonlinear physical systems can often be approximated by a linear system to describe their dynamic behavior and determine their properties in a domain of validity. AFM cantilevers, for instance, show a linear behavior for small excitation amplitudes and a nonlinear one for large amplitudes.

3.1.1 Mathematical representation of linear systems by an operator

A linear system can be mathematically described by an operator H, a behavior that is characterized as follows:
if $u_{exc,1}(t)$, $u_{exc,2}(t)$ are time-dependent excitation signals, and $u_{resp,1}(t) = H\{u_{exc,1}(t)\}$ and $u_{resp,2}(t) = H\{u_{exc,2}(t)\}$ are response signals, then for any combination of excitation signals

$\alpha u_{exc,1}(t) + \beta u_{exc,2}(t)$, where α and β are real-number constants, the response signal of the linear system will be

$$H\left\{\alpha u_{exc,1}(t) + \beta u_{exc,2}(t)\right\} = \alpha H\left\{u_{exc,1}(t)\right\} + \beta H\left\{u_{exc,2}(t)\right\} = \alpha u_{resp,1}(t) + \beta u_{resp,2}(t).$$

In the case of invariant linear systems, if $u_{resp}(t)$ is the answer to excitation $u_{exc}(t)$, then the answer to $u_{exc}(t-\tau)$ is $u_{resp}(t-\tau)$, $\forall\, \tau$, an arbitrary constant.

3.1.2 Time domain response of a linear system

In linear systems, the relation between the time domain response signal $u_{resp}(t)$ and the excitation signal $u_{exc}(t)$ can always be represented by the integral

$$u_{resp}(t) = \int_{-\infty}^{\infty} h(t,\tau) u_{exc}(\tau) d\tau,$$

where $h(t)$ represents the time-varying impulse response and corresponds to the response u_{resp} of the system to an excitation $u_{exc}(t) = \delta(t)$, where $\delta(t)$ corresponds to a Dirac impulse.

In the case of invariant linear systems, $h(t,\tau) = h(t-\tau)$ and $u_{resp}(t)$ are linked to $u_{exc}(t)$ by a convolution integral

$$\begin{aligned} u_{resp}(t) &= h(t) * u_{exc}(t) \\ &= \int_{-\infty}^{\infty} h(t-\tau) u_{exc}(\tau) d\tau. \end{aligned}$$

3.1.3 Frequency domain response of an invariant linear system

The frequency domain response of an invariant linear system is given by the Fourier transform FT of u_{resp}

$$\begin{aligned} FT\left\{u_{resp}\right\} &= FT\left\{h(t) * u_{exc}(t)\right\} \\ &= FT\left\{h(t)\right\} FT\left\{u_{exc}(t)\right\}. \end{aligned}$$

If we set $\overline{U_{resp}}(f) = FT\left\{u_{resp}(t)\right\}$, $\overline{U_{exc}}(f) = FT\left\{u_{exc}(t)\right\}$ and $\overline{H}(f) = FT\left\{h(t)\right\}$, we can write the previous relation

$$\overline{H}(f) = \frac{\overline{U_{resp}}(f)}{\overline{U_{exc}}(f)},$$

where $\overline{H}(f)$ is called transfer function of the invariant linear system. It is a complex number that describes the relation in the frequency domain between the excitation and the response signals.
As a complex number, it can also be written:

$$\overline{H}(f) = |\overline{H}(f)|e^{j\varphi(f)},$$

where $|\overline{H}(f)|$ represents modulus, norm or magnitude, $\varphi(f)$, the phase or phase shift (figure 23b) and f the frequency in hertz.
As illustrated in figure 23a, when a signal $u_{exc}(t) = U_0 sin(2\pi ft + \phi_0)$ is applied at the input of an invariant linear system, the modulus and the phase of the transfer function appear in the response signal u_{resp} as follows:

$$u_{resp}(t) = |\overline{\boldsymbol{H}}(\boldsymbol{f})|\, U_0 sin(2\pi ft + \phi_0 + \boldsymbol{\varphi}(\boldsymbol{f})).$$

If $|\overline{H}(f)| < 1$, u_{resp} is attenuated in comparison to u_{exc}, whereas, $|\overline{H}(f)| > 1$, it is amplified.

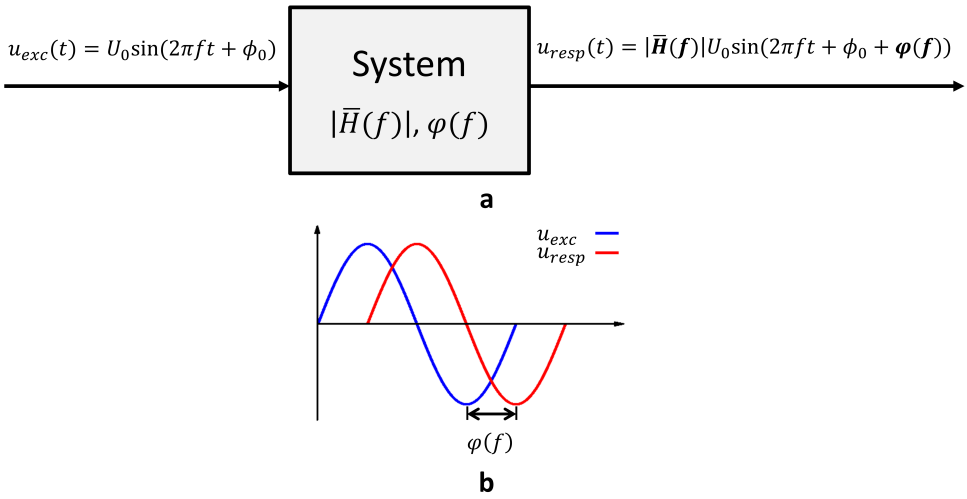

Figure 23: (**a**) Schema illustrating the relation between the expression of the input $u_{exc}(t)$ and output $u_{resp}(t)$ signals for an invariant linear system. (**b**) Phase shift $\varphi(f)$ between u_{exc} and u_{resp} signals.

3.2 Functioning principle of lockin amplifiers

The function of a lockin amplifier is to build a vector from the excitation signal and the response signal of an invariant linear system in order to compute the modulus and the phase of the transfer function of the system.

3.2.1 Building of a vector from u_{exc} and u_{resp}

A vector $\overrightarrow{V}$(X,Y) can be built by multiplying u_{resp} by u_{exc} and u_{resp} by $u_{exc,90°}$, where $u_{exc,90°}$ is u_{exc} shifted by $90°$ and is equal to $U_0 cos(2\pi ft + \phi_0)$.

Hence,

$$\begin{aligned} u_{exc}u_{resp} &= U_0 sin(2\pi ft + \phi_0)|\overline{H}(f)|U_0 sin(2\pi ft + \phi_0 + \varphi(f)) \\ &= \frac{1}{2}|\overline{H}(f)|U_0^2\Big(cos(\varphi(f)) - cos(4\pi ft + 2\phi_0 + \varphi(f))\Big) \end{aligned} \tag{3.1}$$

and

$$u_{exc,90^\circ} u_{resp} = U_0 cos(2\pi ft + \phi_0)|\overline{H}(f)|U_0 sin(2\pi ft + \phi_0 + \varphi(f)) \\ = \frac{1}{2}|\overline{H}(f)|U_0^2\Big(sin(\varphi(f)) + sin(4\pi ft + 2\phi_0 + \varphi(f))\Big) \tag{3.2}$$

As we can see, equations 3.1 and 3.2 both consist of a time-independent component $\frac{1}{2}|\overline{H}(f)|U_0^2 cos(\varphi(f))$ and $\frac{1}{2}|\overline{H}(f)|U_0^2 \sin(\varphi(f))$ and a time-dependent component $\frac{1}{2}|\overline{H}(f)|U_0^2 cos(4\pi ft + 2\phi_0 + \varphi(f))$ and $\frac{1}{2}|\overline{H}(f)|U_0^2 sin(4\pi ft + 2\phi_0 + \varphi(f))$ of frequency $2f$. By suppressing the time-dependent component with an ideal bandpass filter, we can build the in-phase X and quadrature Y components of vector $\overrightarrow{V}$:

$$X = \frac{1}{2}|\overline{H}(f)|U_0^2 cos\varphi(f) \tag{3.3}$$

$$Y = \frac{1}{2}|\overline{H}(f)|U_0^2 sin\varphi(f) \tag{3.4}$$

3.2.2 Computation of $|\overline{H}(f)|$, $\varphi(f)$ and oscillation amplitude $A(f)$

From equations 3.3 and 3.4, the modulus $|\overline{\boldsymbol{H}}(\boldsymbol{f})|$ and the phase $\boldsymbol{\varphi(f)}$ of the transfer function $\overline{H}(f)$ can be computed as follows:

for modulus$|\overline{\boldsymbol{H}}(\boldsymbol{f})|$,

if $\boldsymbol{r}$ is the length of the vector $\overrightarrow{\boldsymbol{V}}$,

$$r = \sqrt{X^2 + Y^2} \\ = \sqrt{\left(\frac{1}{2}|\overline{H}(f)|U_0^2 cos\left(\varphi(f)\right)\right)^2 + \left(\frac{1}{2}|\overline{H}(f)|U_0^2 sin\left(\varphi(f)\right)\right)^2} \\ = \sqrt{\frac{1}{4}|\overline{H}(f)|^2 U_0^4} = \frac{1}{2}|\overline{H}(f)|U_0^2$$

and

$$\boxed{|\overline{H}(f)| = \frac{2r}{U_0^2}}$$

for phase $\boldsymbol{\varphi(f)}$,

$$\boxed{\varphi(f) = arctan\left(\frac{Y}{X}\right)}$$

and

for oscillation amplitude $A(f)$,

the oscillation amplitude of the response signal $A(f)$ can easily be computed from $|\overline{\boldsymbol{H}}(\boldsymbol{f})|$, as $\boldsymbol{A(f)} = |\overline{\boldsymbol{H}}(\boldsymbol{f})|\boldsymbol{U_0}$; it is generally this quantity that is returned by the lockin amplifier instead of $|\overline{\boldsymbol{H}}(\boldsymbol{f})|$

$$\boxed{A(f) = \frac{2r}{U_0}}$$

The principle schema of the mathematical operations done in a lockin amplifier to obtain $A(f)$ and $\varphi(f)$ is given in figure 24.

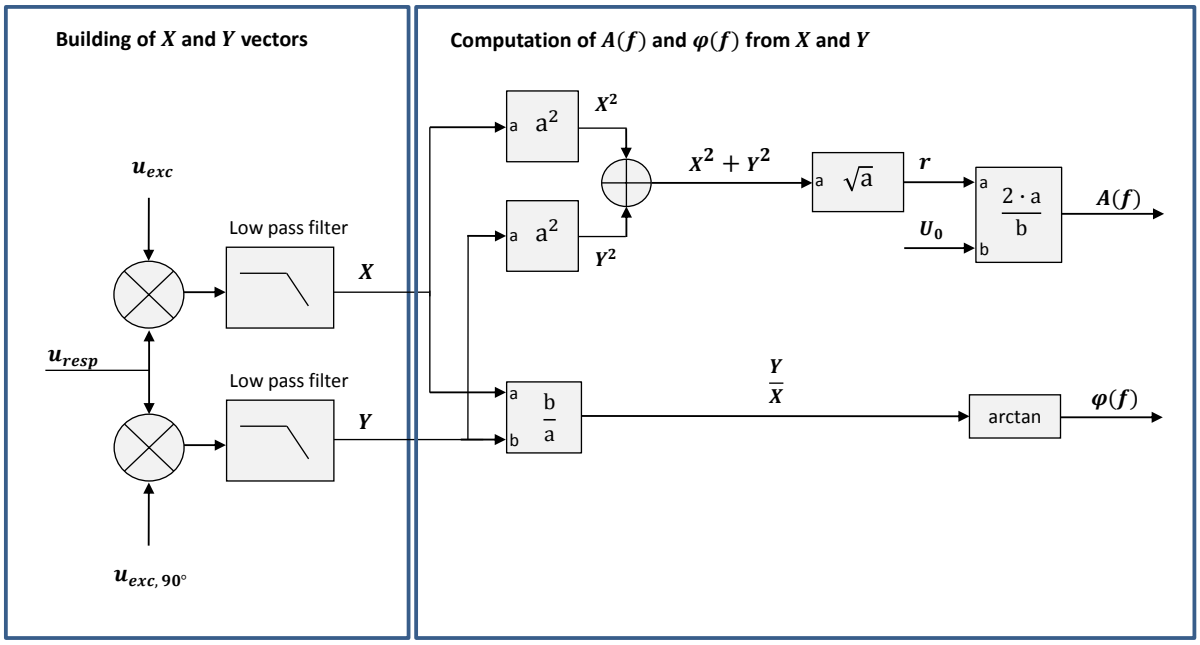

Figure 24: Mathematical operations done in a lockin amplifier. The first part consists in building two vectors X and Y from the response signal u_{resp}, the excitation signal u_{exc}, and u_{exc} shifted by $90\,^\circ$, $u_{exc,90^\circ}$. X and Y are obtained by filtering the product u_{resp} by u_{exc} and u_{resp} by $u_{exc,90^\circ}$. In the second part, the oscillation amplitude of the response signal $A(f)$ and the phase shift $\varphi(f)$ between u_{exc} and u_{resp} are computed. $A(f)$ is obtained by applying Pythagoras theorem to X and Y and multiplying the result by a factor $\frac{2}{U_0}$, where U_0 is the oscillation amplitude of u_{exc}. $\varphi(f)$ is obtained from arctan of ratio Y by X.

3.3 Functioning principle of PLLs

A PLL is a device that maintains the phase shift $\varphi(f)$ between its input and output equal to a set-point value φ_{set} by increasing or decreasing the excitation-signal u_{exc} reference-frequency f_{ref} by a value Δf called frequency shift as illustrated in figure 25a. Several cycles of Δf computation are necessary for the PLL to find the frequency shift Δf_{set} for which $\varphi(f_{ref} + \Delta f_{set}) = \varphi_{set}$ (figure 25b). A new frequency shift Δf_{i+1} is computed by measuring the phase shift value $\varphi(f_i)$ obtained from a previous excitation signal frequency $f_i = f_{ref} + \Delta f_i$, as illustrated in figure 26, where i is the i^{th} computation iteration. $\varphi(f_i)$ is then subtracted from φ_{set} and Δf_{i+1} is computed by PI controller from $\varphi(f_{set}) - \varphi(f_i)$ and added to reference frequency f_{ref} so that $f_{i+1} = f_{ref} + \Delta f_{i+1}$ is the new frequency of u_{exc}.

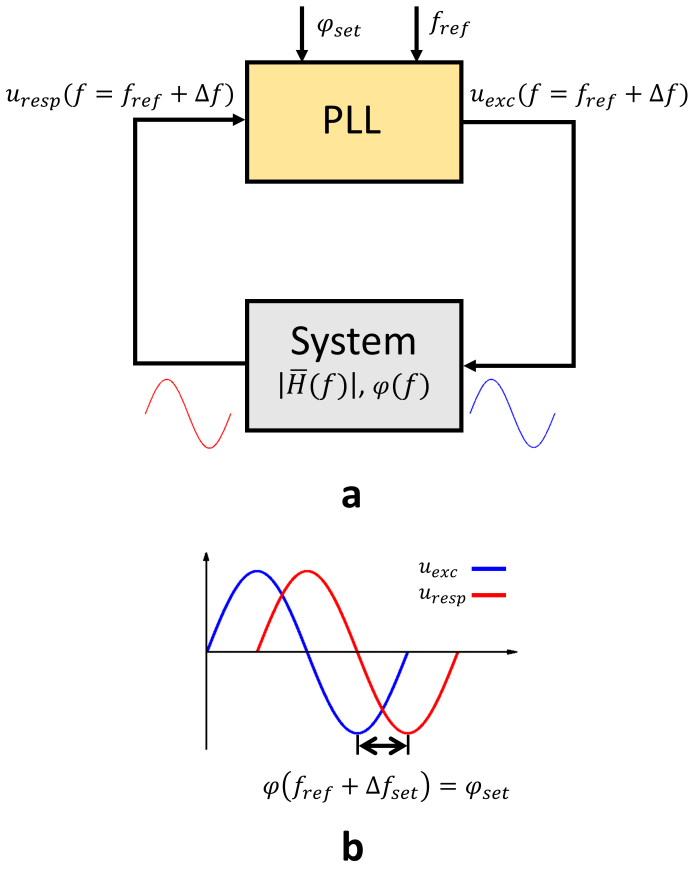

Figure 25: (**a**) Feedback loop for phase shift $\varphi(f)$ controlling of an invariant linear physical system (in AFM, the cantilever) by a PLL. The PLL maintains $\varphi(f)$ to a setpoint value φ_{set} by increasing or decreasing the excitation signal reference frequency f_{ref} by a value Δf, called frequency shift. (**b**) Several cycles of phase shift measuring and Δf computing are necessary to find the frequency shift Δf_{set} for which $\varphi(f_{ref} + \Delta f_{set}) = \varphi_{set}$. The frequency $f_{ref} + \Delta f_{set}$ remains unchanged as long as no perturbation requires the computation of a new Δf_{set} different from the previous one.

If, after n cycles, $\varphi(f_{ref} + \Delta f_n) = \varphi_{set}$, then for all j subsequent frequency shift computation cycles, $\Delta f_{n+j} = \Delta f_n = \Delta f_{set}$, where j is an integer. The frequency of u_{exc} stays equal to $f_{ref} + \Delta f_n$ as long as no new perturbation occurs.

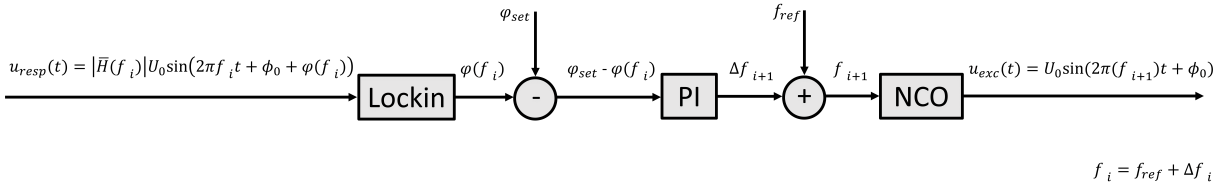

Figure 26: Computation by PLL of the new frequency f_{i+1} of excitation-signal u_{exc} from the measured phase shift $\varphi(f_i)$, where $f_i = f_{ref} + \Delta f_i$ and i is an integer corresponding to the i^{th} iteration of frequency shift computation. The phase shift of invariant linear system $\varphi(f_i)$ is first measured by the lockin amplifier and then subtracted from setpoint φ_{set}. The frequency shift Δf_{i+1} is computed by PI controller from $\varphi_{set} - \varphi(f_i)$ and added to reference frequency f_{ref} so that $f_{i+1} = f_{ref} + \Delta f_{i+1}$ is the new frequency of u_{exc}. If, after n iterations of that operation, $\varphi(f_n) = \varphi_{set}$, then for all j subsequent frequency shift computations, $\Delta f_{n+j} = \Delta f_n$ and the frequency of u_{exc} stays equal to $f_{ref} + \Delta f_n$ as long as no new perturbation occurs.

3.3.1 PLLs applied to AFM for resonance frequency detection

In dynamic mode AFM, the tip-sample interaction has as a consequence the shift of the cantilever resonance curves, as illustrated in figure 27. The shift direction and its magnitude depend on the type of interaction - attractive or repulsive - and on the tip-sample distance. This shift is characterized by a shift of the resonance frequency by a quantity Δf – called frequency shift – compared to the resonance frequency $f_{res,0}$, when no interaction occurs. The sign of the frequency shift depends on the interaction type – negative for an attraction and positive for a repulsion. The shape of the shifted resonance curve ideally is similar to the one, when no interaction occurs. This can be obtained more or less when performing non contact AFM in UHV with the Z controller using the frequency shift of the first flexural mode as control parameter. Most of the time, however, the shape of the amplitude and phase curves is distorded due to the non-linearity of the interaction that introduces harmonics in the response signal. The new resonance frequencies, $f_{res,attract}$ for an attractive interaction and $f_{res,repuls}$ for a repulsive one, can be detect by a PLL as illustrated in figure 28 for an attractive interaction. The PLL detects the new resonance frequency $f_{res,attract}$ by computing the frequency shift $\Delta f_{res,attract}$ for whicht the phase shift $\varphi(f_{ref} + \Delta f_{res,attract})$ corresponds to the setpoint $\varphi_{set} = \varphi(f_{ref})$, where the reference frequency f_{ref} is the initial cantilever resonance frequency $f_{res,0}$. After n cycles of Δf_i computation and evaluation of phase $\varphi(f_i)$ at frequency $f_i = f_{ref} + \Delta f_i$, $\Delta f_n = \Delta f_{res,attract}$, and the new frequency $f_{res,attract} = f_{ref} + \Delta f_{res,attract}$ is then detected. The value of $\Delta f_{res,attract}$ remains unmodified as long as the magnitude of the interaction stays unchanged.

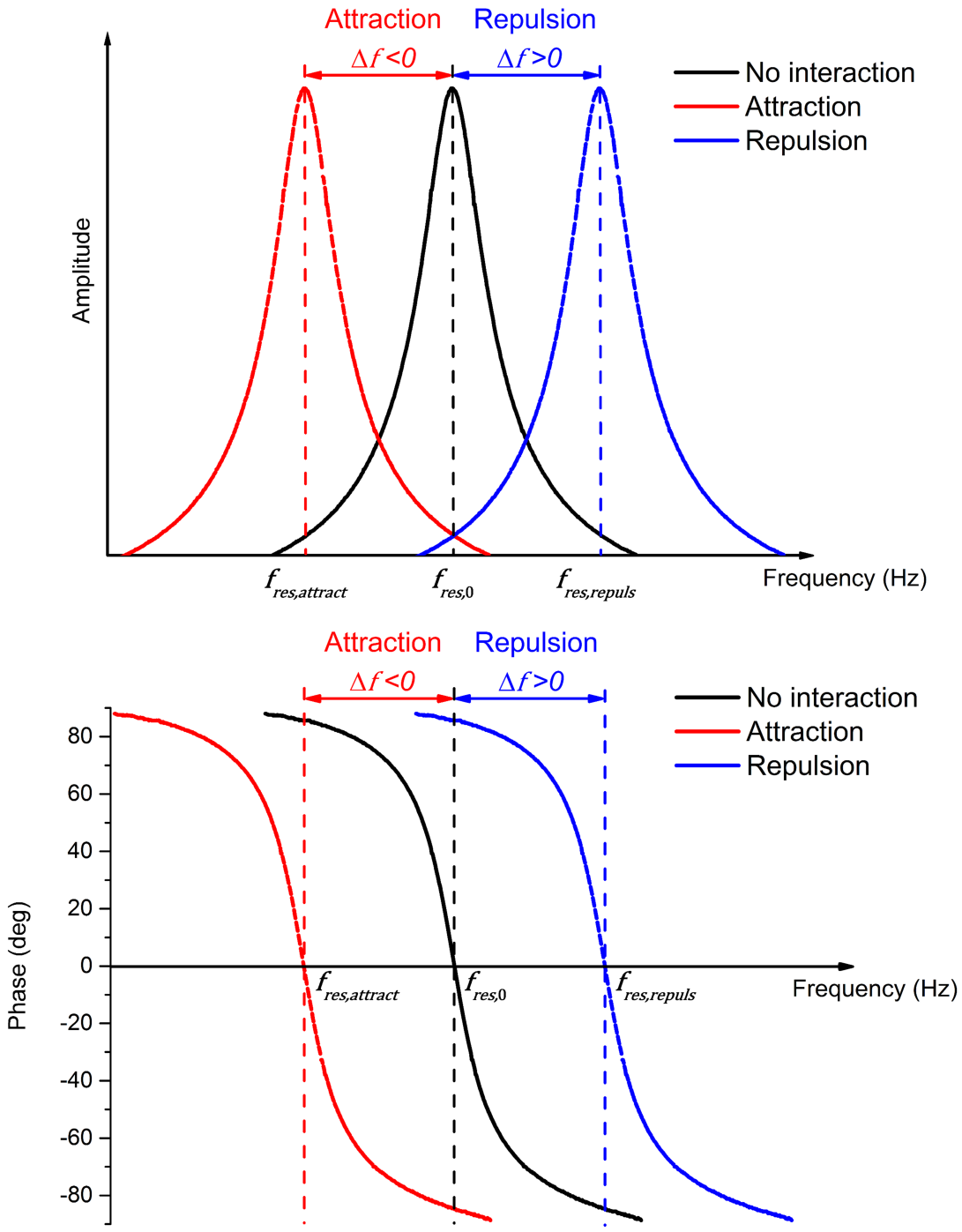

Figure 27: Cantilever resonance curves shift in dynamic mode AFM due to tip-sample interaction (curves are supposed ideal). The shift direction and its magnitude depend on the type of interaction, meaning attractive (red curve) or repulsive (blue curve), and on the tip-sample distance. The frequency $f_{res,0}$, corresponding to the peak frequency of the resonance curve in amplitude, when there is no interaction, is increased by a value Δf, i.e. frequency shift, which is negative in the case of an attractive interaction and positive in the case of a repulsive one. The new resonance frequencies are $f_{res,attract}$ and $f_{res,repuls}$.

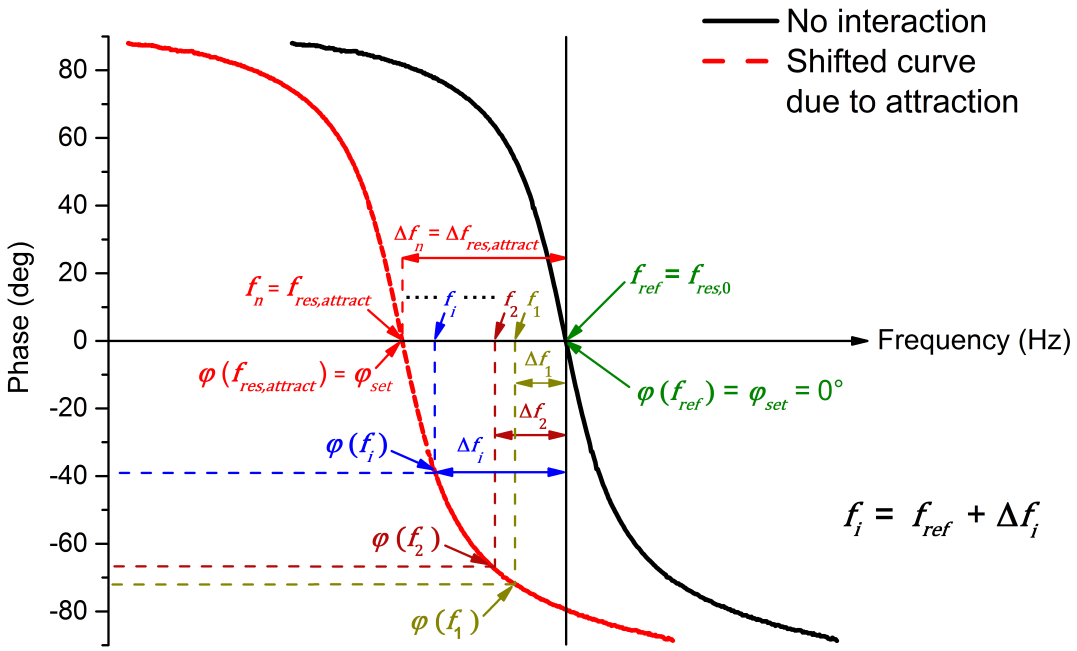

Figure 28: Research of the new cantilever resonance frequency $f_{res,attract}$ by a PLL during tip-sample interaction (in our case, attractive). When a tip-sample interaction occurs, the cantilever resonance curve (black) is shifted (red) and so the resonance frequency, in contrast to the initial one, $f_{res,0}$. A PLL can be used to find the new resonance frequency by computing a $\Delta f_{res,attract}$ for which $\varphi(f_{ref} + \Delta f_{res,attract}) = \varphi_{set}$, where f_{ref} corresponds to $f_{res,0}$ and $\varphi_{set} = \varphi(f_{ref})$ to the phase at the corresponding frequency. n cycles of Δf_i computation and evaluation of phase $\varphi_(f_i)$ at $f_i = f_{ref} + \Delta f_i$ are necessary until $\Delta f_n = \Delta f_{res,attract}$ and the resonance frequency $f_{res,attract} = f_{ref} + \Delta f_{res,attract}$ are detected.

Chapter 4

Algorithm for phase shift computation in the lockin and the PLL technique

The frequency-dependent phase shift $\varphi(f)$ of the cantilever transfer function is a fundamental parameter in dynamic AFM. Its high-precision measurement by PLLs enables the indirect determination of quantities like the interaction forces between the cantilever tip and the sample surface [31] as well as the elasticity modulus [11], via computed frequency shift. As mentioned in chapter 3, the determination of the phase shift is generally done by lockin amplifiers, by computing $arctan(\frac{Y}{X})$, from in-phase X and quadrature Y components. In the initial version of the SAPHYR lockin amplifier, $arctan(\frac{Y}{X})$ is not computed in real time by the lockin but by the controlling software. The lockin-based PLLs in SAPHYR used the approximation $arctan(\frac{Y}{X}) \sim \frac{Y}{X}$ to determine the phase necessary for the computation of the frequency shift in real time. The problem with this approximation is that it restrains phase variations to values around 0°. Hence, the functioning of the PLL stays stable as long as no perturbation occurs. Perturbations, for example, when the cantilever picks up materials on the sample surface in FM-AFM or in case of large changes in material properties when measuring contact resonances, result in a large phase shift variation, far from 0°. In that case, due to the approximation, the erroneous measured phase shift leads to the computation of erroneous frequency shift values. To overcome this problem of instability, I developed and implemented an algorithm in SAPHYR for the precise real-time computation of the phase in the [−180;180[degree domain. This algorithm actually represents a good solution for phase shift computation in the lockin and PLL techniques. For instance, since their full analog easyPLL, the Nanosurf company, have never developed any digital PLL. Their first attempt to develop a digital PLL was done with the SAPHYR controller that was based on the previously mentioned approximation. For that reason, I suggested to patent the algorithm, which was accepted by Unitectra, the associated organization that manages patents of the universities of Basel and Zurich. This chapter presents the principle of the algorithm as well as its characteristics and advantages. Owing to the confidentiality of the patent, the details of the algorithm will not be given.

4.1 Principle of the algorithm

The algorithm describes a component representing blocks '$\frac{b}{a}$' and 'arctan' in figure 24 for the computation of $arctan\left(\frac{Y}{X}\right)$. The algorithm consists of four inputs **X**, **Y**, **clk_ext** and **clk_algorithm** and an output called **phase** as illustrated in figure 29. Inputs **X** and **Y** stand for in-phase and quadrature vectorial components computed by a lockin amplifier. Two digital clocks, clk_ext and clk_algorithm, synchronize the algorithm with the other components in the lockin amplifier and the computation of the phase. The algorithm is based on an iterative method using coefficients to compute the phase. The computation of $arctan\left(\frac{Y}{X}\right)$ in the [−180;180[degree domain is performed in three successive steps as illustrated in figure 30:

− computing $arctan\left(\frac{Y}{X}\right)$ in the [−90;90[degree domain from the built vectors X and Y (see subsection 3.2) with the iterative method. The phase value is computed in a number of cycles of *clk_algorithm* equal to n, the number of coefficients used by the method;

− transposing the phase value from the [−90;90[degree to the [−180;180[degree domain. Since arctan$\left(\frac{Y}{X}\right)$ gives the same value as arctan$\left(\frac{-Y}{-X}\right)$ and arctan$\left(\frac{Y}{-X}\right)$, the same value as arctan$\left(\frac{-Y}{X}\right)$, the domain of returned values is extended to [−180;180[degrees by checking the sign of *X* and *Y*;

− displaying the computed phase value at lockin output after a number of periods of *clk_algorithm* corresponding to n.

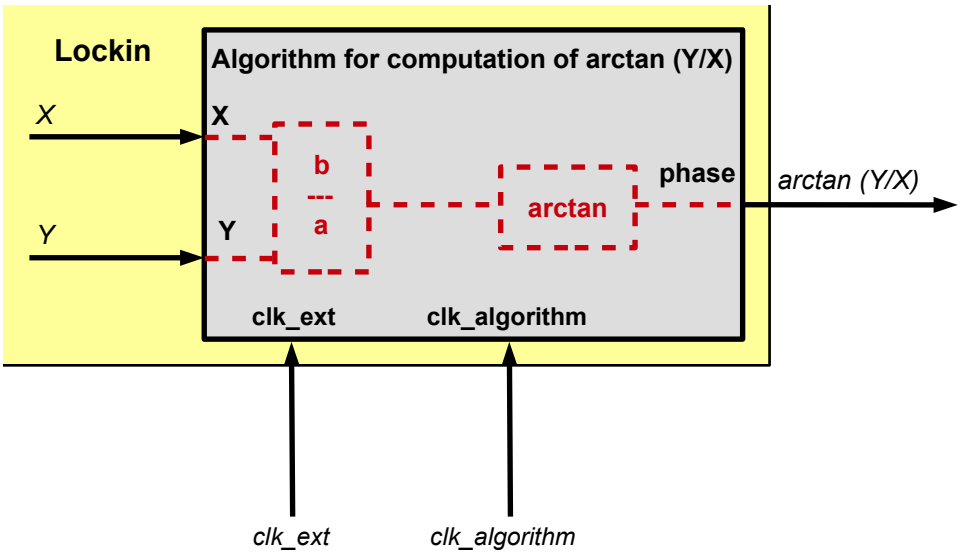

Figure 29: Schematic representation of the component for the computation of $arctan\left(\frac{Y}{X}\right)$ described by the algorithm. The component represents blocks '$\frac{b}{a}$' and 'arctan' in figure 24. It consists of four inputs: **X** and **Y** for the in-phase and quadrature vectorial components computed in the lockin amplifier, **clk_ext** and **clk_algorithm** for the synchronization of the component functioning with the other components in the lockin amplifier and for the synchronization of the phase calculation done by the algorithm. The output **phase** displays the value of the computed phase at the lockin output.

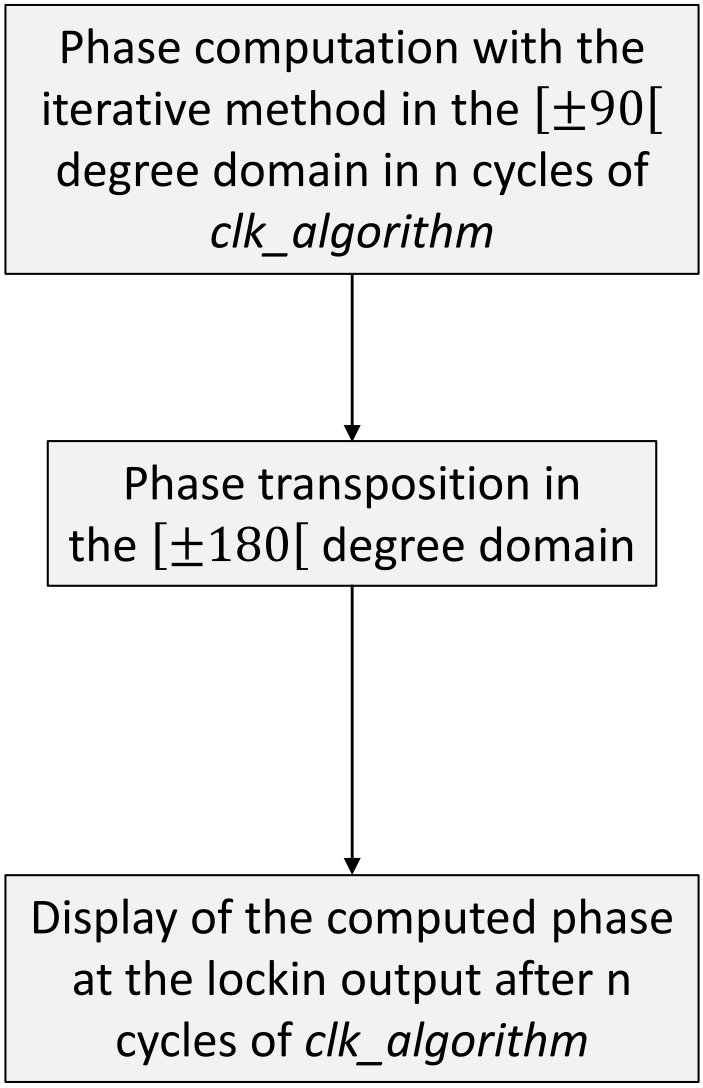

Figure 30: Successive steps for the computation of $arctan(\frac{Y}{X})$ from in-phase X and quadrature Y components in the algorithm. Phase computation is performed in three steps: in the first step, the algorithm computes the phase in the [−90;90[degree domain in n cycles of *clk_algorithm* clock corresponding to the number of coefficients; in the second step, the phase is transposed in the [−180;180[degree domain, finally, after n cycles of *clk_algorithm* clock, the phase value is displayed at the lockin output.

4.2 Characteristics and advantages of the algorithm

The algorithm was developed with the VHDL language in order to be implemented on the FPGA of the SAPHYR controller. This VHDL code can, however, be implemented on any FPGA and the algorithm may be implemented in an ASIC. The structure of the VHDL code for the algorithm was programmed in a 'parameterize and compile' way; thus the user only needs to enter the parameters corresponding to his application and compile the code, which saves time. The user parameters that need to be defined are the bit length of X and Y, the bit length of the phase and the number of coefficients. The algorithm uses two clocks, *clk_ext* and *clk_algorithm*, for the synchronization of the component in figure 29 with other components in the lockin and the synchronization of phase computation. The synchronization works as illustrated in figure 31. First, on the rising edge of *clk_ext* (1), *X* and *Y* are saved by the component, then, at the first rising edge of *clk_algorithm* (2), phase computation from these values is initialized. Finally, after n cycles of *clk_algorithm* (3), the computed phase value is displayed at the lockin output. The algorithm is thought for computing $arctan(\frac{Y}{X})$ in one cycle of *clk_ext* corresponding to the main clock of the lockin amplifier as seen in figure 32a. However, it is possible that more than one cycle of *clk_ext* may be necessary to compute the phase due to the fact that the maximum frequency of *clk_algorithm* that can be generated by the FPGA is too small. In this case, the phase can still be computed as illustrated in figure 32b under the condition $f_{clk\_ext} = \frac{m_{clk\_ext}}{n} f_{clk\_algorithm}$, where f_{clk_ext} is *clk_ext* frequency, $f_{clk\_algorithm}$, *clk_algorithm* frequency, m_{clk_ext} number of cycles of *clk_ext* necessary for phase computation and n the number of coefficients used by the algorithm. The results of the algorithm simulation in the Quartus environment show that the computed values for $arctan(\frac{Y}{X})$ perfectly fit the values obtained from computation softwares, as illustrated in figure 33 and shown in the table in appendix A.

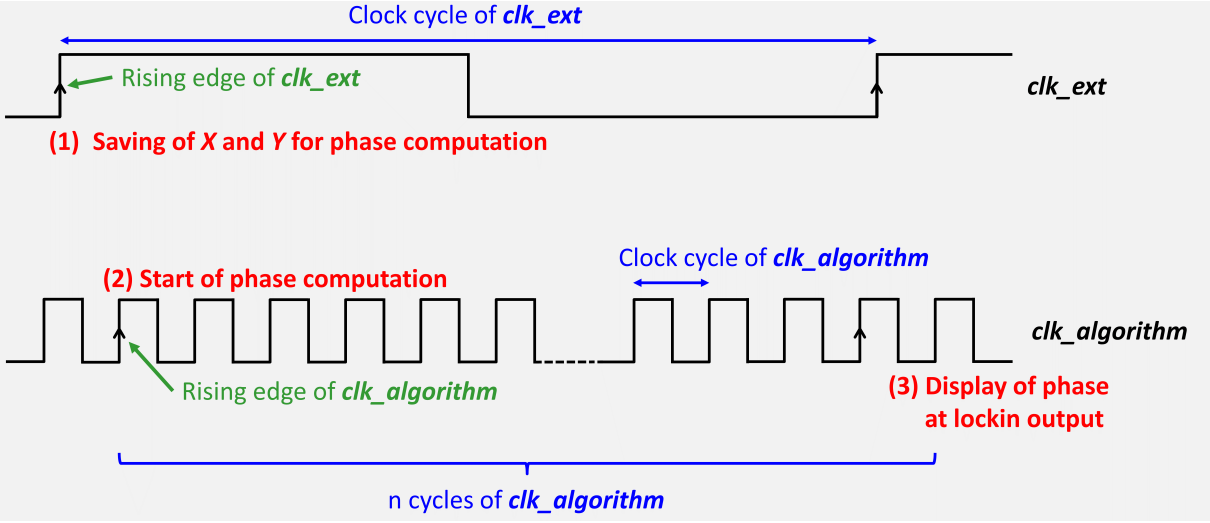

Figure 31: Chronograms of *clk_ext* and *clk_algorithm* for the synchronization of $arctan(\frac{Y}{X})$ computation. At the first rising edge of *clk_ext* (**1**), in-phase *X* and quadrature *Y* components are saved. Then, at the first subsequent rising edge of *clk_algorithm* (**2**), the computation of $arctan(\frac{Y}{X})$ starts. Finally, after n cycles of *clk_algorithm* (**3**), the computed value of $arctan(\frac{Y}{X})$ is displayed at the lockin output.

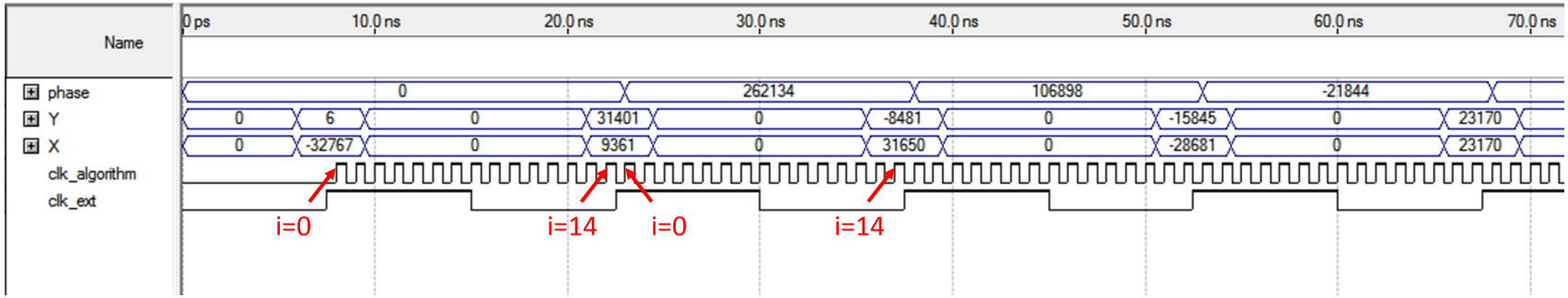

a

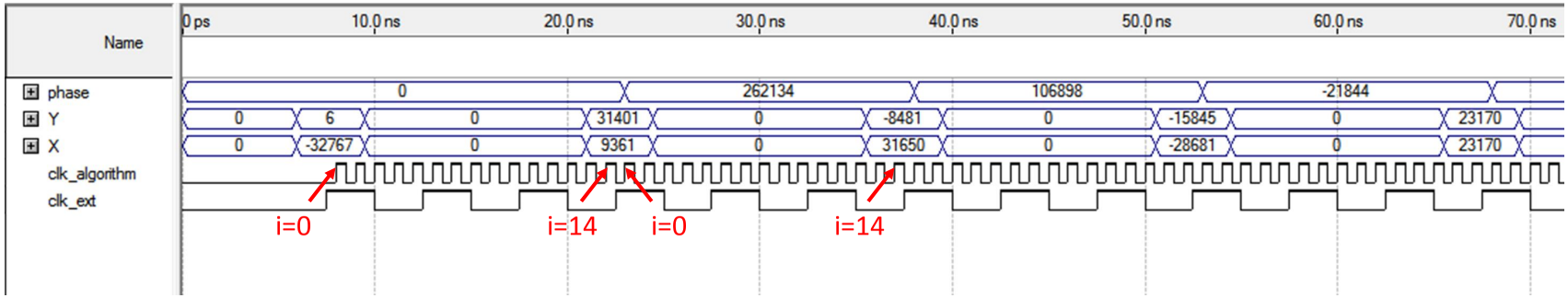

b

Figure 32: Simulation of phase computation by algorithm VHDL code in the Quartus environment from Altera. The code was configured with parameters adapted to SAPHYR, meaning bit lengths of 16 for X and Y, 19 for phase and number of coefficients of 15. At the rising edge of clk_ext, at 7.5 ns, the values −32767 for X and 6 for Y are saved in the component. At the subsequent rising edge of clk_algorithm (i=0), the algorithm starts to compute the phase. After 15 cycles of clk_algorithm (i=14) the phase is computed and its value 262134 displayed at the lockin output. **a** At the following rising edge of clk_ext, new values for X and Y (9361 and 31401) are saved in the component. At the subsequent rising edge of clk_algorithm, the algorithm starts to compute the corresponding phase. **b** The process is similar to that in **a** except that the new values for X and Y are saved after 3 cycles of clk_ext. The algorithm hence allows the computation of phase on several cycles of clk_ext .

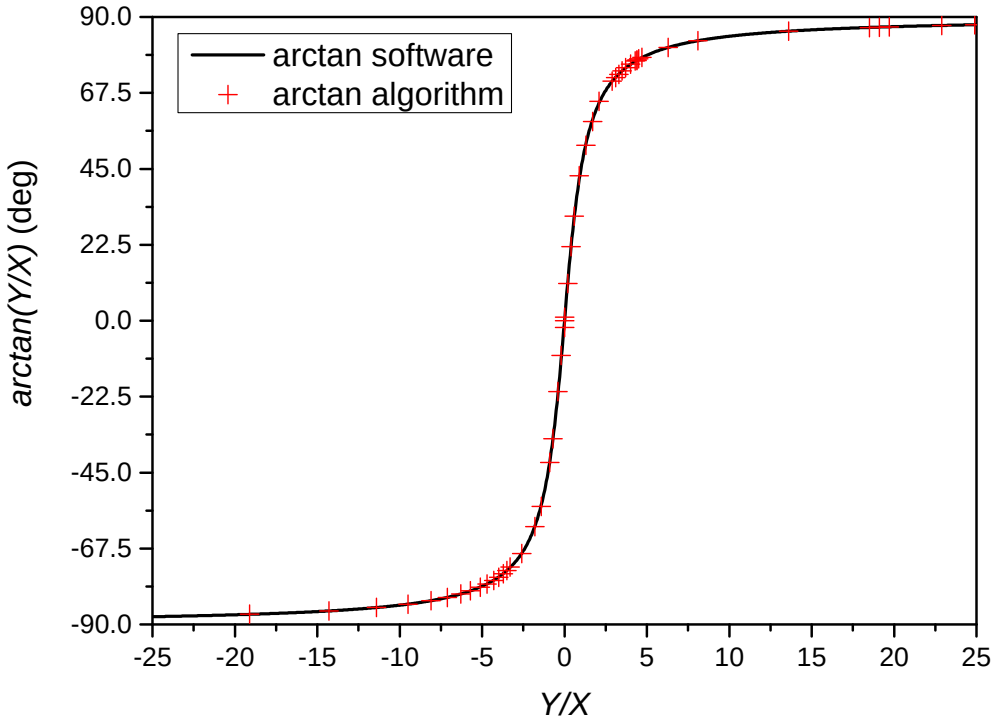

Figure 33: Arctan as a function of ratio *Y/X* curves. The values represented by red crosses were computed with the algorithm and are compared with values obtained from software computation (here Excel) and represented by black curve.

4.3 Patenting of my invention

Since this algorithm shows great potential, especially in the SPM domain, I proposed to patent it. Prof. Ernst Meyer, form the university of Basel and Dr. Wolfgang Henggeler from Unitectra agreed. My invention was officially received by the European Patent Office and registered on July 24, 2015, as shown in appendix B and C.

Chapter 5

Software to control SAPHYR

Software is an essential part of the SAPHYR controller: the different modules (PLL, Math and Subharmonics) have to be configured to work properly. In the same time, the correct signals have to be generated to move the scanners. In addition, data have to be recorded and saved during experiments. At the beginning of the present work, an initial software for the control of SAPHYR, based on C++ language, has already been developped but was incomplete: all the functionnalities of the modules have not been programmed and experiments such as mappings of topography and physical quantities or measurement of quantities-displacement curves could not be performed. For this reason, I decided to develop a new software for the control of SAPHYR. The new software, whose graphical user interface is based on Nanonis software from Specs Zurich (Zurich, Switzerland) for the controlling of their SPM controller, was developed in the LabVIEW environment for the rapidity and simplicity of programming as well as debugging. The present chapter is an insight into the functioning structure and the different user interfaces (UI) of the new software.

5.1 Structure of SAPHYR software

The choice of the software's structure is important and must be done carefully to ease the programming, improve the speed and avoid any troubles like the blocking of the software during its execution.

5.1.1 Execution of the software

The execution of the software, also called session, is divided in 3 parts sequentially executed and representing each a state of the execution; these states are the initialization, the running and the stopping as illustrated in figure 34.

Initialization state

During the initialization state, the graphical interfaces of the software and the registers in the controller are configured with the values and the parameters from the previous session of the software. These configuration parameters and values are loaded from a configuration text file and read at the execution of the software or loaded by the user during the running state. The parameters and values are in the same time recorded in a data structure that represents the actual working state of the controlling system (values entered in the controls in the graphical interfaces for instance).

Running state

Once the configuration is done, the state of execution of the software is running. During this phase the software is working permanently unless the user decides to stop the software. The modules of the controller like the PLL for instance can be used and parameterized and experiments like scans or load-displacement curve measurements can be performed.

Stopping state

When quit is chosen in the main menu bar the running state is interrupted, the graphical interfaces closed and the parameters in the data structure describing the working state is saved in a configuration file that is loaded at the next session.

5.1.2 Structure of the running state

This state consists in three loops: the displaying, the parametrization and the experiments loops. The displaying loop displays the value of the quantities in the corresponding graphical interfaces. The parametrization loop parameterizes the registers in the controller for the signals like the amplitude or the frequency of the excitation signal. The experiments loop performs experiments like scans, load-displacement curves measurements or frequency sweeps.

Displaying loop

The displaying loop reads permanently the value of the quantities measured by the modules, such as the oscillation amplitudes or the phase shifts of the controller and assigns them to the corresponding displays in the graphical interfaces. The loop calibrates also the signals read from the controller.

Parametrization loop

The parametrization loop assigns to the corresponding registers in SAPHYR the values entered in a control in a graphical interface. It saves also the value assigned to the corresponding place in the data structure. The assignation is managed by a structure in LabVIEW called event structure that identifies which control has its value changed or when a button was pressed by the user and executes in these cases a specific function: for instance when the value of the frequency control ‘fref (Hz)’ in the PLL UI is changed, the event structure detects it, configures the corresponding register in the controller and saves the value in the data structure describing the working state.

Experiments loop

The experiments loop contains the functions necessary to perform the experiments like the frequency sweep, the Z spectroscopy, the scan or the frequency sweep. Certain experiences like the measurement of load-displacement curves or elasticity measurement need information about the cantilever dimensions or its resonance frequencies. A special graphical interface was created to specify these information, as illustrated in figure 35. The values entered are saved in the data structure. When the user wants to make a load-displacement curve for instance the corresponding function reads in the data structure these values to calibrate the results.

Management of the conflicts

All three loops defining the running state work independently from each other. Conflicts can happen when a function in a loop tries to use the USB interface to read or write data whereas the function of another loop is already using it. To avoid this kind of situation a specific component called semaphore is used. The principle of the semaphore consists in controlling the access to a resource. If a function wants to access a resource and no other function is using it, the semaphore gives the permission to continue. In the opposite case, the semaphore blocks the access until the resource is free again.

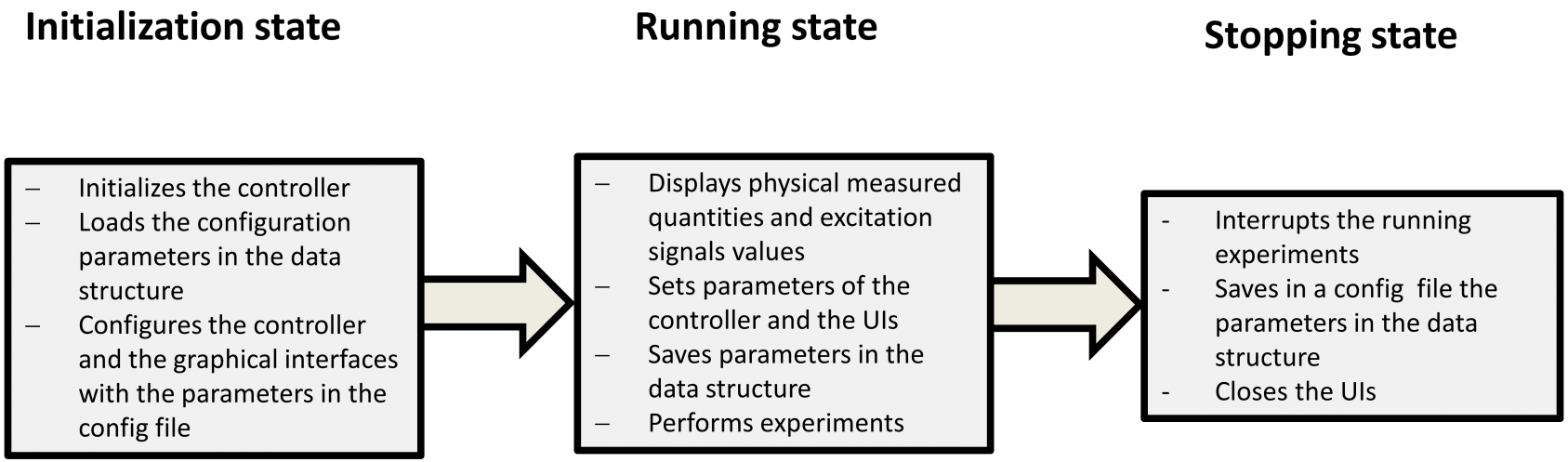

Figure 34: Structure of the execution of the software.

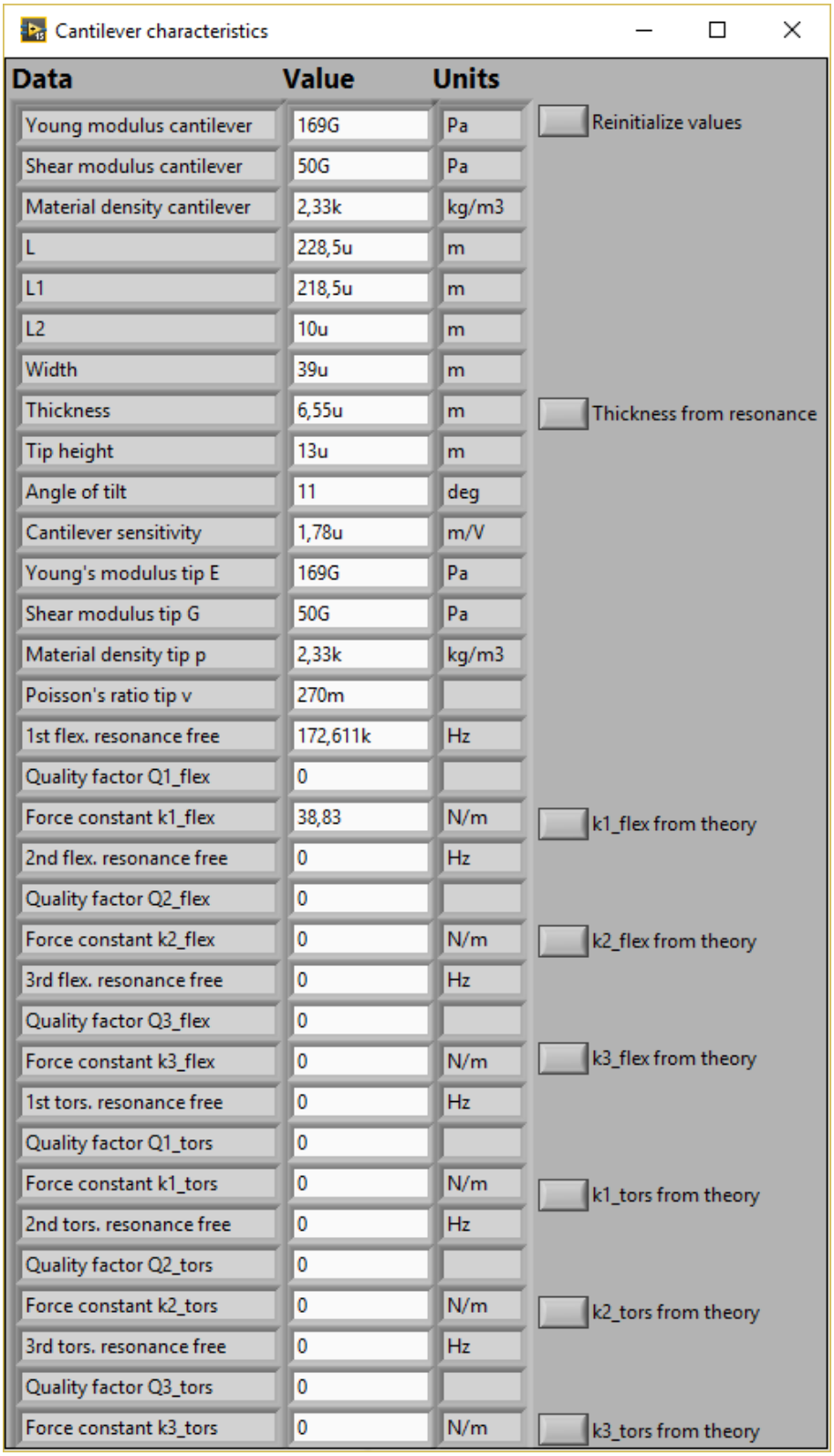

Figure 35: UI where the values for the cantilever characteristics are entered. These values are automatically used for calibrating the displays in the different UI in the software.

5.2 Graphical interfaces of SAPHYR modules

5.2.1 PLL module graphical interface

In this user interface, the PLL mode of functioning of the PLL module, either lockin or PLL, is specified and its associated parameters defined (setpoints, frequency of oscillations, ...). As seen in figure 36, the interface is divided in 5 parts: Saphyr input, Module input, Lockin, Amplitude controller and Phase controller.

Saphyr input

This part enables the selection of one of the 4 inputs of Microscope input part (figure 20) in 'Input channel'. The corresponding attenuator bloc is configured by selecting or not '/10' and 'AC coupling', for, respectively, the attenuation by a factor 10 and the suppression of the DC component of the input signal.

Module input

In this part of the UI, a compensation and/or a suppression signal can be subtracted from the input signal assigned to the PLL module by selecting, respectively, 'Compensation' and/or 'Suppression'. The DC component of the resulting signal can be suppressed by selecting 'AC coupling'. The resolution of the resulting signal before its digitizing can also be improved by selecting the maximum amplitude of the signal in 'Input range (V)' or by moving the red tip on the horizontal slide.

Lockin

When the lockin mode (subsection 2.2.1) is selected $-$ grey button in the left in Phase controller part unselected $-$, the amplitude of the excitation signal $V_{0,ref}$ is the value set in 'Drive amplitude (mV)' and its frequency f_{ref} the value set in 'fref (Hz)'. The phase at origin ϕ_0 is set in 'Phase at origin'. The resolution of the excitation signal can be improved by setting the value of its maximum amplitude in 'Amplitude max (V)'. The bandwidth of the filters used for the computation of the in-phase and quadrature components X and Y can be selected in 'Demodulator bandwidth' (subsection 3.2.1 and illustration 24). The measured phase shift $\varphi(f)$ in degrees and oscillation amplitude $A(f)$ in volts are displayed in 'Phase (deg)' and 'R (V)'.

Amplitude controller

This part enables the use of $V_{0,PI}$ as amplitude of the excitation signal (subsection 2.2.1) by pressing on the grey button in the left. The setpoint for the oscillation amplitude of the input signal is set in 'Setpoint (m)'. The value of the controller's gains K_P and K_I are set either in 'Kp' and 'Ki' or by moving the red tip of the associated horizontal slides. The values of the amplitude $V_{0,PI}$ of the excitation signal and of the oscillation amplitudes of the cantilever are displayed, respectively, in 'Diss (V)' and 'Amplitude (m)'.

Phase controller

This part enables the use of the PLL module in either the PLL or the lockin mode by pressing on the grey button in the left. In PLL mode (subsection 2.2.1), the setpoint is set in 'Setpoint (deg)'. As for the amplitude controller, the value of the controller's gains K_P and K_I are set either in 'Kp' and 'Ki' or by moving the red tip of the associated horizontal slides. The phase error value corresponding to $\Delta\varphi$ is displayed in 'Phase error'. The computed frequency shift Δf is displayed in 'Frequency shift (Hz)'. A lock range set in 'Lock range' can be defined to avoid too large frequencies of the NCO to be generated; in that case, if the frequency shift is larger than the value in lock range, the frequency of the excitation signal is the value set in 'Lock range'.

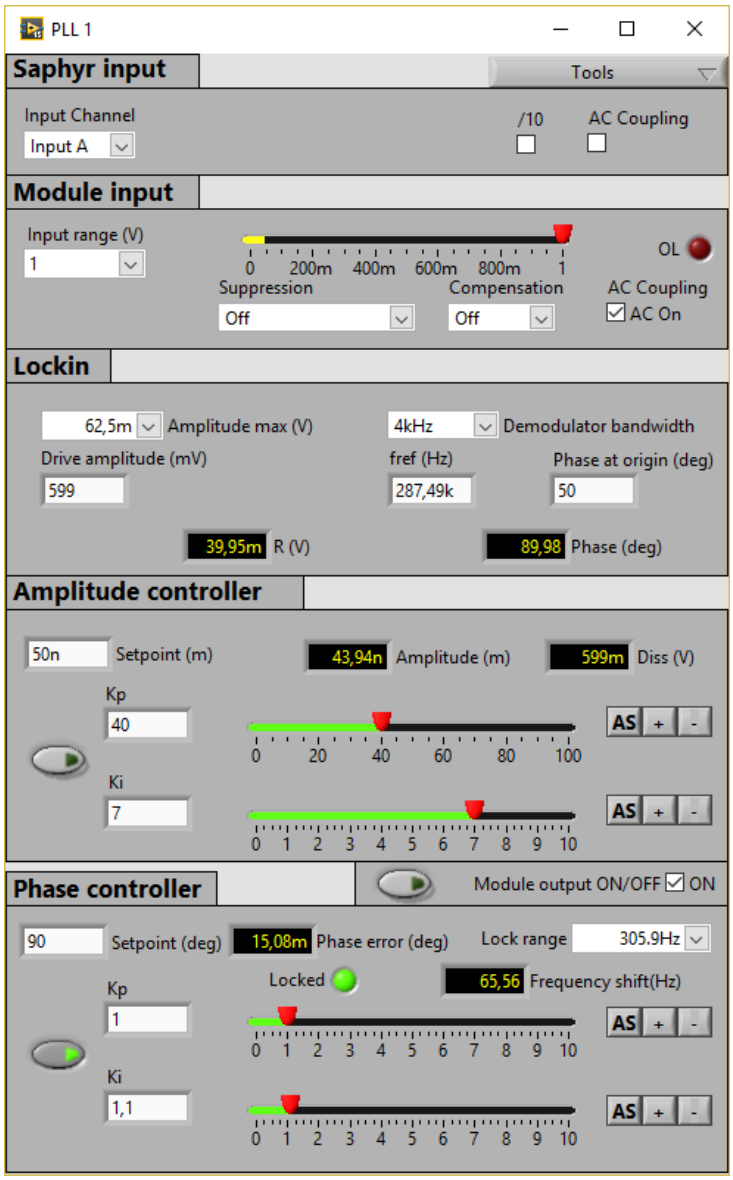

Figure 36: UI of the PLL module.

5.2.2 Subharmonics module

The Subharmonics UI (figure 37) enables the parameter definition of patterned signals (figure 18) at the four outputs of Subharmonics module (subsection 2.2.3). In the 'Reference signal' part, a PLL is chosen as reference for the time scale associated with the signal pattern in 'Reference PLL'. The duration of the repeatidly generated signal is defined by the time corresponding to a number of periods of oscillations – set in 'Number of periods' – generated by the NCO of the selected PLL. In the 'Output A' part, the duration of the pulses is detemined in 'Pulse length L11' and 'Pulse length L12'. The first pulse is shifted from reference signal by a time defined in 'Shift S11' and both pulses are shifted by a duration defined in 'Shift S12'. The polarity of the signal may be inverted by selecting 'Invert signal'. In Output B part, the description is the same as for the Output A part. The two pulses can be displayed or not by selecting or unselecting 'Pulse 11' and 'Pulse 12'. In Combined signals of outputs A and B part, Outputs A and B can be configured to generate periodically a signal whose pattern is an alternation of the patterns defined in Output A and Output B parts. The output at which this pattern must be generated is selected in 'Signal output' and can be Output A , Output B or both outputs. The polarity of the signal may be inverted by selecting 'Invert signal'. In the Output C part, the generation of the square wave is enabled by selecting 'Pulse 3'. Additionally, the polarity of the signal can be inverted by selecting the option 'Invert signal'. Similarly to Output C part, in Output D part, the generation of the square wave is enabled by selecting 'Pulse 4'. The signal can be shifted with regard to the reference signal in 'Shift 4' and its polarity inverted by selecting 'Invert signal'.

5.2.3 Configuration of the Microscope input and output

The Inputs configuration UI (figure 38) enables the assignation of one of the four inputs of Microscope inputs part (figure 20) to a PLL/Kelvin module in 'Input channel'. In addition, it enables the configuration of each of the 4 inputs of the Microscope inputs part by setting or not an AC coupling for the suppression of the DC component of the input signal in 'AC Coupling' and an attenuation gain of 10 in '/10'. The Microscope outputs configuration UI (figure 39) enables the configuration of the signal at each of the 4 outputs of the Microscope outputs part (figure 21). The output signals consist of the combination of selected signals among the four PLL/Kelvin modules output signals and the input signal of Aux interface (figure 22). Additionally, the UI enables the configuration of the input of the Aux signal by setting an AC coupling in 'Aux AC Coupling' and an attenuation gain in 'Aux /10'.

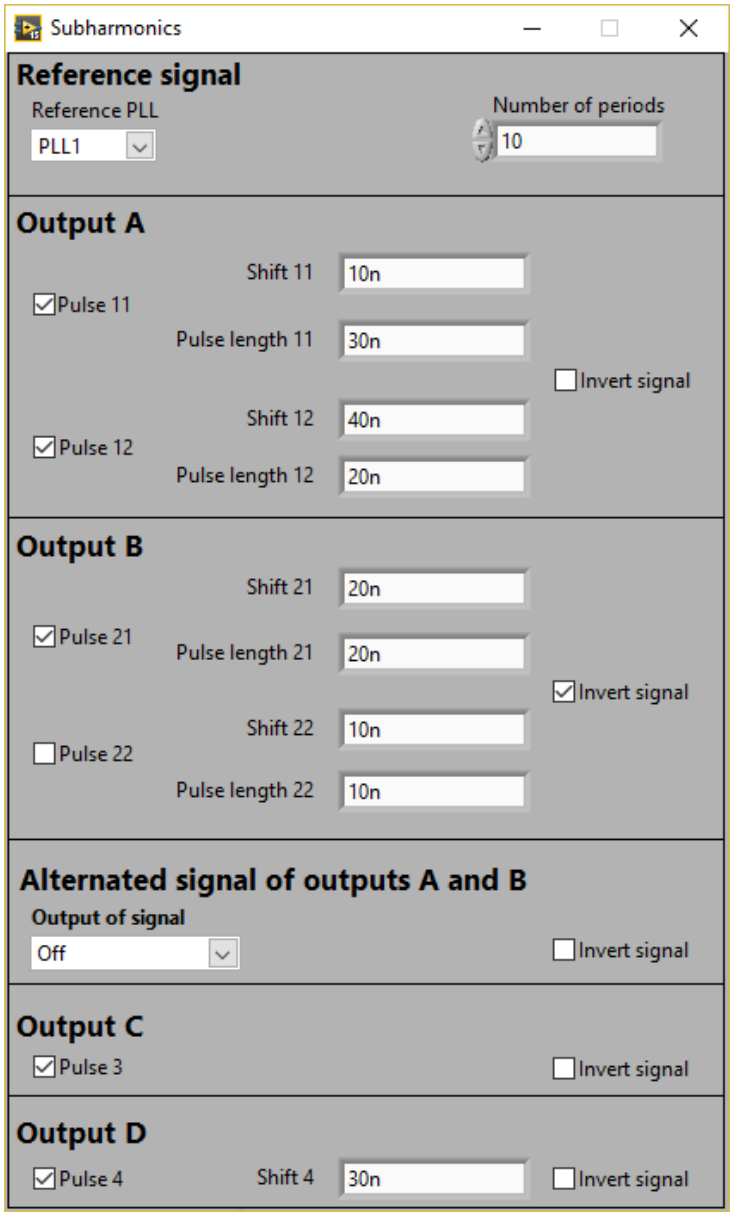

Figure 37: UI for the parametrization of the four signals generated at the four outputs of Subharmonics module. The four signals are synchronized by the NCO of the selected PLL/Kelvin module in 'Reference PLL'. The duration of the signals is a multiple of the period of the signal generated by the NCO and is set in 'Number of periods'. In output A, the parametrization of the two pulses that form the signal is done. These parameters are the pulse lengths set in 'Pulse length 11' and 'Pulse length 12' the shift of the first pulse with regard to the reference signal set in 'Shift 11' and the shift between both pulses set in 'Shift 12'. The user can decide to display or not a pulse in 'Pulse 11' and 'Pulse 12'. The polarity of the signal can be inverted by selecting 'Invert signal' as well. The same functionnalities stand for Output B. In Combined signals of outputs A and B part, an alternation of the signals defined in Output A and Output B parts can be generated at one of or both outputs A and B. In output C and D parts, a square wave can be generated by selecting 'Pulse 3' and/or 'Pulse 4'. In addition, a shift between the reference signal and the square wave at output D can be defined in 'Shift 4'.

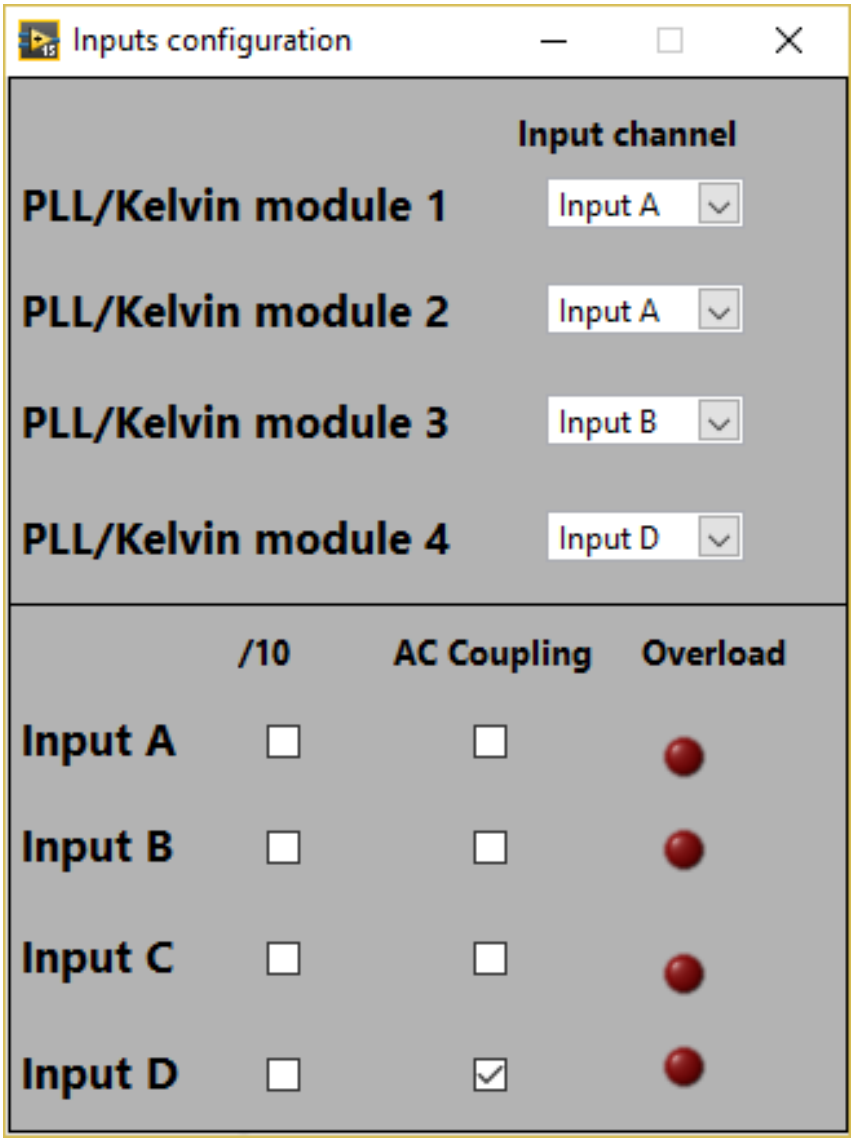

Figure 38: UI for the assignation of an input of Microscope inputs part (figure 20) to a PLL/Kelvin module in 'Input channel' and the configuration of the inputs of the Microscope inputs part. The signals at each input can be attenuated by a factor 10 set in '/10' or their DC component can be suppressed by an AC Coupling function set in 'AC coupling'.

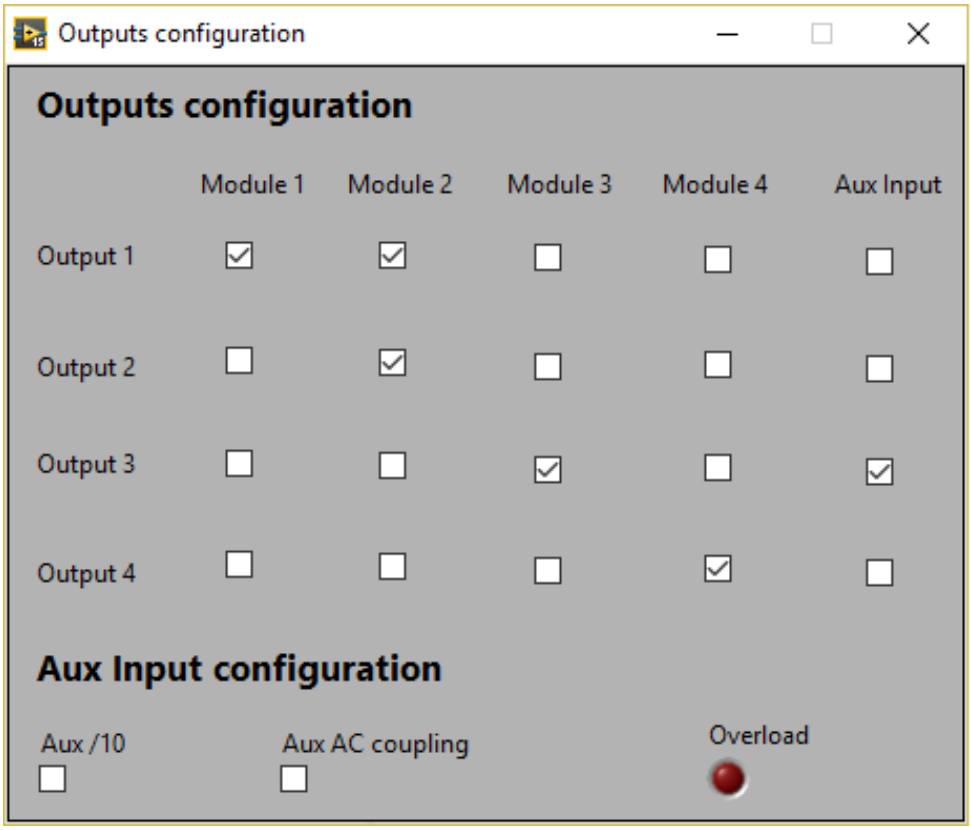

Figure 39: UI for the configuration of the signal at each of the 4 outputs of the Microscope outputs part (figure 21). Each output signal consists of the combination of selected signals among the four PLL/Kelvin modules and the input signal of Aux interface. In addition, the UI enables the treatment of the Aux input signal by setting an AC coupling in 'Aux AC coupling' and an attenuation gain in 'Aux /10'.

5.3 Three-dimensional mapping of the topography and physical properties of samples

AFM microscopes can map the topography and local physical properties of samples in a three-dimensional space by moving the cantilever with piezoelectric scanners in a volume formed by a cuboid in the direction of length X, width Y and height Z, as illustrated in figure 40.

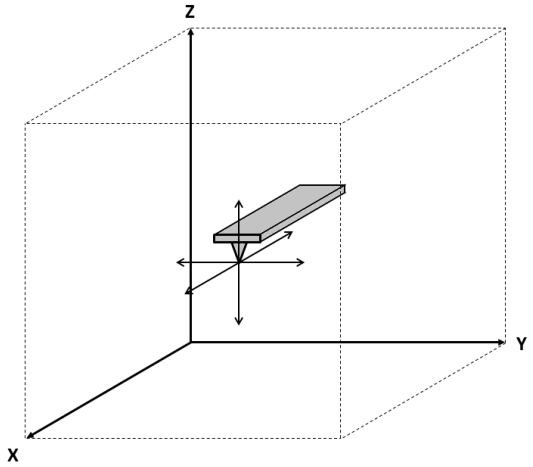

Figure 40: Schematic representation of a cantilever moving in a cuboid in the X, Y and Z directions.

The answer of a piezoelectric scanner to an applied voltage is an expansion or a contraction of its shape whose intensity and direction depend, respectively, on the amplitude and polarity of the voltage. In the ideal case, this answer is proportional to the applied voltage and characterized by a coefficient called calibration factor C that is generally expressed in meters/volt. By 'ideal case' we mean that the effect of nonlinearities, hysteresis and creep characteristics of piezoelectric scanners used in open loop are not taken into account. In SAPHYR, three Math submodules are necessary for the generation of these voltages. The submodules are generally configured (see subsection 2.2.2) as follows: two in acquisition and signal generation mode to scan in the X and Y directions, and one configured in controlling mode to control the tip-sample distance in the Z direction. As the outputs can only generate voltages of $\pm$ 10 V, a preamplifier characterized by an amplification gain G may be used between the Math submodule output and the input of the piezoelectric scanner to sweep a larger distance, as seen in figure 41. The expansion or contraction (displacement) of the piezoelectric material d in meters as a function of the *voltage* of a Math submodule output is, in the ideal case, given by the relation

$$d = voltage \cdot G \cdot C$$

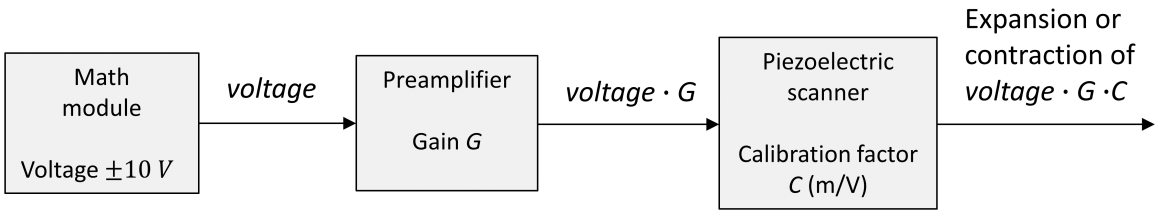

Figure 41: Interconnections of the Math submodule output, preamplifier, piezoelectric scanner and signals at their outputs.

When performing a three-dimensional mapping or when recording load-displacement curves, the scan dimensions (length, width, displacement and their steps) in meters have to be defined by the user. For this reason, the amplification gain G of the preamplifiers and the calibration factor C of the piezoelectric scanners have to be set by the user in order to convert the scan dimensions to the corresponding voltage in accordance with equation $d = voltage \cdot G \cdot C$, where d is the displacement of the piezoelectric material and *voltage* the voltage generated by the Math submodule. In SAPHYR software, a UI enables these parameters to be set for the scanners in the X, Y, Z directions, as illustrated in figure 42.

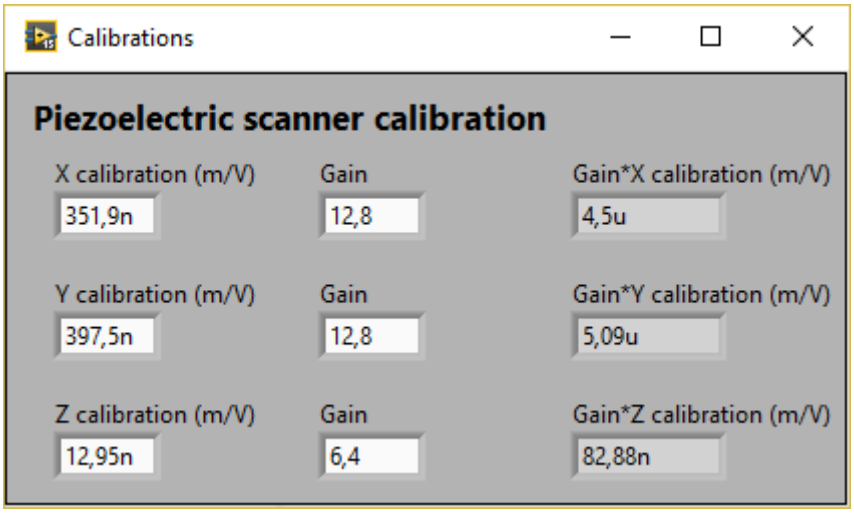

Figure 42: Graphic interface for the setting of the amplification gain G and the calibration factor C for the X, Y and Z direction scanners.

Z controller

The Z controller UI is used to regulate the tip-sample surface distance (Z direction) as a function of a parameter specified in 'Controller input'. This parameter depends on the measuring mode and can be the cantilever frequency shift (FM mode) or the cantilever oscillation amplitude (intermittent-contact mode) measured by one of the 4 PLL modules specified in 'PLL reference'; but it can also be an external voltage that corresponds to the vertical deflection signal of the cantilever (contact mode). For this purpose, a Math submodule, configured in PI controller mode (subsection 2.2.2), modifies the voltage value of the specific output until the measured parameter value, 'Input value', reaches the value specified in 'Setpoint'. The difference between the input value and the setpoint is displayed in 'Error'. The speed and the precision of the regulation are characterized by the proportional 'Kp' and integral 'Ki' gains of the controller. When measuring in dynamic mode, the safe-tip function can be used to avoid tip crashes: in this case, the cantilever is retracted to its lowest position (maximum retraction) as soon as a condition is satisfied. This condition is defined by selecting a type of safe tip mode and depending on the condition type, by setting a threshold value in 'Safe tip mode': unlocked, threshold, unlocked and threshold, and unlocked or threshold. In the unlocked case, the scanner retracts when the PLL module specified in 'PLL reference' unlocks. In the threshold case, the scanner retracts to the lowest position as soon as the oscillation amplitude of the PLL module reaches a value inferior/superior or equal – conditions '$\leq$' or '$\geq$' set by the user – to the value set in 'Threshold'. In the unlocked and threshold, and unlocked or threshold cases, the cantilever is retracted, respectively, if both conditions are simultaneously satisfied and if one of both conditions is satisfied. In the right part of the UI, the displacement of the scanner during the regulation is indicated by the position of the red tip, in the vertical slide; its value and the corresponding voltage applied to the scanner are displayed in 'Z (m)' and 'Z (V)'. Additionally, the user can retract the cantilever to a defined home position – value indicated by the blue tip on the vertical slide – by pressing on 'Home' or to the lowest position (maximum retraction) by pressing on 'Withdraw'.

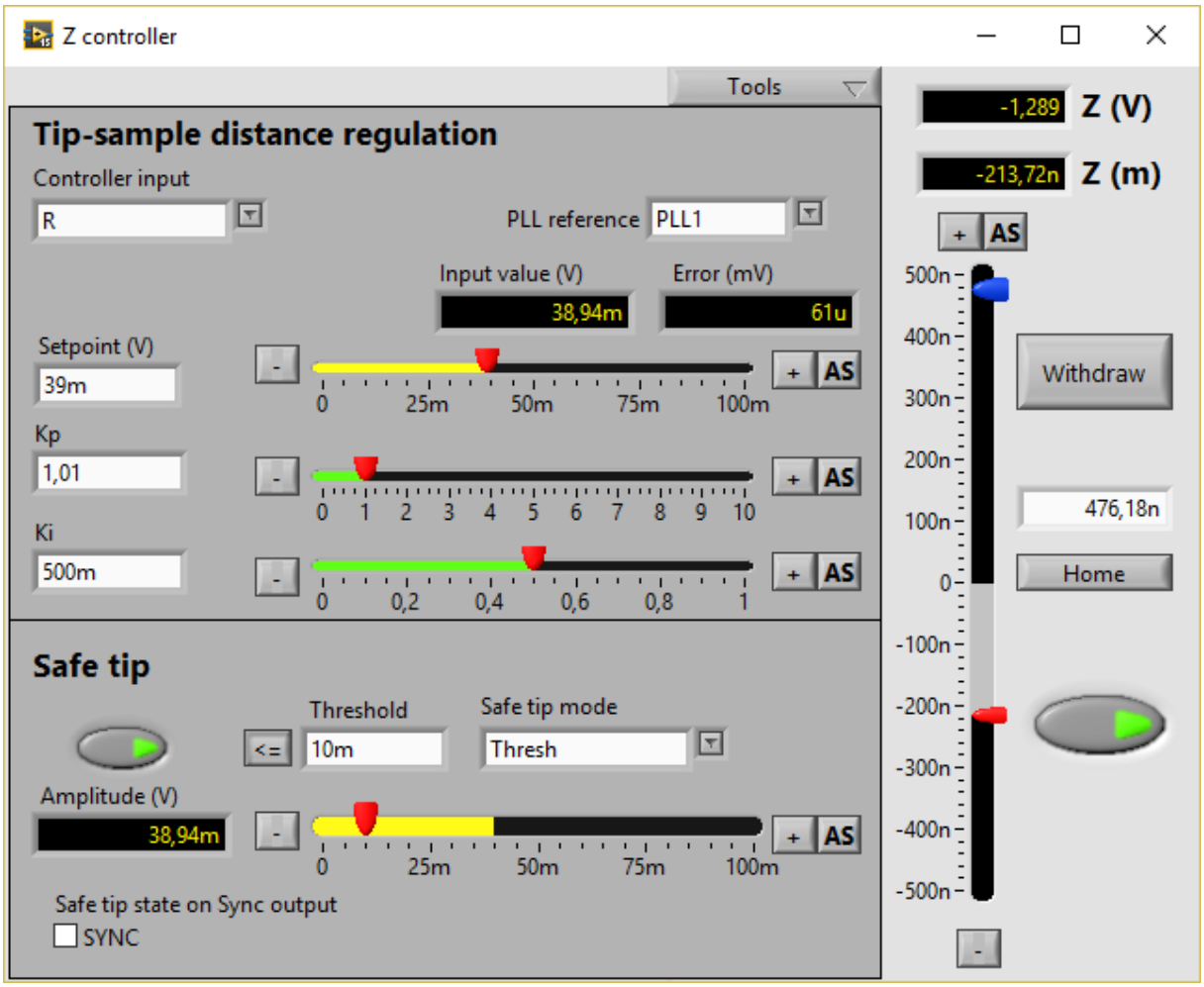

Figure 43: UI of the Z controller for the regulation of the tip-sample surface distance. The regulation parameter is set in 'Controller input' and can be the cantilever frequency shift, oscillation amplitude (of a selected PLL module) or its vertical deflection. The setpoint, proportional and integral gains are, respectively, set in 'Setpoint', 'Kp' and 'Ki'. To avoid tip crashes, a safe tip condition such as unlocked, threshold, unlocked and threshold, and unlocked or threshold can be used. If the condition is satisfied, the cantilever is retracted to the lowest position. The threshold condition for retracting can be a cantilever oscillation amplitude superior or inferior to the value specified in 'Threshold' and the unlocked condition, the unlocking of the selected PLL. Moreover, the cantilever can be retracted to a defined home position – value indicated by the blue tip on the vertical slide –, by pressing on 'Home' or at the maximum retraction position by pressing on 'Withdraw'. The scanner displacement is indicated in the right part of the UI by a red tip on the vertical slide; its value and the corresponding voltage applied to the scanner are displayed in 'Z (m)' and 'Z (V)'.

X,Y direction scanner

As illustrated in figure 45, the scan UI, enables the mapping of topography and of quantities, such as cantilever oscillation amplitude or phase shift to be mapped by moving the cantilever tip in the X and Y directions. For this purpose, the user defines a scan window corresponding to an area of the sample to investigate. The maximum size of the scan is defined by the voltage that the controller can deliver, i.e. −10 to 10 V in both directions. The scanning window is defined by setting its dimensions – in 'Width (m)' and 'Height (m)' – and a center position – in 'X0 (m)' and 'Y0 (m)' – in the maximum scanning window, as illustrated in figure 44. The window can

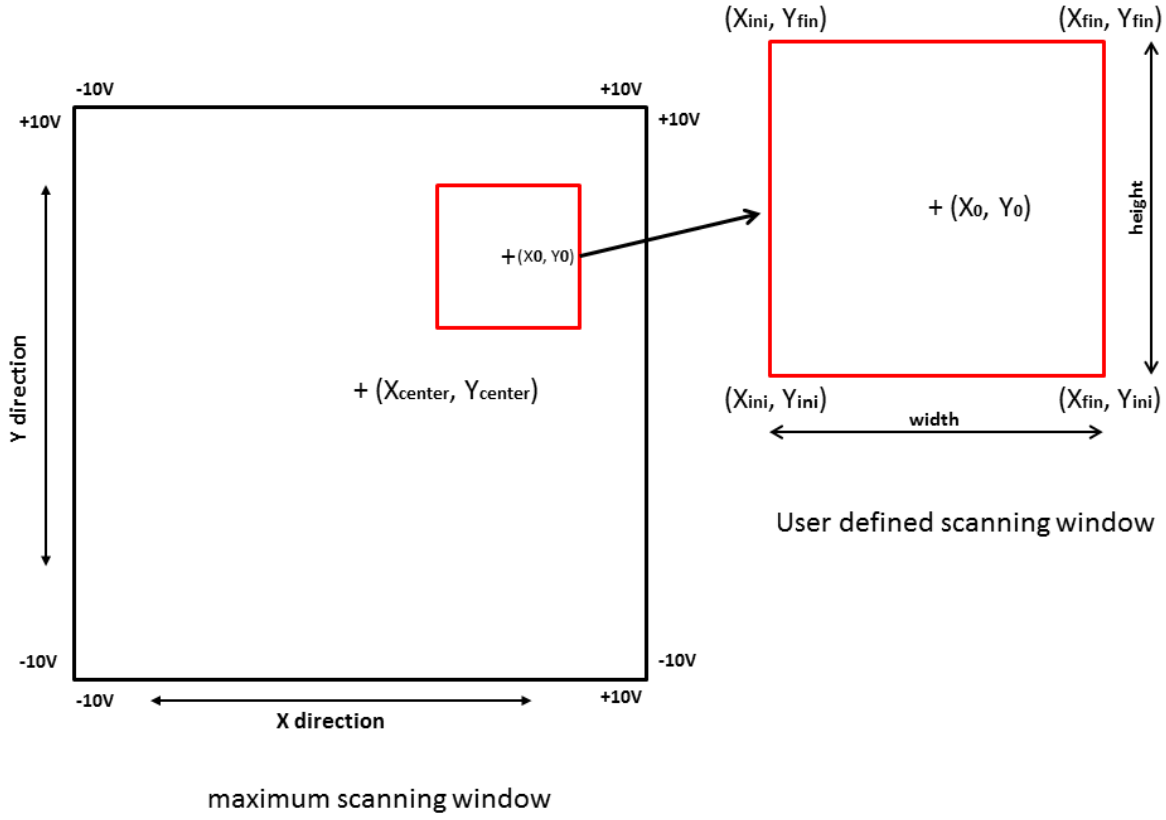

Figure 44: Definition of a scan window in the X and Y directions.

also be rotated by a defined angle specified in 'Angle (deg)'. The rotation is especially useful for correcting the sample tilt. The speed in the X and Y directions and the resolution in pixels and number of lines can also be defined. The tilt of the sample can be corrected in the X and Y directions by setting values in 'X axis (deg)' and 'Y axis (deg)'. The lines, consisting in recording a number of pixels – set in 'Pixels' – by sweeping forward and backward, are acquired at a speed in meters per second specified in 'Linear (m/s)'. The delay time in seconds between the acquisiton of two subsequent lines is set in 'Delay/line (s)'. The scans can be performed from the bottom-up position (Xini,Yini) or top-down position (Xini,Yfin) in figure 44 and continuously by selecting 'Loop acquisition'. A freeze function enables the scanning to be interrupted. Two saving options are possible, i.e. save the next image and save all images. The images are

saved by selecting ‘Save’ and ‘Next’ or ‘All’. In the ‘Data’ part of the UI, a measured channel – for example the measured phase shift as seen in figure 45 – is displayed by selecting it in ‘Channel’ and its acquired values processed with a function selected in ‘Processing’: Subtract average or Subtract slope. In the ‘Experiment’ window, quantities computed with the measured quantities – for example the elasticity computed with mathematical model of Herruzo et al. – are selected to be displayed instead of a measured channel. A palette of colors can also be set in ‘Colors palette’ to associate colors to a range of values for the measured quantities.

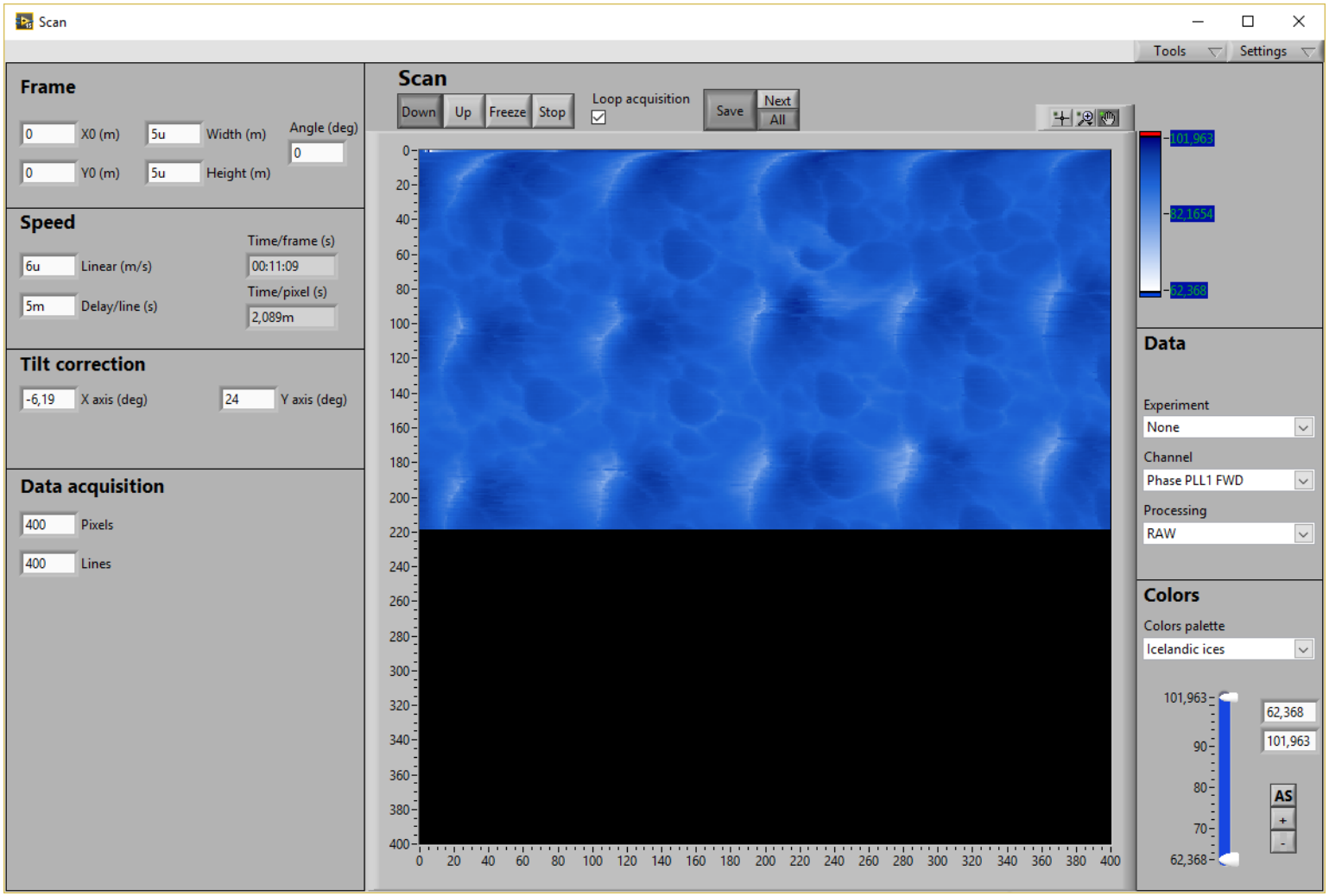

Figure 45: UI for scanning topography and measured quantities. The scanning window is defined by setting its dimensions – in 'Width (m)' and 'Height (m)' – and a center position – in 'X0 (m)' and 'Y0 (m)' – in the maximum scanning window, as illustrated in 44. The window can also be rotated by a defined angle specified in 'Angle (deg)'. The tilt of the sample can be corrected in the X and Y direction by setting values in 'X axis (deg)' and 'Y axis (deg)'. The lines, consisting in recording a number of pixels – set in 'Pixels' – by sweeping forward and backward, are acquired at a speed in meters per second specified in 'Linear (m/s)'. The delay time, in seconds between the acquisiton of two subsequent lines, is set in 'Delay/line (s)'. The scans can be performed from bottom-up – position (Xini,Yini) – or from top-down – position (Xini,Yfin) in figure 44 – and continuously by selecting 'Loop acquisition'. A freeze function enables the scanning to be interrupted. Two saving options are possible: save the next image and save all images. The images are saved by selecting 'Save' and 'Next' or 'All'. In the 'Data' part of the UI, a measured channel is displayed by selecting it in 'Channel' and its acquired values processed with a function selected in 'Processing'. In the 'Experiment' window, quantities computed with the measured quantities are selected to be displayed instead of a measured channel. A palette of colors can also be set in 'Colors palette' to associate colors to a range of values for the measured quantities.

5.4 Experiments

5.4.1 Frequency sweep

Frequency sweeps are useful to determine the resonance frequencies of cantilevers from resonance curves. A UI was developped for SAPHYR for this purpose (figure 46): the software uses a PLL module in lockin mode to excite the cantilever in a domain of frequencies specified by the user and records the oscillation amplitude and phase shift associated with the cantilever's response signal (section 3.2.2). Cantilevers are excited with a defined amplitude and a phase at origin set in 'Amplitude (mV)' and 'Phase at origin (deg)', respectively, in a frequency range specified by 'Start frequency (Hz)' and 'Stop frequency (Hz)'. A frequency range centered at center frequency 'fref (Hz)' set in 'PLL' UI with a length twice the value specified by 'Frequency range (Hz)' can also be defined. The sweeps can be performed from the start frequency to the stop frequency or conversely with '$>$' or '$<$', respectively. A number of amplitude and phase points, specified by 'Number of points', are sequentially recorded at a speed specified by 'Period (ms)'. The resonance frequency is determined from the fitting of the amplitude curve with a Lorentzian curve of expression $\frac{A}{4\pi^2\sqrt{(f^2-f_0^2)^2+(\beta f/\pi)^2}}$, where parameters A, f, f_0 and β, correspond to the amplitude, the frequency, the resonance frequency and the damping, respectively. The algorithm used for determining the parameters is based on Levenberg and Marquardt's method. The Q factor is determined from β by computing the ratio $\frac{f}{f_{sup}-f_{inf}}$, where f_{sup} and f_{inf}, correspond to the higher and lower frequencies of the fitting curve for which the intensity is half the intensity at resonance frequency f_0, respectively.

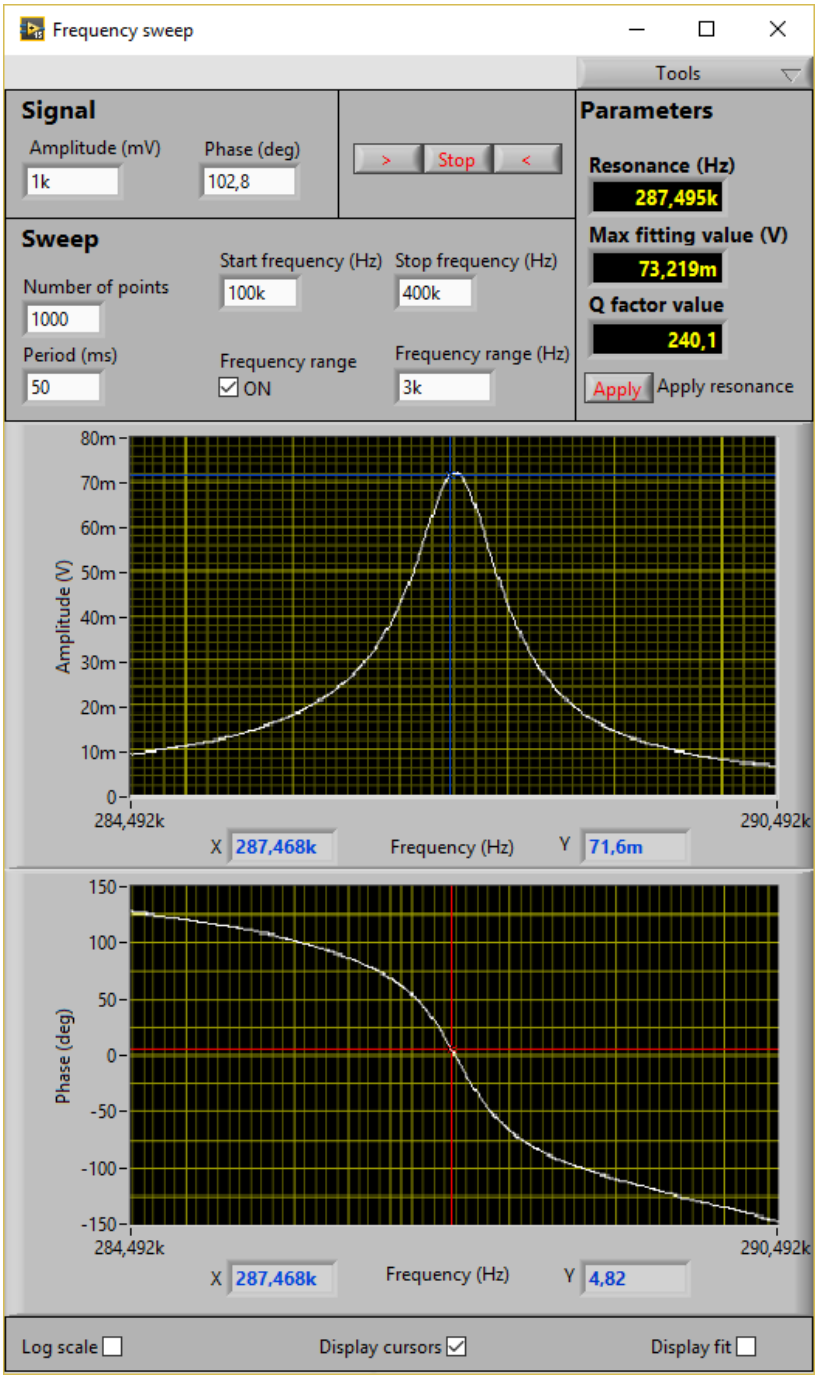

Figure 46: UI for performing frequency-sweep experiments. Cantilever resonances are detected by exciting it with a defined amplitude set in 'Amplitude (mV)' in a frequency range specified by 'Start frequency (Hz)' and 'Stop frequency (Hz)'. A frequency range centered at 'fref (Hz)' value, set in 'PLL' UI and with a length double the value specified in 'Frequency range (Hz)' can also be defined. A number of points specified by 'Number of points' are sequentially recorded at a speed specified by 'Period (ms)'. The resonance frequency is determined by fitting the amplitude curve. The value for the resonance can be defined as new value for 'fref (Hz)' value in 'PLL' UI by pressing the 'Apply resonance' button. Values in amplitude and phase graphs can be checked by moving cursors.

5.4.2 Z spectroscopy curve measurement

Z spectroscopy curve measurements are generally necessary to determine the sensitivity of the cantilever by measuring its vertical deflection as a function of the displacement, to determine sample elasticity by measuring load-displacement curves, as in Oliver and Pharr's method (see section 6.1), or to determine the load necessary to reach the elastic regime by simultaneously measuring frequency shift/load-displacement curves, as we will see in section 6.2. The curves are recorded by sweeping a number of positions from a lower to an upper limit with the Z scanner and a certain speed depending on the waiting time between the acquisition of two points, and recording one or several channels – vertical deflection for instance – corresponding to a position. For this purpose, a UI was developped for SAPHYR software, as illustrated in figure 47. The window is divided in three parts: two called Settings and Curves and the graph. In the Settings, the characteristics of the curves are defined before they are recorded. These characteristics are the number of points, the upper and lower limits of the position sweep, the waiting time between two acquisitions and the delay. This last parameter was specially developed for the investigation of elasticity with Oliver and Pharr's method, as we will see in section 6.1; it actually specifies the time delay in seconds, that elapses before the software starts to record the backward curve. The software can also simultaneously record several channels, such as the vertical deflection or the frequency shift. The user can specify whether he wants to save the curve or record a backward curve. Additionally to these functions, when recording the vertical deflection channel, he can specify the type of the curve: sensitivity or load displacement. In the first type, the curves are recorded to determine the sensitivity of the cantilever by acquiring the voltage of the photodiode. In the case of the load-displacement curve, this voltage is multiplied by the calibration factor, i.e. in the product of the cantilever spring constant by the inverse of the sensitivity, with their values taken from the 'Cantilever characteristics' UI. In the Curves part, a curve is selected among the selected channels and displayed in the graph. The forward and backward curves can also be shifted in the abscissa and ordinate directions. In the graph, two cursors (red) can be used to determine the slope of the linear sections in the curves. The slope is determined by fitting the curve portion between the two cursors and is displayed in the upper right corner. The graph can also be used to determine the elasticity of samples with Oliver and Pharr's method; for this purpose, the UI elasticity investigation (figure 48) must be additionally used by selecting it in the 'tools' menu. For this purpose, the user just needs to determine the slope of the curve in the linear deformation phase with the red cursors and the value for P_{max} and h_{max} with the yellow cursors. By pressing on the 'add measurement to table button', the values and parameters in equations 1.2 and 1.4-1.8 are automatically computed from P_{max}, h_{max}, the slope of the linear curve portion and the entered Poisson's ratio of the sample.

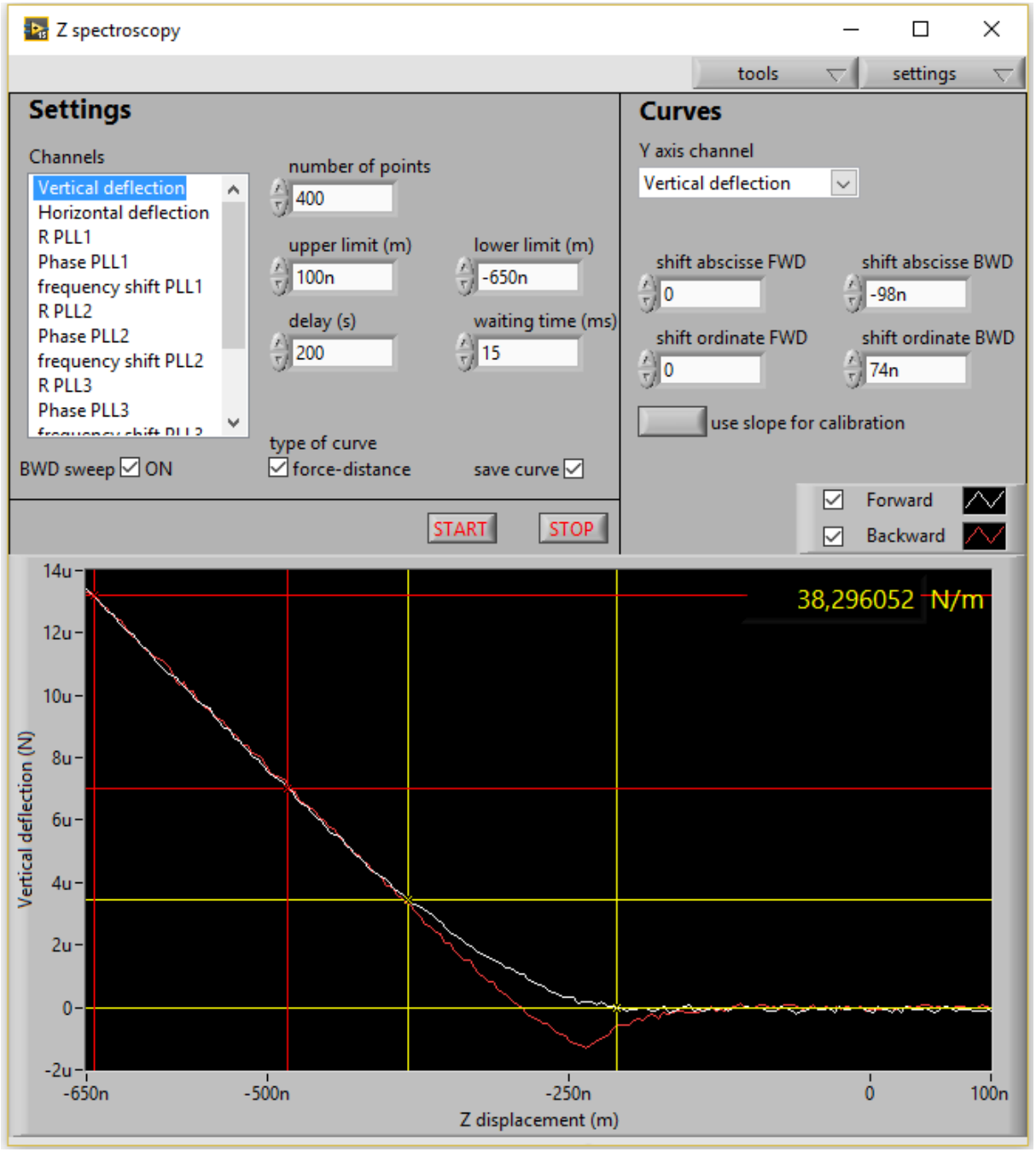

Figure 47: UI for Z spectroscopy curve measurements. The measurement of the curves consists in sweeping a number of positions at a certain speed from the lower to the upper limit with the Z scanner and recording the value of the selected channels – vertical deflection, frequency shift – associated with a given position. The measurement speed is defined by the waiting time. A time delay can also be imposed before the software begins to record the backward curve. The parameters are entered in the Settings part. Forward and backward curves can be shifted. Elasticity measurements with Oliver and Pharr's method can be performed by using the UI with elasticity investigation UI. Values and parameters in equations 1.2 and 1.4-1.8 are computed by positioning the red and yellow cursors for determining the slope of the linear curve portion, and parameters P_{max} and h_{max}, respectively. Computed values are displayed in elasticity investigation UI.

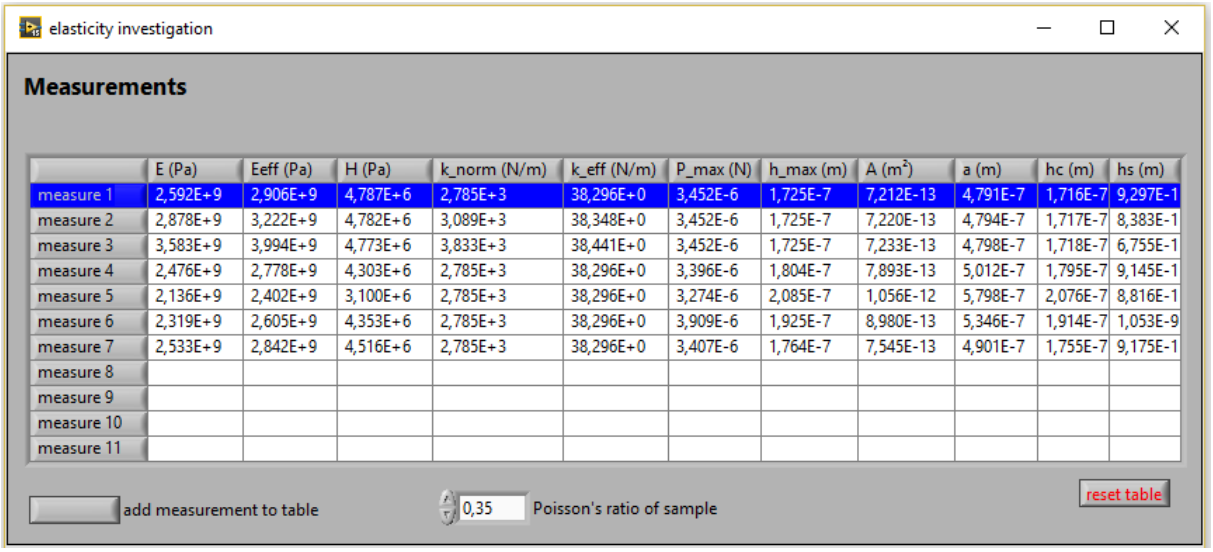

Figure 48: UI for performing elasticity measurements with Oliver and Pharr's method. By pressing on the 'add measurement to table button', the values and parameters, in equations 1.2 and 1.4-1.8, are automatically computed from the position of the cursors in the graph in 'Z spectroscopy' UI and from entered Poisson's ratio of the sample.

Chapter 6

Measurements

In this chapter, we present the results of the AFM elasticity investigation on LLDPE, PP, PS and PTFE polymer samples and a self-assembled monolayer of 1H,1H,2H,2H-perfluorodecyltrichlorosilane (FDTS) on a silicon oxide substrate perforated with circular holes prepared by polymer blend lithography [35]. For this purpose, a static method based on the work of Oliver and Pharr [25, 30] for rigid indenters – presented in subsection 1.3.1 – and a dynamic method based on the publication of Herruzo et al. [11] were used. The static method consisted in measuring load-displacement curves to determine the parameters necessary for the computation of the elastic modulus in Oliver and Pharr's mathematical model. As cantilevers are different from rigid indenters, we analyzed parameters such as creep of the piezoelectric scanner, cold flow, thermal expansion of the sample and finite stiffness of the cantilever to be able to apply the theoretical model of Oliver and Pharr to the curves measured by AFM. The method was tested on PTFE and PS. We explain the existence of a plastic deformation phase followed by an elastic one. In the dynamic method, we show, by recording Δf_1, Δf_2 and F_N as a function of the Z scanner displacement curves on LLDPE, PP, PS and FDTS, that a linear relation similar to that in the work of Herruzo et al. [11], exists between the frequency shift of the first flexural mode of the cantilever Δf_1 and the square of the frequency shift of the second flexural mode Δf_2^2 when measuring in contact mode with a certain load F_N. This way of measuring avoids the problem of instabilities of the FM AFM-based method when measuring in nondry air at ambiant temperature. We assessed the necessary load F_N to measure in the elastic deformation phase. We used this relation to determine the storage modulus of LLDPE, PP, PS and FDTS and give an order of magnitude of Young's modulus of FDTS thin film.

6.1 Investigation of polymer sample elasticity by static-mode AFM

6.1.1 Experimental

Microscope and data acquisition

The measurements were performed with a high-speed AFM head (figure 49) developped at Ecole Polytechnique Fédérale de Lausanne by Prof. Georg Fantner's group. The load-displacement curves were recorded with SAPHYR controller and the Z spectroscopy UI in subsection 5.4.2.

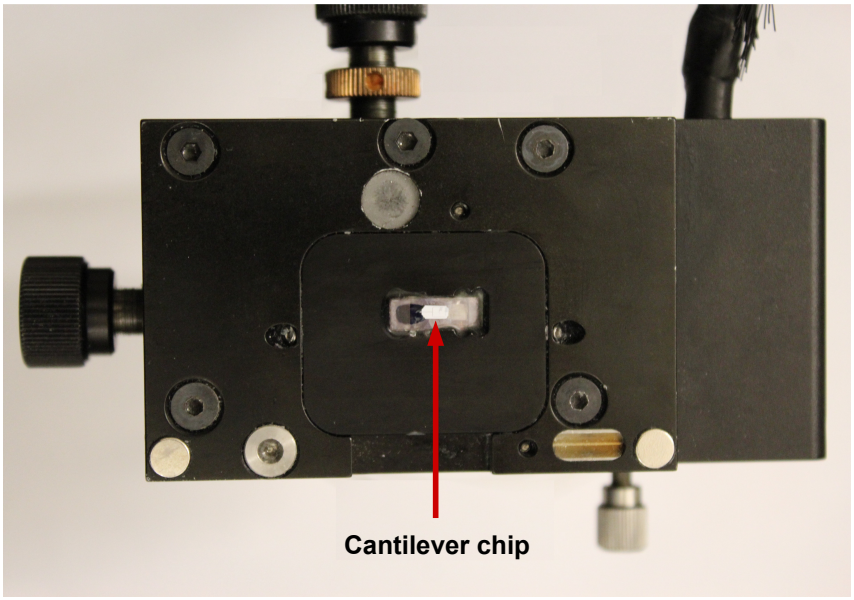

Figure 49: High-speed AFM head used for the measurements. The cantilever chip is fixed on the microscope head with a special wax.

Cantilevers

The measurements were performed with a PPP-NCL cantilever from Nanosensors™ (Si tip of Young's modulus $E_{tip} \sim$ 169 GPa) to have the necessary stiffness to reach the elastic regime. The cantilever is characterized by a resonance $f_{0,1} =$ 172.611 kHz and a stiffness constant $k_1 =$ 38.83 N m^{-1} for the first flexural mode in free space. The stiffness constant was computed from the theoretical formula $k_1 = \frac{Ewt^3}{4l^3}$ [2], where E, t, w and l are, respectively, Young's modulus of the cantilever beam, thickness, width and length. The thickness $t =$ 6.55 μm was determined from $f_{0,1}$ and the formula $t \sim$ 6.1911 $(\frac{\rho}{E})^{\frac{1}{2}} f_{0,1} l^2$ [2]. The cantilever width $w =$ 39 μm and length $l =$ 228.5 μm were determined by optical microscopy. The values $E =$ 169 GPa and $\rho =$ 2,330 kg m^{-3} were taken for Young's modulus of the silicon beam and its mass density. The measured normal force $F_{N,meas}$ that corresponds to the vertical deflection of the cantilever and gives the value of the applied normal force F_N on the sample surface was calibrated with a factor obtained by dividing the cantilever's spring constant by its optical sensitivity S_z. The optical sensitivities of value 1.78 μm V^{-1} for measurements on PTFE and 1.75 μm V^{-1} for measurements on PS were determined by measuring a vertical deflection-distance curve on

an n-type silicon(111) sample of electrical resistivity $=10\ \Omega$ m and by taking the inverse of the slope.

Determination of the sensitivity of the cantilever

The sensitivity of the cantilever describes its deflection as a function of the displacement of the Z scanner. This characteristic actually depends on different factors, such as the reflective coating on the cantilever back, but also on the temperature, as illustrated in figure 50, where we can observe a decrease in sensitivity and an increase in thermal noise as the temperature increases. The sensitivity of a cantilever is generally determined from a load-displacement curve performed on a hard sample, for instance silicon(111), as it was the case for the present measurements; the elastic deformation of the cantilever can thus be neglected and the movement of the Z scanner equals the deflection of the cantilever. As temperature and laser intensity may vary, the sensitivity was checked before and after recording the load-displacement curve.

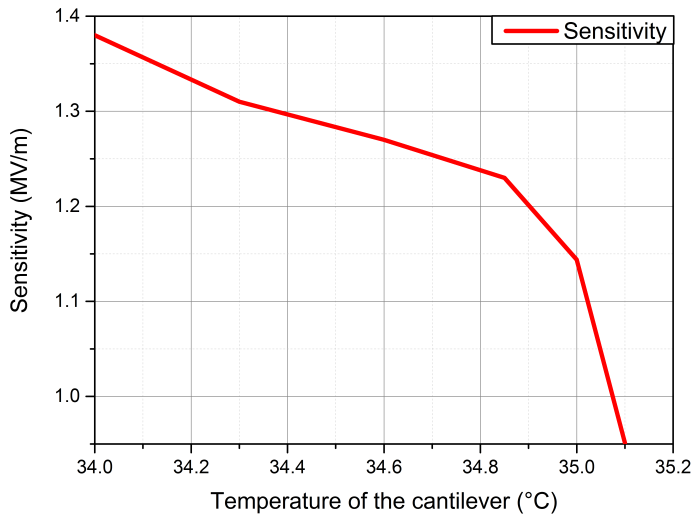

Figure 50: Effect of temperature on sensitivity. The curve was obtained by putting the microscope head in a box and cooling down the vicinity with nitrogen N_2. A load-displacement curve was then periodically measured on a silicon(111) sample to determine the sensitivity and observe its changes.

Samples and measurement conditions

The elasticity of polytetrafluoroethylene (PTFE) and polystyrene (PS) was investigated in nondry air with a relative humidity of 36 $\%$ and an ambient temperature of 27 °C.

6.1.2 Measurement and results

Recording of load/unload-displacement curves

The load/unload-displacement curves of PTFE and PS were recorded by indenting with a displacement magnitude large enough to observe two phases: a plastic deformation phase characterized by a nonlinear relation between the load and the displacement, followed by an elastic deformation phase characterized by the linearity of the relation between the load and the displacement, as illustrated in figure 54. In the elastic phase, the first recorded load/unload-displacement curves, measured by retracting the tip directly after it reached the maximum depth, were all characterized by a slope for the load-displacement curve different from the slope of the unload-displacement curve. By setting a time delay long enough at the maximum displacement of the Z scanner, before retracting the tip, and during which the tip keeps its position, one can observe, that the slope of the unload-displacement curve tends to the slope value of the load-displacement curve, as illustrated in figure 52. A shift ΔL between the maximum load of both curves, dependent on the time delay, can also be observed. The analysis of ΔL as a function of the time delay showed that ΔL tends to reach a constant value after several minutes, as illustrated in figure 53. The shift ΔL and the different slopes can be explained by different factors, such as cold flow, thermal expansion and piezo creep:

– **cold flow or sample creep** is the tendency of the sample to continue to deform even after stopping the indentation;

– **thermal expansion** also is a continuous deformation of the sample in the vicinity of the tip due to an increase in temperature. This increase is due to the energy generated by the friction of the tip with the surrounding matter, and

– **piezo creep or drift** is a characteristic of a piezoelectric material. This effect describes the tendency of the Z scanner piezoelectric material to continue to expand even if the applied voltage stays constant for a while. This effect can easily be observed by putting the tip into contact with the sample surface at a defined position and monitoring the vertical deflection signal. One can observe an increase in the vertical deflection signal, as shown in figure 51, which illustrates the recording of a load-displacement curve. When the curve is recorded, the applied voltage stays constant and the drift appears. The drift can be described as a function defined by

$$L(t) = L_0 \left(1 + \gamma log_{10}\left(\frac{t}{0.1}\right)\right), \tag{6.1}$$

where γ is the creep factor that determines the rate of the logarithm, with $0.01 \leq \gamma \leq 0.02$. L_0 is the nominal constant displacement after 0.1 s. The piezo creep can be neglected if the position of the Z scanner is controlled in a closed servo loop, which is not the case with the measurements in the present work. However, the measurements performed in the present work were done in open loop. The correct time delay between the measurement of the loading and unloading curves can be estimated by measuring the load difference ΔL between the last recorded point of the loading curve and the first point of the unloading curve, as illustrated in figure 52. This difference is actually dependent on the delay and becomes constant after a certain time, as illustrated in figure 53. By correcting the shift ΔL and matching the linear part of both load-displacement curves, as illustrated in figure 54, we can see that the curves can be

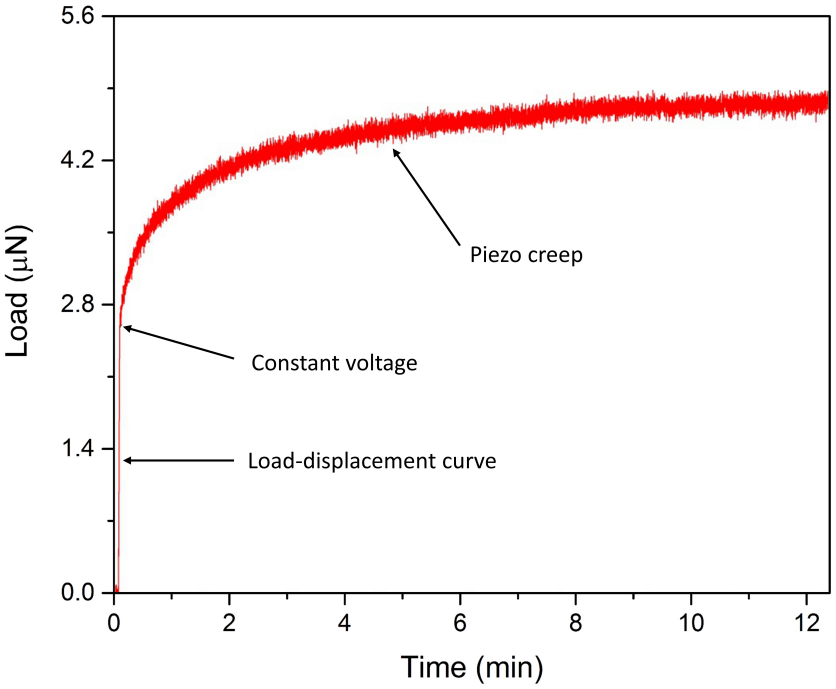

Figure 51: Piezo creep observed after recording a load-displacement curve. The voltage applied on the piezo scanner stays constant. On the four-quadrant detector, we observe that the piezo scanner continues to expand with time. This evolution follows a logarithmic law.

split into two areas: the out-of-contact and jump-to-contact area and the indentation area. In the out-of-contact and jump-to-contact areas, the tip is approached onto the sample surface. When the tip is close enough, long distance interaction forces, generated by the atoms and molecules of the surface, attract the tip onto the surface, which bends the cantilever – negative values of the load. This effect cannot be observed in the loading curve due to the resistance of the high spring constant of the cantilever. When the tip comes into contact with the surface due to the displacement of the Z scanner, the indentation area begins – positive values of the load. This area is characterized by a plastic deformation phase followed by an elastic deformation phase.

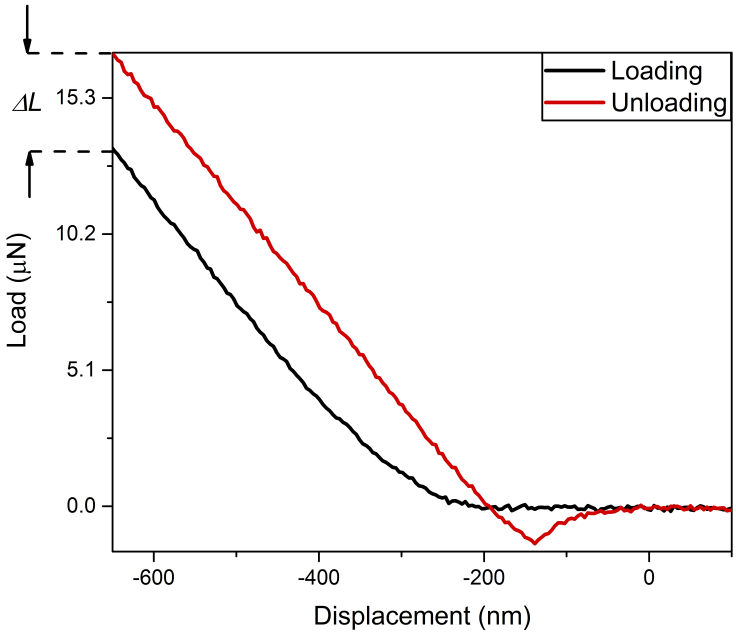

Figure 52: Load-displacement curve obtained with a delay of 3 min. Due to the delay, a load difference, ΔL, between unloading and loading curves can be observed.

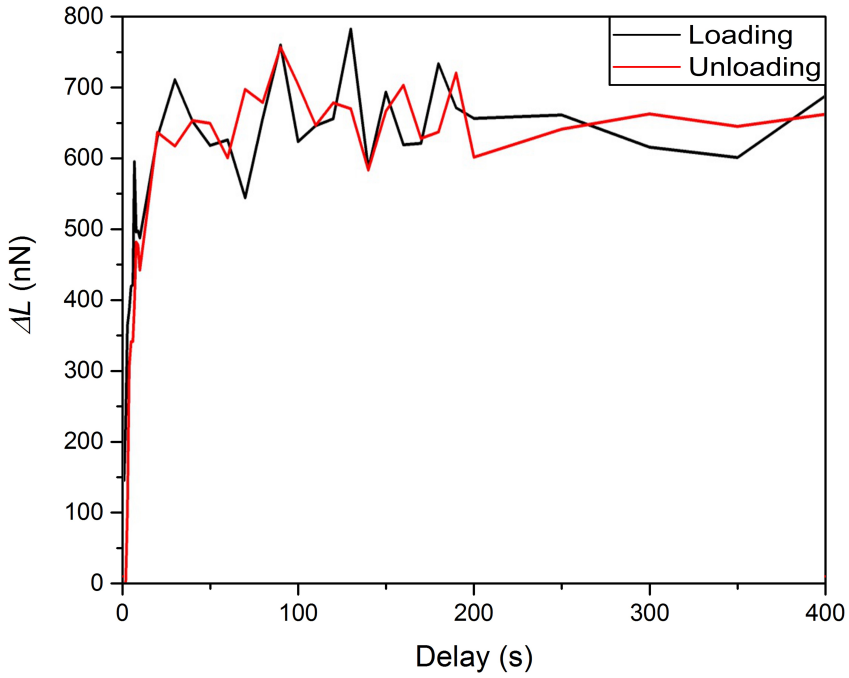

Figure 53: Recording of the ΔL (Delay) curve to estimate the time delay before recording an unloading curve.

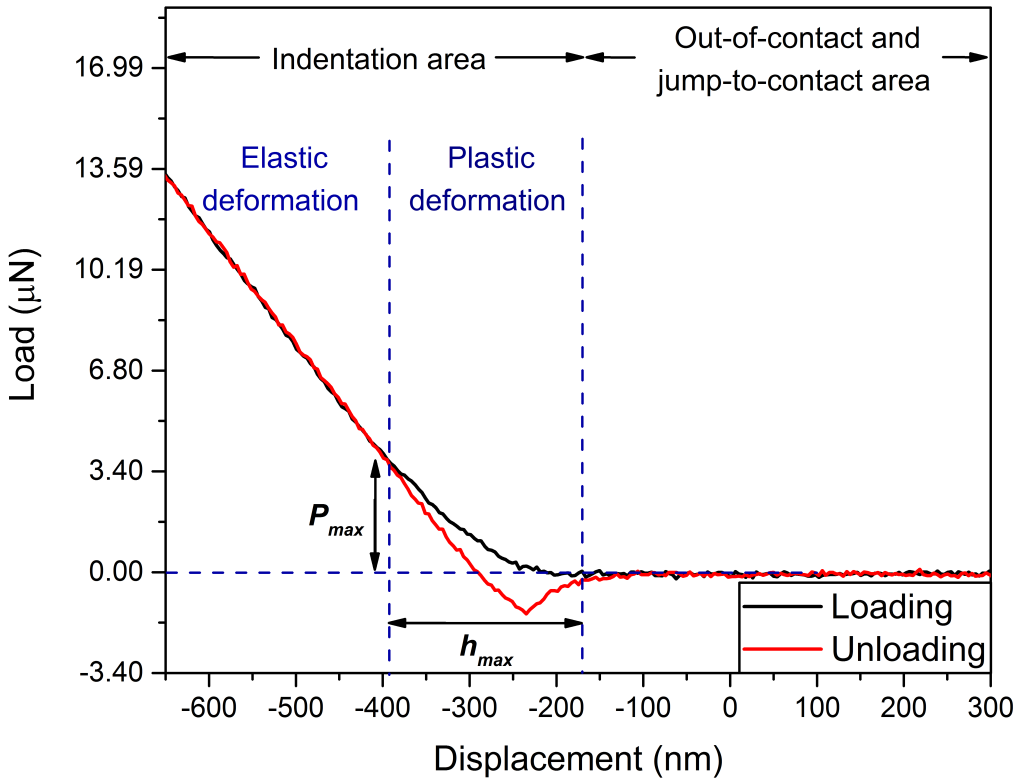

Figure 54: Load-displacement curves obtained by cantilever tip indentation and retraction on PS. The cantilever is a PPP-NCL of spring constant 38.83 N m^{-1}. The curves can be split into two areas: the out-of-contact and jump-to-contact area and the indentation area. In the first area, the tip is approached onto the sample surface. When the tip is close enough to the surface, a bending of the cantilever characterized by negative values for the load is observed. This effect is not observed here due to the high spring constant of the cantilever that resists bending. The indentation area starts when the tip comes into contact with the surface due to displacement of the Z scanner. The area is characterized by a plastic deformation phase followed by an elastic deformation phase. h_{max} and P_{max} are determined from the length and the maximum load in the plastic deformation phase.

Sample surface deformations and evolution of stress during indentation

The existence of a plastic and an elastic deformation phase is explained by the evolution of stress σ (ratio of the applied normal force F_N to the cross-section A of the cantilever tip) during indentation of the sample surface by the cantilever tip, as illustrated in figure 55. At the beginning of the indentation, after setting the tip on the sample surface, stress is increased from a normal force with an initial value of 0 nN. The evolution of stress can be split into three phases. In the first phase, if the applied normal force increases gently or if the contact surface between the tip apex and the surface is large enough, the generated stress increases gently enough to deform the sample surface elastically. This elastic phase does not occur if the steps of the Z scanner responsible for the increase in the applied normal force are too large. In this case, the generated stress is strong enough to deform the surface plastically and phase 2 is initiated. In the second phase, due to the geometry of the tip, assumed to be pyramidal, the contact area is small enough and the applied normal force strong enough to create a stress that deforms the sample surface plastically. In the third phase, the tip geometry and the increase in the indentation depth result in a larger increase in the contact area than that produced by the applied normal force, thus decreasing the stress on the sample surface. When the stress decreases below a threshold value σ_0, the sample starts deforming elastically.

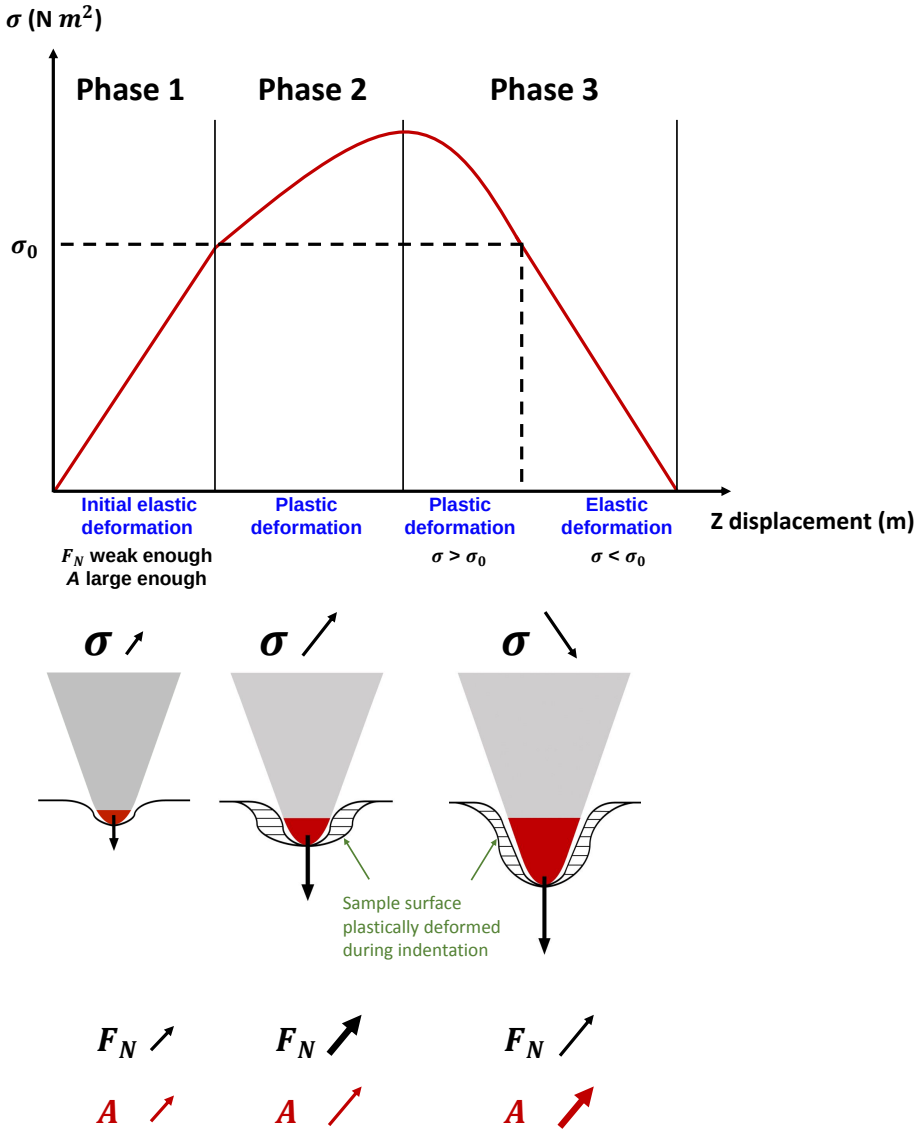

Figure 55: Three phases characterizing the evolution of stress σ during indentation by the cantilever tip. This evolution is responsible for the plastic and elastic deformation of the sample. In phase 1, in the presence of a weak enough applied normal force F_N or a large enough cross-section A, the generated stress is small enough to deform the surface elastically. This initial elastic phase can only be observed if the steps used for the Z scanner are small enough. If the step is too big, the evolution of the stress is directly initiated with phase 2. In phase 2, the large value of F_N and its fast increase compared to A generate a stress large enough to deform the surface plastically. In phase 3, the geometry of the tip results in a fast increase in the contact area and hence of A compared to the moderate increase in F_N, which decreases the stress. When the stress decreases below a threshold value σ_0, the deformation becomes elastic. The red area of the tip apex describes the contact area of the tip. The striped area shows the region of the sample plastically deformed during indentation. The arrow at the tip apex represents the applied normal force F_N; the arrows on the right of σ, F_N and A represent increased speed (bold for fast) and magnitude (length).

Computation of PTFE and PS elastic moduli

In Oliver and Pharr's method, h_{max} and P_{max} are defined, respectively, as the maximum depth during the indentation in the plastic deformation phase and its associated load. The sample stiffness $k_{sample,norm}$ is determined from the derivate at h_{max} of the fitting $-$ with the power law in equation 1.3 $-$ of the unloading curve, that characterizes the recovery of the elastic displacement. In our case, as the fit with the power law did not match the shape of the unload curve, $k_{sample,norm}$ at h_{max} was determined from the fitting of the slope of the loading curve (or of the unloading curve as the slope is the same) in the elastic deformation phase. h_{max} and P_{max} were defined as the length and the maximum load in the plastic deformation phase, as illustrated in figure 54. The analyzed load-displacement curves for PTFE and PS with defined h_{max} and P_{max} and the linear fit of the elastic deformation phase are shown in figures 56 and 57. As we can see, the sample normal stiffness $k_{sample,norm}$ was determined from the slope by modelizing the cantilever tip in contact with the sample surface by two springs in a series, k_1 and $k_{sample,norm}$ which are, respectively, the spring constant of the cantilever and the normal sample stiffness (of constant value in the elastic phase), as illustrated in figure 58a. As shown in figure 58b, the applied load F_N, due to the displacement of the Z scanner Δz, is $F_N = k_{eff}\Delta z$, where k_{eff} is the effective spring of value $k_1 k_{sample,norm}/(k_1 + k_{sample,norm})$ which corresponds to the slope of the load/unload curves in the elastic deformation phase. Hence, $k_{sample,norm}$ can be determined by the formula $k_{sample,norm} = k_1 k_{eff}/(k_1 - k_{eff})$. The determination of k_{eff} and computations of $k_{sample,norm}$ for PTFE and PS are shown in table 1. For PTFE, for a determined k_{eff} of 35.46 N m^{-1}, the computation of $k_{sample,norm}$ yields a value of 408 N m^{-1}. For PS, three different fittings of the slope yield values of 38.29, 38.34 and 38.44 N m^{-1} for k_{eff}. The associated computed $k_{sample,norm}$ yield the values 2,785, 3,089 and 3,833 N m^{-1}. The small variation of approximately 0.4% between the first and the third slope yield a variation of 27% for their associated $k_{sample,norm}$. This large variation is explained by the fact that the denominator in the formula for $k_{sample,norm}$ computation is close to 0 due to values for k_{eff} close to the cantilever spring constant k_1. This effect shows that the method is highly dependent on the stiffness of the cantilevers when measuring on PS and that stiffer cantilevers should be prefered when using this method. The elastic moduli of PTFE and PS were computed from $k_{sample,norm}$ and parameters h_{max} and P_{max} and taking a Poisson's ratio of 0.46 for PTFE [36] and 0.35 for PS [37]. The results summarized in table 1 show values in good accordance with Young's moduli of bulk materials reported in the literature $E_{sample,lit}$ for PTFE and PS, as seen in table 2.

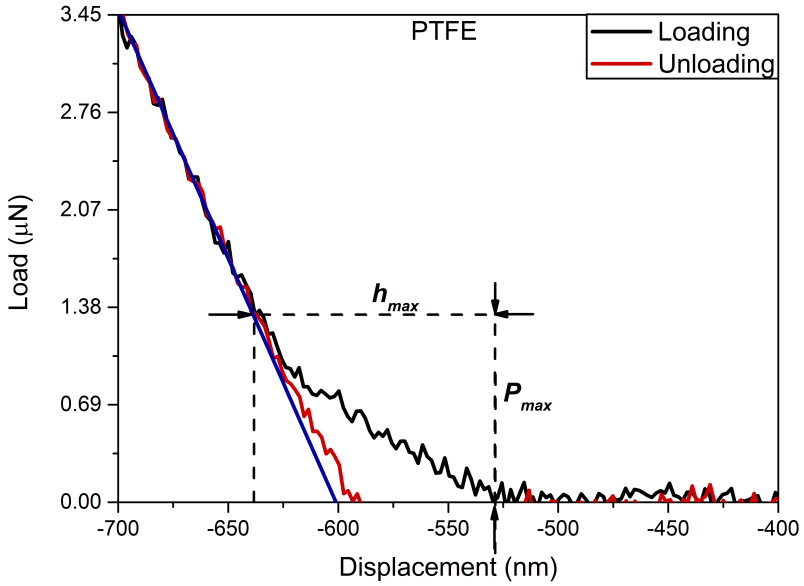

Figure 56: Definition of the plastic deformation phase by h_{max} and P_{max}, and linear fit of the elastic deformation phase on the load-displacement curve of PTFE.

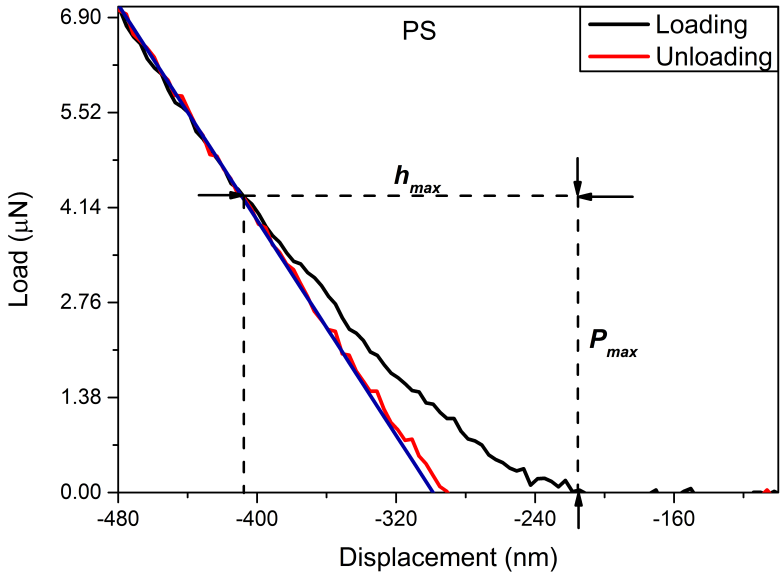

Figure 57: Definition of the plastic deformation phase by h_{max} and P_{max}, and linear fit of the elastic deformation phase on the load-displacement curve of PS.

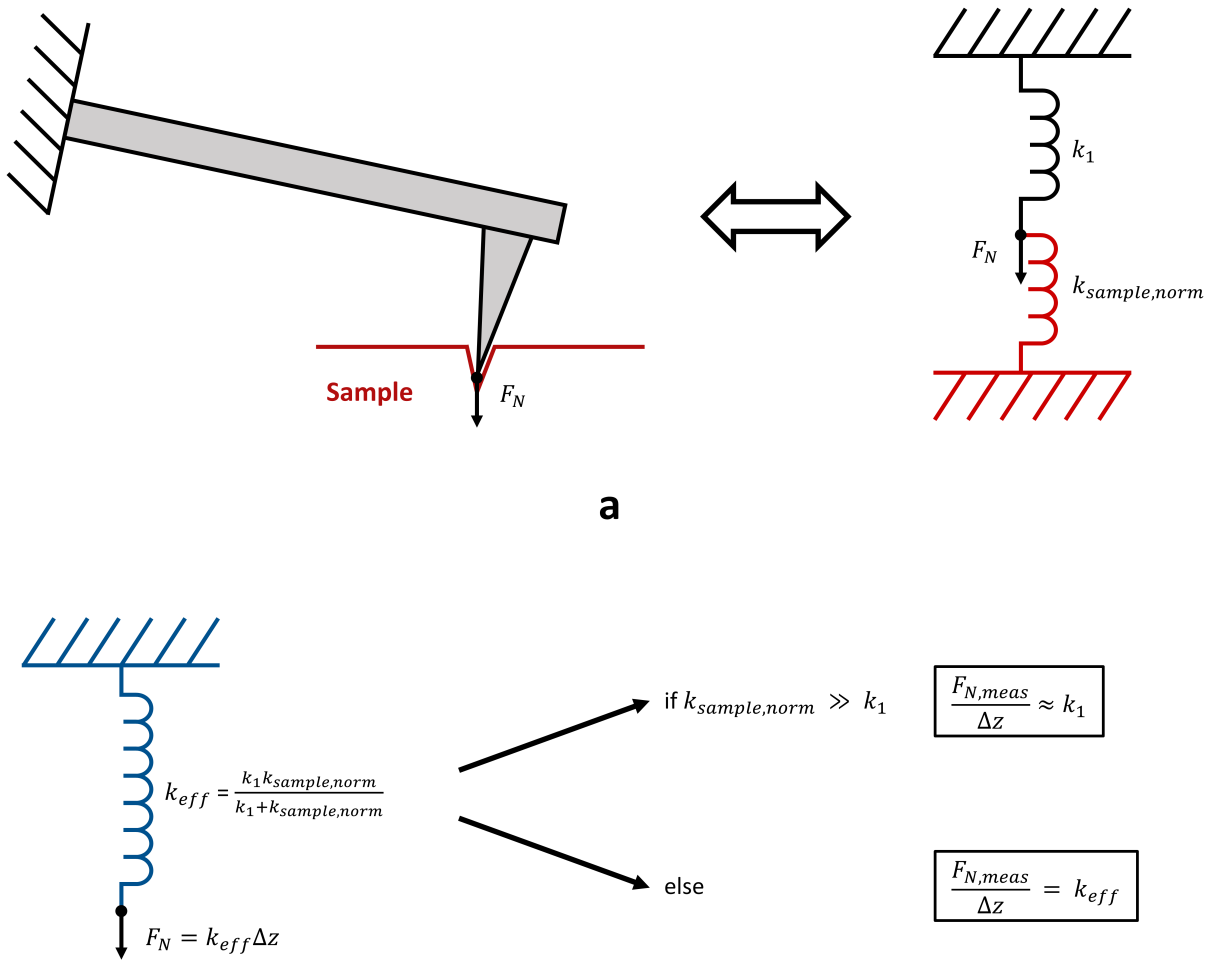

Figure 58: **a** Modelization of the cantilever in contact with sample surface by two springs in a series, k_1 and $k_{sample,norm}$, representing the cantilever spring constant and the normal sample stiffness, respectively. The arrow F_N represents the applied normal force. **b** Effective spring constant k_{eff} and value of the ratio of the measured applied normal force $F_{N,meas}$ to the displacement of the Z scanner Δz as a function of sample stiffness.

Measurement parameters	PTFE	PS
Indenter geometry ϵ	0.75	0.75
Poisson's ratio of sample ν_{sample}	0.46 [36]	0.35 [37]
Determined parameter		
Curve slope k_{eff} (N m^{-1})	35.46	38.29; 38.34; 38.44
P_{max} (μN)	1.34	4.24
h_{max} (nm)	118.3	193.2
$k_{sample,norm}$ (N m^{-1})	408	2785; 3089; 3833
Cantilever sensitivity (m V^{-1})	1.78	1.75
Force calibration (μN V^{-1})	69.11	67.95
Computed and quantities		
Young's modulus E_{sample} (GPa)	0.499	2.59; 2.88; 3.58
E_{eff} (GPa)	0.63	2.9; 3.22; 3.99

Table 1: Measurement parameters and determined parameters for the computation of Young's modulus of PTFE and PS $E_{sample,meas}$.

Sample	$\boldsymbol{E_{sample,meas.}}$ (GPa)	$\boldsymbol{E_{sample,lit.}}$ (GPa)
PTFE	0.499	0.3−0.8 [36]
PS	2.59; 2.88; 3.58	2.3−4.1 [37]

Table 2: Measured elastic modulus $E_{sample,meas}$ and values for Young's modulus of bulk materials from the literature $E_{sample,lit}$ on PTFE and PS. $E_{sample,meas}$ values are included in the range of Young's moduli for bulk materials.

6.2 Investigation of the elasticity of polymer samples by dynamic-mode AFM

6.2.1 Measurement method

Principle of the method

The FM-AFM-based measurement method introduced by Herruzo et al. [11] for the measurement of the frequency shifts relative to the first and second flexural modes in equation 1.17 reaches its limits when the measurements are performed in nondry air, at ambiant temperature. These limitations are actually due to the instability of the PLLs used for the measurement of the frequency shifts and hence of the Z controller, which is explained by the presence of water on the sample surface. As a consequence of the presence of water, the repulsive regime necessary for the measurement of the frequency shifts can hardly, if at all, be reached, as illustrated in figure 59, where the frequency shift of the first flexural mode, Δf_1, was recorded as a function of the Z scanner displacement during approach (black) and retraction (red). We can actually observe jumps in the frequency shifts on both curves due to unlockings of the PLL used for the measurement of the frequency shift.

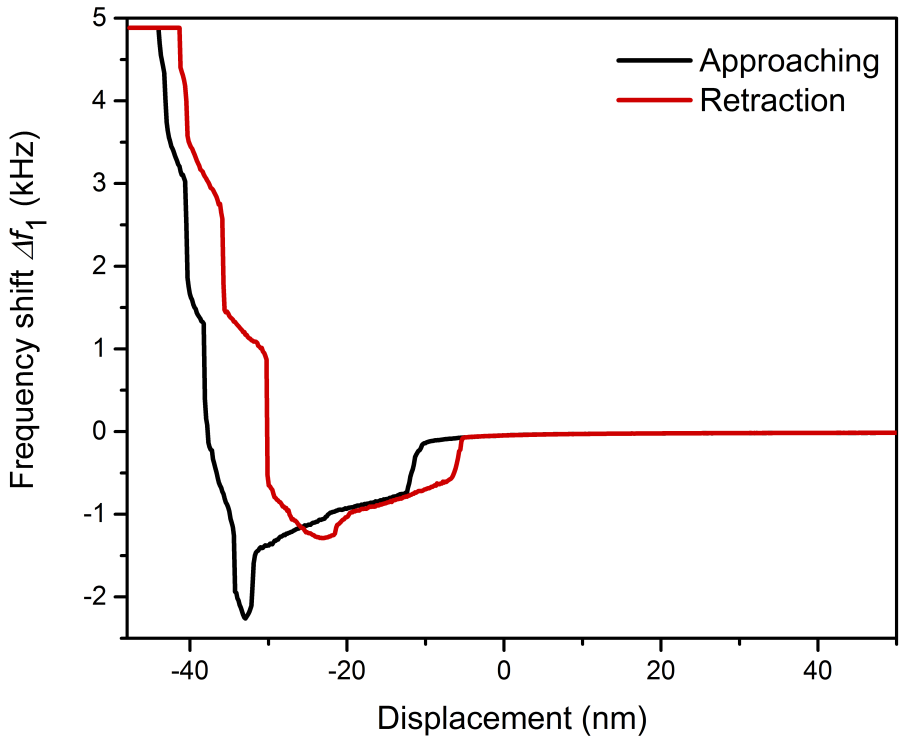

Figure 59: Frequency shift-displacement curves obtained in nondry air by recording the frequency shift of the first flexural mode of the cantilever, Δf_1, during approach (black) and retraction (red) of the tip. Jumps due to unlocking of the PLL can be observed and are explained by the presence of water on the sample surface. The curves were recorded with a PPP-NCL cantilever from Nanosensors^{TM} with a resonance frequency of 160 kHz and a spring constant of 48 N m^{-1}.

To overcome this problem, we propose a new method for measuring the frequency shifts of the first and second flexural modes in equation 1.17, based on the tracking of the first and second flexural contact resonances. In contrast to the FM-AFM method, where the applied normal force F_N on the sample is controlled by Δf_1, in our method, the applied normal force F_N is directly controlled by the vertical deflection of the cantilever. The stability of the microscope during its operation is insured by the use of an amplitude A_2 small enough compared to A_1. In this case, the relation between the effective elastic modulus of the sample E_{eff} and the frequency shifts Δf_1 and Δf_2 can be expressed as follows

$$E_{eff} = \alpha(A_1)\frac{\Delta f_2^2(F_N)}{\Delta f_1(F_N)}, \tag{6.2}$$

where α depends on amplitude A_1, determined from a sample of known elastic modulus, and Δf_1 and Δf_2 are the frequency shifts that depend on the applied normal force F_N and are determined from the measured contact resonances from the relation $\Delta f_i = f_i - f_{0,i}$, where Δf_i, is the frequency shift, $f_{0,i}$ is the resonance in free space and f_i is the contact resonance of the i^{th} flexural mode.

Feedback controls

As introduced by Herruzo et al. [11], five different feedback loops are used as feedback controls, as shown in figure 60: two feedbacks for maintaining amplitudes A_1 and A_2 constant, two for keeping phase shifts φ_1 and φ_2 constant for tracking contact resonances f_1 and f_2 and the last as main feedback for controlling the applied normal force F_N.

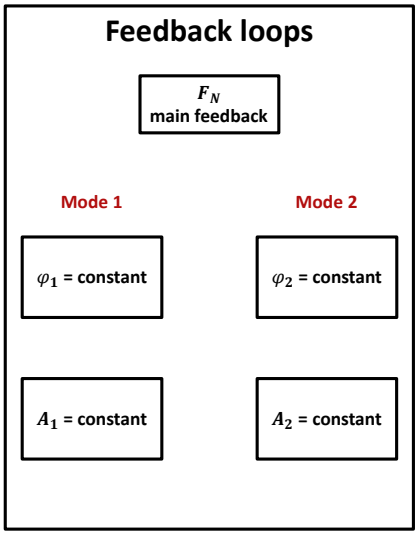

Figure 60: Feedback loops necessary to track the flexural contact resonances of the cantilever. The main feedback insures that the measurements are performed with a constant normal force. The other feedbacks are used to keep the phase and the amplitude φ_1, A_1 for first flexural mode and φ_2, A_2 for second flexural mode constant.

6.2.2 Experimental

Microscope and data acquisition

The measurements were performed with a flex AFM head from Nanosurf and the Nanonis scanning probe microscope controller. The system integrates PLLs necessary for tracking the contact resonances and all the controlling and signal generation modules for measuring and mapping the physical quantities. Square areas of 2.5 μm were acquired at 256 x 256 pixels and at a scan speed of 2 μ m s^{-1}.

Cantilevers

The measurements were performed with a PPP-CONT cantilever from Nanosensors™ (Si tip of Young's modulus $E_{tip} \sim$ 169 GPa) characterized by $f_{0,1}$ = 16.35 kHz, $k_1 = 0.324$ N m^{-1}, Q_1 = 68, $f_{0,2}$ = 102.98 kHz, $k_2 = 13.1$ N m^{-1}, $Q_2 = 208$, where Q_i is the Q factor of the i^{th} flexural mode in free space. The force constants were computed for k_1 from the theoretical formula $k_1 = \frac{Ewt^3}{4l^3}$ [2], where E, t, w and l are, respectively, the cantilever beam Young's modulus, thickness, width and length and for k_2 by using the relation $k_2 = 40.4k_1$ established by Rast et al. [38]. The thickness t =2.35 μm was determined from $f_{0,1}$ and the formula $t \sim 6.1911(\frac{\rho}{E})^{\frac{1}{2}} f_{0,1} l^2$ [2]. The cantilever width w =52 μm and length l = 445 μm were determined by optical microscopy. The values E = 169 GPa and ρ = 2,330 kg m^{-3} were taken for the Young's modulus of the silicon beam and its mass density. The measured normal force $F_{N,meas}$ that corresponds to the vertical deflection of the cantilever and gives the value of the applied normal force F_N on the sample surface was calibrated with a factor obtained by dividing the cantilever spring constant by the cantilever optical sensitivity S_z. The optical sensitivity of value 229 nm V^{-1} was determined by measuring a vertical deflection-distance curve on an n-type silicon(111) sample of electrical resistivity = 10 Ω m and by taking the inverse of the slope. The two first flexural modes of the cantilever in contact were excited with the amplitudes A_1 = 22 mV and A_2 = 5 mV for all samples.

Samples and measurement conditions

Three different polymers, i.e., PS, PP and LLDPE and a self-assembled monolayer (SAM) of FDTS on a silicon oxide (SiOx) substrate were investigated. The SAM was prepared with circular holes obtained by polymer blend lithography (PBL) [35]. A reference sample consisting of PTFE, with a nominal Young's modulus of 500 MPa was used to determine parameter $\alpha(A_1)$. The measurements were performed in nondry air with a relative humidity of 36% and an ambient temperature of 27 °C.

6.2.3 Results and Discussion

Force-displacement and frequency shift-displacement curves

Before starting the investigation of sample elasticity, a force-displacement curve and a frequency shift-displacement curve (figures 61 and 62, left) for both flexural modes were recorded for each sample to determine for which F_N values the relation between Δf_1 and Δf_2^2 is linear and compute parameter $\alpha(A_1)$. The measured applied normal force $F_{N,meas}$ and frequency shifts Δf_1, Δf_2 were recorded for a displacement of the piezoelectric scanner in the normal direction Z from 0 to 350 nm. To measure the curves, the cantilever tip first indented the sample to a depth corresponding to a displacement of the Z scanner of 350 nm and both PLLs were then switched on. The curves were recorded during retraction of the tip in order to avoid unlocking the PLLs, which would happen if the tip indented the sample from a starting position out of contact, as contact resonances are quite far from those in free space. On the frequency shift-displacement curves, we observe a nonlinear relation between the measured frequency shifts, Δf_1 and Δf_2, and the displacement of the scanner, followed by a linear one. This suggests a plastic deformation phase of the sample surface during the first step of the indentation, followed by an elastic deformation phase. Both subsequent phases are explained by the evolution of stress during the indentation, as explained in subsection 6.1.2.

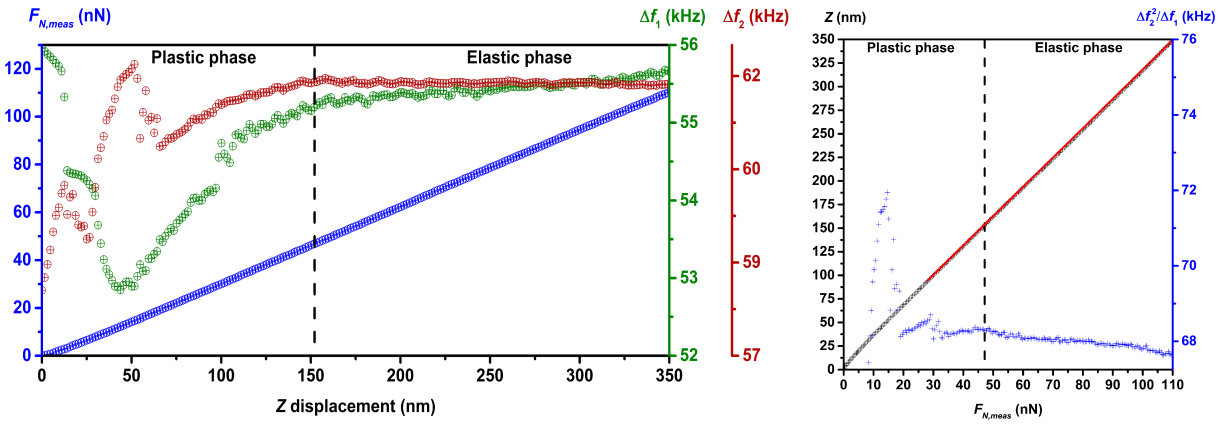

Figure 61: Left : Force-displacement and frequency shift-displacement curves of PTFE. The Δf_1(Z displacement) and Δf_2(Z displacement) curves evidence the existence of a plastic deformation phase followed by an elastic one. Right : the fitting of the $Z(F_{N,meas})$ curve gave a value close to the cantilever spring constant showing the exceedingly high compliance of the cantilever. The $\Delta f_2^2/\Delta f_1(F_{N,meas})$ curve shows the quasi-invariance of the $\Delta f_2^2/\Delta f_1$ ratio in the elastic phase and in the highest region of the plastic phase. Parameter $\alpha(A_1)$ determined by dividing the nominal value of the elasticity of the reference sample by the mean value of the ratio in the elastic phase gave a value of 7,355 Pa Hz^{-1}.

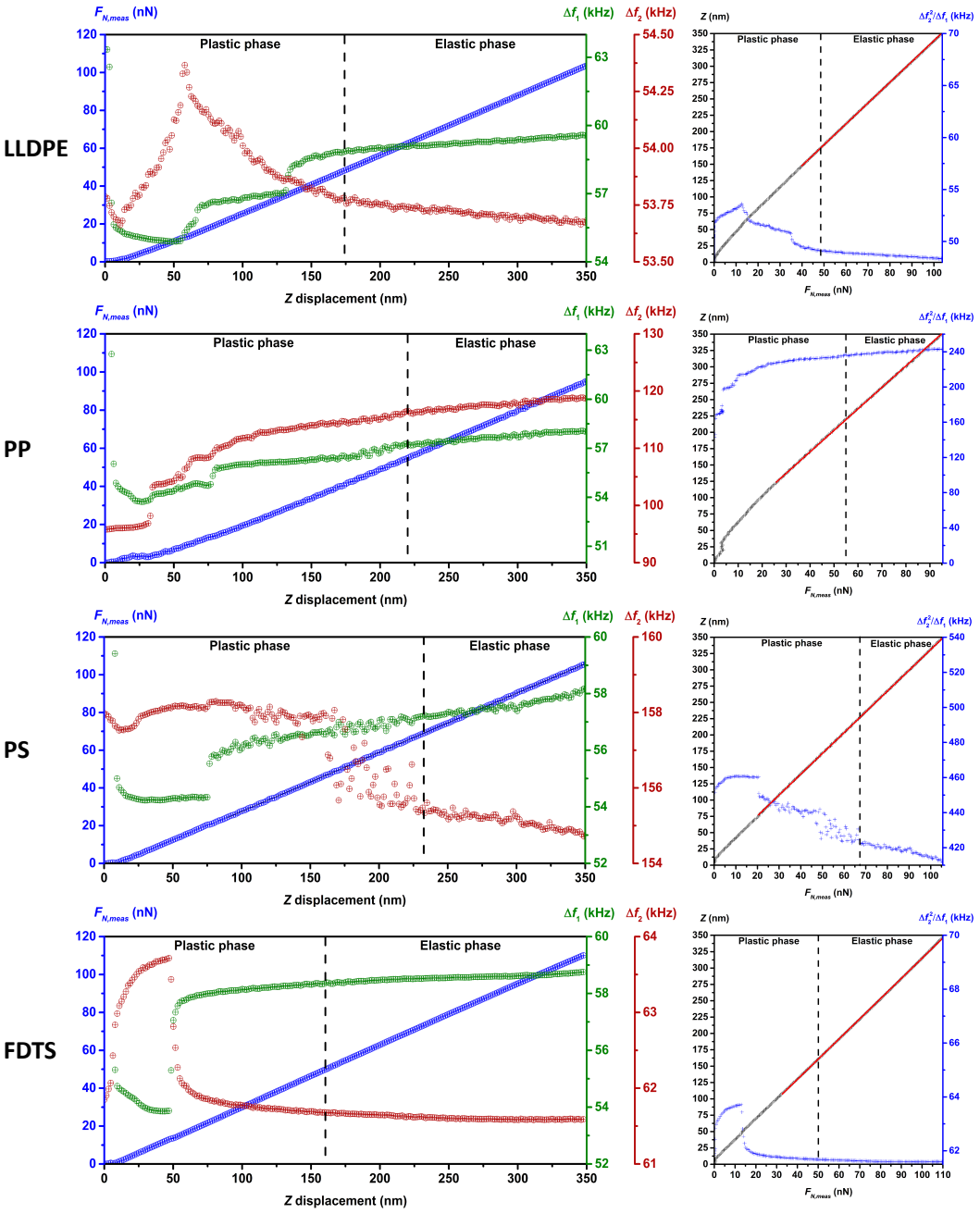

Figure 62: Left : Force-displacement and frequency shift-displacement curves of LLDPE, PP, PS and FDTS for the determination of the minimal normal force F_N used as setpoint for the elasticity measurements. The Δf_1(Z displacement) and Δf_2(Z displacement) curves evidence the existence of a plastic deformation phase followed by an elastic one. Right : Fitting of the $Z(F_{N,meas})$ curves gave a value close to the cantilever spring constant showing the exceedingly high compliance of the cantilever. The $\Delta f_2^2/\Delta f_1(F_{N,meas})$ curves show the quasi-invariance of the $\Delta f_2^2/\Delta f_1$ ratio in the elastic phase and in the highest region of the plastic phase.

Analysis of the force-displacement curves evidences the same relations with, however, a linear relation in the nonlinear domain of the frequency shift-displacement curves. This effect is due the too low spring constant of the cantilever compared with the normal stiffness of the samples from a certain Z displacement value and can be explained by modelling the cantilever tip in contact with the sample surface with two springs in a series, k_1 and $k_{sample,norm}$, the spring constant of the cantilever and the normal sample stiffness (of constant value in the elastic phase), respectively, as illustrated in figure 58a. As seen in figure 58b, the normal sample stiffness increases during indentation and the value of k_{eff} tends to k_1, so that beyond a certain value of $k_{sample,norm}$, the variation of $k_{sample,norm}$ cannot be observed anymore in the $F_{N,meas}(Z)$ curve. This assumption is confirmed from the fitting of the linear regions for each sample in table 3.

Sample	Inverse of slope (N m^{-1})
LLDPE	0.315
PP	0.308
PS	0.313
FDTS	0.324
PTFE	0.320

Table 3: Value of the inverse of the fitting curve slope of $Z(F_{N,meas})$ for measured samples in figures 61 and 62 (right). The values are close to the cantilever spring constant.

Linearity between Δf_1 and Δf_2^2 and determination of $\alpha(A_1)$

The linearity of the relation between Δf_1 and Δf_2^2 is shown in figures 61 and 62 (curves on the right) where the quasi-invariance of ratio $\Delta f_2^2/\Delta f_1$ in the elastic phase and in the upper part of the plastic phase can be observed. The mean value of the linear coefficient for each sample and the corresponding maximum deviation in percent in the elastic phase and the upper part of the plastic phase are reported in table 4. The small deviation in the upper part of the plastic phase suggests that setpoints for F_N in this region can be used to investigate sample elasticity. Parameter $\alpha(A_1)$ was determined by dividing the nominal value of Young's modulus of PTFE by the mean value of $\Delta f_2^2/\Delta f_1$ of PTFE. The computation yields a value of 7,355 Pa Hz^{-1}.

Sample	Mean $\Delta f_2^2/\Delta f_1$ (Hz)	Max. dev. elastic phase (%)	Max. dev. plastic phase (%)
LLDPE	48,720	0.89	3
PP	239,738	1.77	5
PS	417,224	1.38	6.7
FDTS	61,614	0.1	0.8
PTFE	67,981	0.52	1

Table 4: Mean value of $\Delta f_2^2/\Delta f_1$ and corresponding maximum deviation (%) in the elastic phase and the highest region in the plastic phase for measured samples.

Investigation of sample elastic modulus

Sample elastic modulus was then investigated with setpoints of the main feedback in the highest region of the plastic phase of 44.4 nN for LLDPE, 29.6 nN for PP, 29.6 nN for PS and 37 nN for FDTS. The results of the scannings are shown in figures 63 and 64 for topography (a) and elastic modulus (b). The histograms in (c) correspond to the distribution of elastic modulus for each map in (b). Polymers being viscoelastic materials, the elastic modulus $E_{eff,meas}$ measured on the investigated samples in dynamic mode corresponds to the storage modulus. As the measured contact resonances are quite large compared with the inverse of typical material relaxation time, we can assume that the measured storage modulus is frequency independent. Measurements showed values included in the range of Young's moduli for bulk materials for LLDPE, PP and PS, as shown in table 5. The investigation also evidenced regions of different elastic moduli, as illustrated in the histograms of LLDPE, PP and the SAM: LLDPE shows three different peaks centered at 362 MPa, 380 MPa and 393 MPa, PP two peaks centered at 1.468 GPa and 1.565 GPa and the SAM two peaks centered at 472 MPa and 478.5 MPa. Finally, the value of storage modulus of FDTS gives an order of magnitude of Young's modulus of FDTS monolayer.

Sample	$\boldsymbol{E_{eff,meas.}}$ (GPa)	$\boldsymbol{E_{sample,lit.}}$ (GPa)
LLDPE	0.362 $\pm$ 0.004, 0.38 $\pm$ 0.004, 0.393 $\pm$ 0.005	0.3$-$0.7 [39]
PP	1.468 $\pm$ 0.009, 1.565 $\pm$ 0.015	0.896$-$1.55 [40]
PS	3.21 $\pm$ 0.02	2.3$-$4.1 [37]
FDTS	0.4785 $\pm$ 0.0005	

Table 5: Measured storage moduli $E_{eff,meas}$ and values for Young's modulus of bulk materials from the literature $E_{sample,lit}$ on LLDPE, PP, PS and FDTS. $E_{eff,meas}$ values are included in the range of Young's moduli for bulk materials. For FDTS no literature value is available.

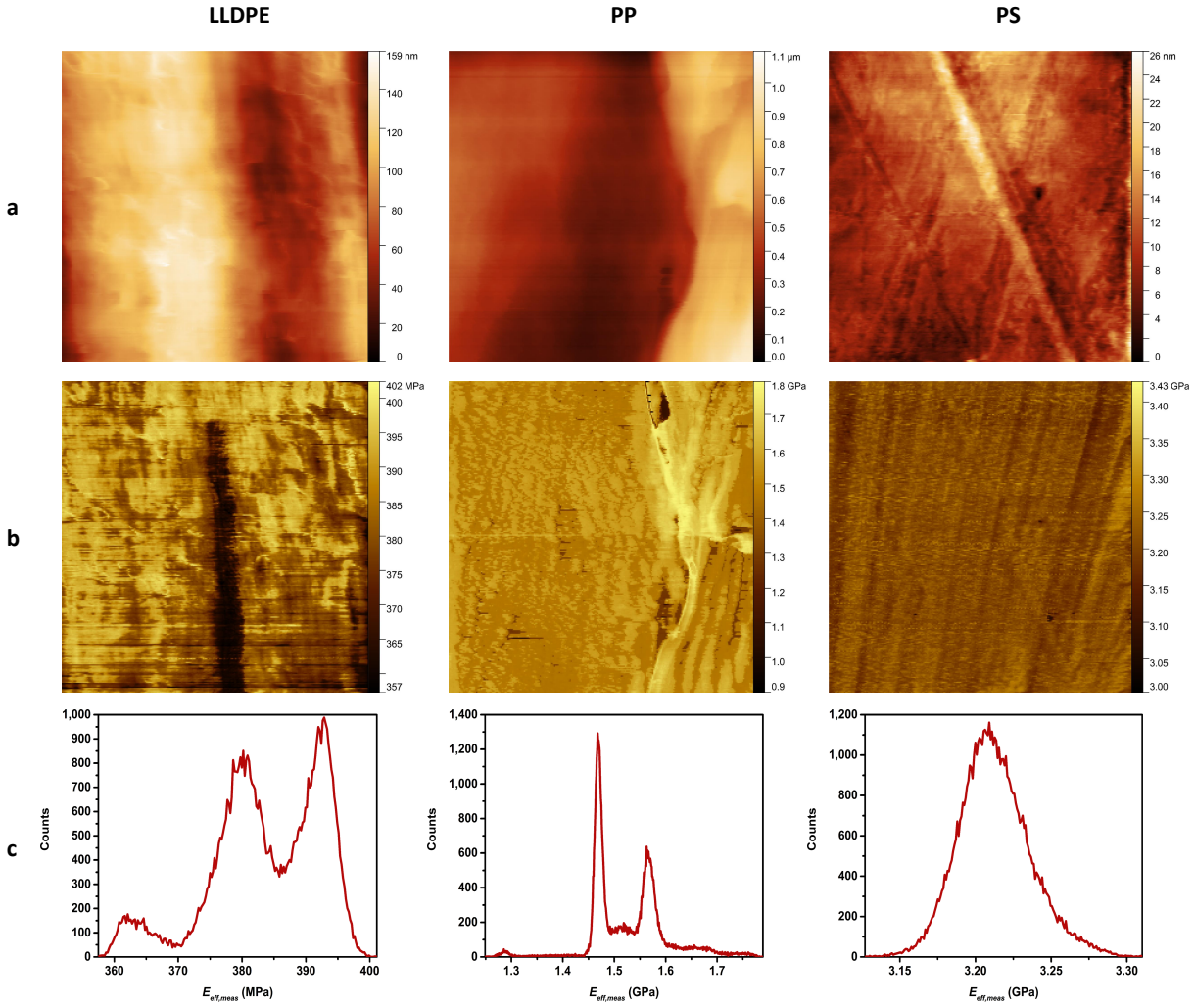

Figure 63: Mapping of topography (**a**) and elastic modulus (**b**) of 2.5 μm x 2.5 μm surfaces of LLDPE, PP and PS samples. The measurements were performed in contact by applying a constant normal force F_N of 44.4 nN for LLDPE and 29.6 nN for PP and PS, and by exciting the two first flexural modes of the cantilever with an amplitude of $A_1 = 22$ mV and $A_2 = 5$ mV respectively for the first and second mode. Histograms in **c** show the distribution of elastic modulus $E_{eff,meas}$ in the maps in **b**.

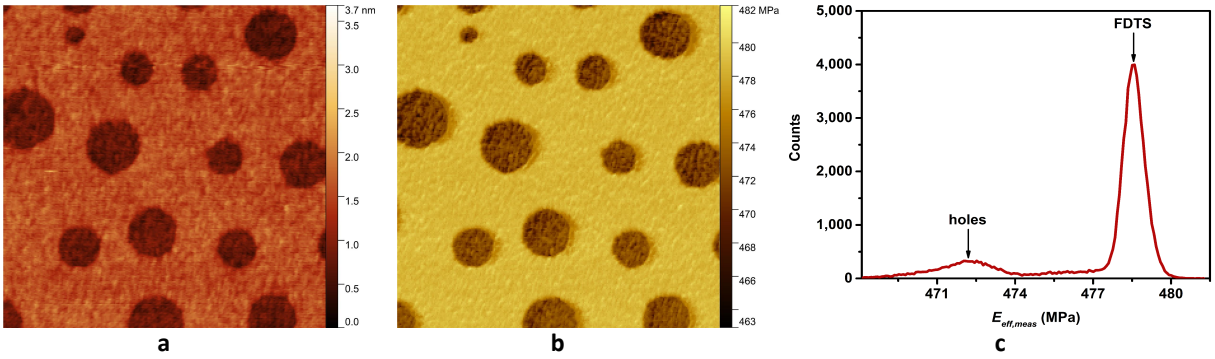

Figure 64: Mapping of topography (**a**) and elastic modulus (**b**) of 2.5 μm x 2.5 μm surface of the FDTS + SiOx SAM sample. The measurements were performed in contact by applying a constant normal force F_N of 37 nN, and by exciting the two first flexural modes of the cantilever with an amplitude of $A_1 = 22$ mV and $A_2 = 5$ mV respectively for the first and second mode. Histogram in **c** shows the distribution of elastic modulus $E_{eff,meas}$ in **b**.

Effect of tip functionalization on the SiOx elasticity peak of the SAM sample

The proximity of the peaks for FDTS and SiOx holes whereas we would expect two far distant ones can be explained by the fact that during scanning, some material of FDTS has formed around the tip, so that the relatively soft FDTS-coating of the tip is sensed (see also figure 65). The effect of collecting Teflon-like molecules with AFM tips has been known for a long time. It has been successfully used for the topographic imaging of the Si(111) surface with atomic resolution. Howald et al. [41] studied the Si(111)7 x 7 reconstruction in UHV by contact force microscopy. They observed adhesive forces of up to 103 nN between the Si tip and the Si(111) surface. By coating the tip with PTFE (Teflon), they could reduce the sticking forces to 10 nN. A short scan on a PTFE sample led to a reliable coating of the tip for the subsequent AFM scan on silicon. Since our sample consists of a perforated Teflon-like monolayer, the cantilever tip is most likely constantly functionalized with a thin layer of FDTS. This leads to the observed soft elasticity in- and outside the holes. The stability of this functionalization during the scan can be verified with topographic images. The holes show a depth slightly below 1.2 nm, which is the height of the FDTS monolayer, as seen in figure 65. If the tip coating were worn off, during the scan, larger holes would appear at least partially deeper.

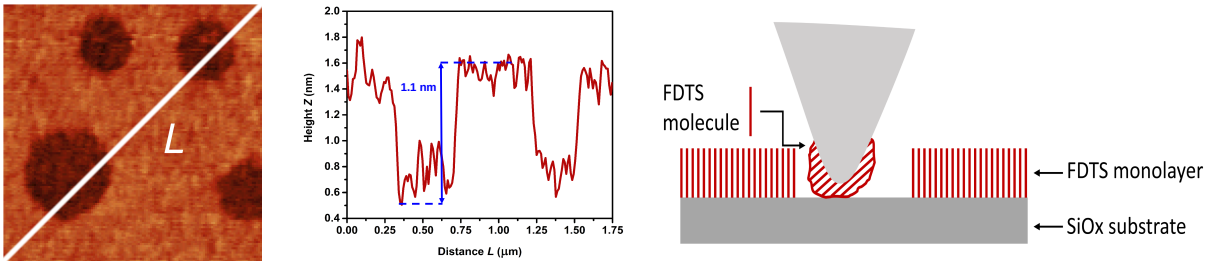

Figure 65: Line profile of the SiOx holes in the topographical mapping of the SAM showing their relative height and width due to the functionalization of the cantilever tip with FDTS material. On the right, a schematic of the tip-sample interaction is depicted. Loosley bond FDTS molecules are able to migrate to the AFM tip and can therefore functionalize it by the build-up of a thin layer of FDTS on the tip apex.

Conclusion

The aim of the present work was to investigate the elasticity of polymers by AFM. Four different polymers, namely LLDPE, PP, PS and PTFE, and a self-assembled monolayer of FDTS on a silicon oxide substrate perforated with circular holes prepared by polymer blend lithography [35] were investigated. Two measuring methods were used for this purpose, a static method, based on Oliver and Pharr's [25], [30] method for measuring the elasticity of samples with rigid indenters, and a dynamic method based on the work of Herruzo et al. [11]. In the static method, load-displacement curves were recorded to determine the parameters necessary to compute the elasticity of the samples in Oliver and Pharr's mathematical model. The load-displacement curves were recorded by indenting the cantilever tip in the sample through the displacement of the Z scanner and recording the vertical deflection of the cantilever corresponding to the applied load. The measurements evidenced the existence of a plastic deformation phase characterized by a nonlinear relation between the displacement of the Z scanner and the load, and an elastic deformation phase characterized by a linear relation between the displacement of the Z scanner and the load. The existence of these phases is explained by the evolution of stress σ (ratio of the applied load to the cross-section A of the cantilever tip) during indentation of the sample surface by the cantilever tip. The plastic phase starts when sufficient stress is applied to the surface. The slow increase in tip cross-section A compared to the applied load results in an increase in stress σ and a plastic deformation of the sample surface. The geometric shape of the tip, assumed to be pyramidal, results in a fast increase in tip cross-section compared with the increase in applied load when the tip goes deeper into the surface, which decreases the stress. When the decrease in stress is inferior to a threshold value, the surface starts to deform elastically and an elastic phase appears. The first recorded loading/unloading-displacement curves showed that by setting a delay before recording an unloading-displacement curve the slope of the unloading-displacement curve tends to the slope of the loading-displacement curve in the elastic deformation phase. By allowing a delay, we can also observe a shift ΔL between the maximum loads of loading/unloading-displacement curves. This shift is explained by different factors such as cold flow, thermal expansion and piezo creep. The necessary time to obtain the same slope for both curves was estimated by recording a ΔL curve as a function of the delay. We can observe that the delay reaches a constant value after a certain time. The determined minimum time was used to record the load-displacement curves of the samples. The curves were adapted to match their linear area and determine the parameters h_{max}, P_{max} and the normal sample stiffness $k_{sample,norm}$ required by the mathematical model of Oliver and Pharr. Parameters h_{max} and P_{max} were set as the length of the plastic deformation phase and the associated maximum load. The normal sample stiffness $k_{sample,norm}$ could not be determined by the fitting of the unloading-displacement curve by the power law defined in Oliver and Pharr's method because fitting and unloading-displacement curves did not fit. Instead, $k_{sample,norm}$ was determined from the slope of the loading curve by modelizing the cantilever

tip in contact with the sample surface by two springs in a series, k_1 and $k_{sample,norm}$, respectively, the spring constant of the cantilever and normal sample stiffness. The equivalent stiffness corresponds to the slope of the linear fit k_{eff} so that $k_{sample,norm}$ can be determined by $k_{sample,norm} = k_1 k_{eff}/(k_1 - k_{eff})$. For PS, three different fittings of the slope yield three values for k_{eff} with a variation of approximately 0.4% between the first and the third value. However, this small variation results in a difference of 27% in the computed values for $k_{sample,norm}$. This large variation is explained by the fact that the denominator in the formula for $k_{sample,norm}$ computation is close to 0 because the values for k_{eff} are close to the cantilever spring constant k_1. This effect shows that the method is highly dependent on the stiffness of the cantilevers and that stiffer cantilevers should be prefered when measuring on PS and harder samples with this method. Computation of the elastic modulus from the computed $k_{sample,norm}$ showed values in good accordance with Young's moduli of bulk materials published in the literature $E_{sample,lit}$ on PTFE and PS as shown in the table below;

Sample	$\boldsymbol{E_{sample,meas.}}$ (GPa)	$\boldsymbol{E_{sample,lit.}}$ (GPa)
PTFE	0.499	0.3−0.8 [36]
PS	2.59; 2.88; 3.58	2.3−4.1 [37]

In the dynamic method, we present a robust method for the quantitative determination of local sample elastic-modulus under ambient conditions (humidity, temperature). It combines the simplicity of the theoretical model developed by Herruzo et al. [11] for the determination of sample elasticity from 1 MPa to 3 GPa with a robust measuring method based on contact resonances. The measurements consist in tracking the first and second flexural contact resonances of the cantilever to determine the frequency shifts Δf_1 and Δf_2 relative to the corresponding resonances in free space in order to compute the elastic modulus. The linearity of the relation between Δf_1 and Δf_2^2 established in Herruzo et al. can be determined from the measurement of Δf_1 and Δf_2 as a function of the Z piezoelectric scanner displacement curves. These curves were measured on four polymers, i.e. LLDPE, PP, PS, PTFE and a Teflon-like fluorinated SAM. Analysis of the $\Delta f_2^2/\Delta f_1(F_{N,meas})$ curve showed that setpoints for the applied normal force in the highest region of the plastic phase could be used without causing a large deviation in the elasticity compared with the results we would obtain in the elastic phase. The elasticity of LLDPE, PP, PS and the studied SAM was then investigated. As polymers are viscoelastic materials, the elastic modulus $E_{eff,meas}$ measured in dynamic mode corresponds to the storage modulus. We assumed a frequency independence of the measured storage modulus as the measured contact resonances are quite large compared to the inverse of typical material relaxation time. The measurements showed values for the storage modulus within the range of Young's moduli for bulk materials for LLDPE, PP and PS as shown in table below;

Sample	$\boldsymbol{E_{eff,meas.}}$ (GPa)	$\boldsymbol{E_{sample,lit.}}$ (GPa)
LLDPE	0.362 $\pm$ 0.004, 0.38 $\pm$ 0.004, 0.393 $\pm$ 0.005	0.3−0.7 [39]
PP	1.468 $\pm$ 0.009, 1.565 $\pm$ 0.015	0.896−1.55 [40]
PS	3.21 $\pm$ 0.02	2.3−4.1 [37]
FDTS	0.4785 $\pm$ 0.0005	

The method can also distinguish the variations in surface elasticity as for LLDPE, PP and the studied SAM where different peaks were observed for the same sample. The investigated SAM

is a monolayer of FDTS patterned with circular 1:2-nm-deep holes by PBL. Due to the functionalization of the cantilever tip by SAM molecules, a comparable stiffness is measured inside and outside the holes. Finally, the measured value of the storage modulus of 478.5 $\pm$ 0.5 MPa is close to the value for bulk fluorinated materials such as PTFE (500 MPa) and can thus be used as an estimation for the order of magnitude of Young's modulus of FDTS monolayers. The measurements of the quantities required for the static method were performed with the SPM controller SAPHYR developed from a common project jointly devised by the Nanolino group of the Department of Physics of the University of Basel (Switzerland) and Nanosurf, based in Liestal (Switzerland) and specialized in SPM. The controller embeds different devices, called modules, for the generation, conditioning and treatment of signals such as PLLs, lockin amplifiers, PI controllers and a Subharmonic module for the generation of user defined periodic pulse signals. A full software for the stearing of the modules of SAPHYR and for performing experiments was developed in the LabVIEW environment. In the PLL UI, the PLL module can be used in lockin amplifier or PLL mode. The Subharmonics UI enables the setting of the values of the parameters characterizing the pulses. The Z controller UI enables the recording of sample topography in contact, intermittent contact and noncontact mode by using a Math submodule. The scan UI enables the mapping of the topography and other quantities such as the oscillation amplitude or the phase shift of the cantilever by generating the voltages necessary to the X and Y scanners to move the tip. A Z spectroscopy interface was developed to enable the recording of quantities as a function of the Z scanner displacement. In addition, a delay can be set before the recording of the unload-displacement curve as required in the above description. Moreover, by moving cursors on the graph where the load-displacement curves are displayed, parameters h_{max}, P_{max} can be determined and the normal sample stiffness $k_{sample,norm}$ computed by an integrated fitting function; the mathematical model of Oliver and Pharr [25], [30] was implemented in the UI to enable the computation of the elastic modulus from the determined parameters. Finally, the initial method for the computation of phase shifts between an excitation signal and the cantilever response signal with SAPHYR lockin amplifiers was replaced by a more powerful algorithm that I developed. In the initial method, the phase shift was determined from the real-time computation of ratio $\frac{Y}{X}$ of the quadrature Y to the in-phase X components in SAPHYR controller and the computation of $arctan(\frac{Y}{X})$ by the software for the control of SAPHYR. This algorithm can now compute $arctan(\frac{Y}{X})$ directly and precisely in the SAPHYR lockin amplifiers in real time. In addition, the algorithm overcomes the instabilities of the functioning of the initial PLLs in SAPHYR based on the use of the approximation $arctan(\frac{Y}{X}) \simeq \frac{Y}{X}$ as a phase shift value, and due to magnitudes of phase shift and its variations greater than $0°$, that occur, for example, when the cantilever tip picks up material or the elastic properties of the sample surface change. Since this algorithm shows great potential, especially in the SPM domain, I proposed to patent it. Prof. Ernst Meyer, from the University of Basel, and Dr. Wolfgang Henggeler, from Unitectra, agreed. My invention was officially received by the European Patent Office and registered on July 24, 2015.

Bibliography

[1] E. Meyer. Atomic force microscopy. *Prog. Surf. Sci.*, 41:3–49, 1992.

[2] E. Meyer, T. Gyalog, R. M. Overney, and K. Dransfeld, editors. World Scientific Publishing: Singapore, 1998.

[3] F. J. Giessibl. Advances in atomic force microscopy. *Rev. Mod. Phys.*, 75:949–983, 2003.

[4] W. A. Hofer, A. S. Foster, and Schluger A. L. Theories of scanning probe microscopes at the atomic scale. *Rev. Mod. Phys.*, 75:1297–1331, 2003.

[5] S. Kasas and G. Dietler. Probing the nanomechanical properties of viruses, cells and cellular structures. In Y. Dufrêne, editor, *Life at the Nanoscale: Atomic Force Microscopy of Live Cells*, pages 335–352. Pan Stanford Publishing, Singapore, 2011.

[6] S. Dai, J. Zhao, M. He, X. Wang, J. Wan, Z. Shan, and J. Zhu. Elastic properties of GaN nanowires: revealing the influence of planar defects on Young's modulus at nanoscale. *Nano. Lett.*, 15:8–15, 2015.

[7] H. Lu and X. Meng. Correlation between band gap, dielectric constant, Young's modulus and melting temperature of GaN nanocrystals and their size and shape dependences. *Sci. Rep.*, 5:16939, 2015.

[8] G. Binnig, C. F. Quate, and C. Gerber. Atomic force microscope. *Phys. Rev. Lett.*, 56:930–934, 1986.

[9] J. Tamayo and R. Garcia. Effects of elastic and inelastic interactions on phase contrast images in tapping-mode scanning force microscopy. *Appl. Phys. Lett.*, 71:2394–2396, 1997.

[10] D. C. Hurley and J. A. Turner. Measurement of Poisson's ratio with contact-resonance atomic force microscopy. *J. Appl. Phys.*, 102:033509, 2007.

[11] E. T. Herruzo, A. P. Perrino, and R. Garcia. Fast nanomechanical spectroscopy of soft matter. *Nat. Commun.*, 5:3126, 2014.

[12] U. Rabe. Atomic force acoustic microscopy. In B. Bhushan and H. Fuchs, editors, *Applied Scanning Probe Methods II*, pages 37–90. Springer, Berlin, Heidelberg, Germany, 2006.

[13] U. Rabe, J. A. Turner, and W. Arnold. Analysis of the high-frequency response of atomic force microscope cantilevers. *Appl. Phys. A*, 66:277–282, 1998.

[14] U. Rabe and W. Arnold. Acoustic microscopy by atomic force microscopy. *Appl. Phys. Lett.*, 64:1493–1495, 1994.

[15] U. Rabe, S. Amelio, E. Kester, V. Scherer, S. Hirsekorn, and W. Arnold. Quantitative determination of contact stiffness using atomic force acoustic microscopy. In *Ultrasonics*, volume 38, pages 430–437. Elsevier, 2000.

[16] U. Rabe, S. Amelio, M. Kopycinska, S. Hirsekorn, M. Kempf, M. Göken, and W. Arnold. Imaging and measurement of local mechanical material properties by atomic force acoustic microscopy. *Surf. Int. Analys.*, 33:65–70, 2002.

[17] U. Rabe, M. Kopycinska-Müller, and S. Hirsekorn. Atomic force acoustic microscopy. In F. Marinello, D. Passeri, and E. Savio, editors, *Acoustic Scanning Probe Microscopy*, pages 123–153. Springer, Berlin, Heidelberg, Germany, 2012.

[18] J. R. Lozano and R. Garcia. Theory of multifrequency atomic force microscopy. *Phys. Rev. Lett.*, 100:0761021–0761024, 2008.

[19] R. Garcia and E. T. Herruzo. The emergence of multifrequency force microscopy. *Nat. Nanotechnol.*, 7:217–226, 2012.

[20] T. R. Rodriguez and R. Garcia. Compositional mapping of surfaces in atomic force microscopy by excitation of the second normal mode of the microcantilever. *Appl. Phys. Lett.*, 84:449–451, 2004.

[21] R. Proksch. Multifrequency, repulsive-mode amplitude-modulated atomic force microscopy. *Appl. Phys. Lett.*, 89:113121, 2006.

[22] N. F. Martinez, J. R. Lozano, E. T. Herruzo, F. Garcia, C. Richter, T. Sulzbach, and R. Garcia. Bimodal atomic force microscopy imaging of isolated antibodies in air and liquids. *Appl. Phys. Lett.*, 19:384011, 2008.

[23] E. T. Herruzo and R. Garcia. Theoretical study of the frequency shift in bimodal FM-AFM by fractional calculus. *Beilstein J. Nanotechnol.*, 3:198–206, 2012.

[24] R. Garcia and R. Proksch. Nanomechanical mapping of soft matter by bimodal force microscopy. *Eur. Polym. J.*, 49:1897–1906, 2013.

[25] W. C. Oliver and G. M. Pharr. An improved technique for determining hardness and elastic modulus using load and displacement sensing indentation experiments. *J. Mater. Res.*, 7:1564–1583, 1992.

[26] G. Binnig and H. Rohrer. Scanning tunneling microscopy. *Helv. Phys. Acta*, 55:726–735, 1982.

[27] G. Binnig, H. Rohrer, C. Gerber, and Weibel. E. Surface studies by scanning tunneling microscopy. *Phys. Rev. Lett.*, 49:57–60, 1982.

[28] F. J. Giessibl. Atomic resolution of the silicon (111)-(7x7) surface by atomic force microscopy. *Science*, 267:68–71, 1995.

[29] M. F. Doerner and W. D. Nix. A method for interpreting the data from depth-sensing indentation instruments. *J. Mater. Res.*, 1:601–609, 1986.

[30] W. C. Oliver and G. M. Pharr. Measurement of hardness and elastic modulus by instrumented indentation: Advances in understanding and refinements to methodology. *J. Mater. Res.*, 19:3–20, 2004.

[31] F. J. Giessibl. Forces and frequency shifts in atomic-resolution dynamic-force microscopy. *Phys. Rev. B*, 56:16010, 1997.

[32] S. Kawai, T Glatzel, S. Koch, B. Such, A. Baratoff, and E. Meyer. Systematic achievement of improved atomic-scale contrast via bimodal dynamic force microscopy. *Phys. Rev. Lett.*, 103:220801, 2009.

[33] B. C. Stipe, H. J. Mamin, C. S. Yannoni, T. D. Stowe, T. W. Kenny, and D. Rugar. Electron spin relaxation near a micron-size ferromagnet. *Phys. Rev. Lett.*, 87:277602, 2001.

[34] T. Fukuma and J. I. Kilpatrick. Phase-modulation atomic-force microscope with true atomic resolution. *Rev. Sci. Instrum.*, 77:123703, 2006.

[35] C. Huang, M. Moosmann, J. Jin, T. Heiler, S. Walheim, and T. Schimmel. Polymer blend lithography: A versatile method to fabricate nanopatterned self-assembled monolayers. *Beilstein J. Nanotechnol.*, 3:620–628, 2012.

[36] Goodfellow webpage. PTFE material information. http://www.goodfellow.com/E/Polytetrafluoroethylene.html.

[37] Goodfellow webpage. Polystyrene material information. http://www.goodfellow.com/E/Polystyrene.html.

[38] S. Rast, C. Wattinger, U. Gysin, and E. Meyer. Dynamics of damped cantilevers. *Rev. Sci. Instr.*, 71:2772–2775, 2000.

[39] M. D. Lechner. Polymers. In W. Martienssen and H. Warlimont, editors, *Springer Handbook of Condensed Matter and Materials Data*, pages 477–522. Springer, Berlin, Heidelberg, Germany, 2005.

[40] Materials data book, 2003, Cambridge University Engineering Department, england.

[41] L. Howald, R. Lüthi, E. Meyer, and H. J. Güntherodt. Scanning force microscopy on the si(111)7 x 7 surface reconstruction. *J. Phys. B: Cond. Matter.*, 93:267–268, 1994.

List of Figures

List of Tables

Appendix A

Table of phase values from the computation of arctan function with the algorithm and computation software

X	*Y*	Phase from algorithm	Phase from algorithm in degrees	arctan2 in degrees
-32,767	0	-262,144	-179.999	180.00
-32,767	6	262,134	179.993	179.99
-32,767	57	262,002	179.902	179.90
-32,747	1,144	259,232	178.000	178.00
-32,269	5,690	247,580	170.000	170.00
-30,982	10,668	234,478	161.003	161.00
-28,675	15,856	219,998	151.061	151.06
-25,821	20,173	206,798	141.997	142.00
-21,497	24,730	190,786	131.002	131.00
-15,886	28,659	173,300	118.996	119.00
-11,486	30,688	160,950	110.516	110.52
-6,814	32,051	148,546	101.998	102.00
-572	32,763	132,526	90.998	91.00
0	32,767	131,082	90.007	90.00
2,673	32,658	124,268	85.328	85.32
9,361	31,401	106,898	73.401	73.40
16,135	28,519	88,112	60.502	60.50
21,049	25,112	72,868	50.034	50.03
23,170	23,170	65,534	44.999	45.00
27,481	17,846	48,054	32.996	33.00
29,934	13,328	34,958	24.004	24.00
32,269	5,690	14,564	10.000	10.00
32,631	2,987	7,618	5.231	5.23
32,762	572	1,454	0.998	1.00
32,767	0	0	0.000	0.00
32,747	-1,144	-2,912	-2.000	-2.00
31,650	-8,481	-21,844	-14.999	-15.00
30,162	-12,803	-33,492	-22.997	-23.00
28,377	-16,383	-43,694	-30.002	-30.00
24,331	-21,947	-61,240	-42.050	-42.05
18,375	-27,130	-81,388	-55.885	-55.89
14,866	-29,201	-91,776	-63.018	-63.02
10,668	-30,982	-103,406	-71.003	-71.00
57	-32,767	-130,930	-89.902	-89.90
0	-32,767	-131,072	-90.000	-90.00
-6	-32,767	-131,082	-90.007	-90.01
-6,252	-32,165	-147,092	-101.000	-101.00
-13,848	-29,697	-167,488	-115.005	-115.00
-17,856	-27,474	-179,166	-123.024	-123.02
-23,007	-23,331	-196,030	-134.603	-134.60
-26,165	-19,724	-208,244	-142.990	-142.99
-28,681	-15,845	-220,028	-151.081	-151.08
-32,075	-6,701	-244,966	-168.205	-168.20
-32,523	-3,993	-251,948	-172.999	-173.00
-32,645	-2,822	-254,954	-175.063	-175.06
-32,732	-1,515	-258,294	-177.356	-177.35
-32,747	-1,141	-259,242	-178.007	-178.01
-32,767	-6	-262,134	-179.993	-179.99
-32,767	0	-262,144	-179.999	-180.00

Figure 66: The table of phase values obtained by computation of arctan(Y/X) with the algorithm presented in chapter 4 and arctan2 function of Excel. The decimal values for X, Y and phase from algorithm in columns 1, 2 and 3 show the values corresponding to the binary values for the bit lengths used for SAPHYR, i.e. 16 for X and Y and 19 for the phase. The decimal value 32767 corresponds to the length of a unit vector and the value -262144 to a phase of -180°.

Appendix B

Acknowledgement of receipt of request for grant of a European patent for: ‘Algorithm for phase computation in lock-in technique’

Europäisches Patentamt
European Patent Office
Office européen des brevets

Acknowledgement of receipt

We hereby acknowledge receipt of your request for grant of a European patent as follows:

Submission number	3656523
Application number	EP15178389.1
File No. to be used for priority declarations	EP15178389
Date of receipt	24 July 2015
Your reference	uz242ep
Applicant	Universität Basel
Country	CH
Title	Algorithm for phase computation in lock-in technique
Documents submitted	package-data.xml application-body.xml SPECEPO-1.pdf\uz242ep_spec_claims_abs_figs2.pdf (69 p.) ep-request.xml ep-request.pdf (4 p.) f1002-1.pdf (1 p.)
Submitted by	CN=Ben Schulz 21083
Method of submission	Online
Date and time receipt generated	24 July 2015, 18:50 (CEST)
Message Digest	08:96:ED:2A:E2:FC:A9:F0:D8:D5:21:FF:E8:83:70:EE:54:DF:AD:B5

Correction by the EPO of errors in debit instructions filed by eOLF
Errors in debit instructions filed by eOLF that are caused by the editing of Form 1038E entries or the continued use of outdated

Appendix C

Name of the inventor

European Patent Office
80298 MUNICH
GERMANY

Questions about this communication ?
Contact Customer Services at www.epo.org/contact

BUBENDORF, Alexander
Universität Basel
12, rue des orèvres
F-68480 Sondersdorf
FRANCE

Date	16.09.15
Reference	
Application No./Patent No.	15178389.1 - 1954
Applicant/Proprietor	Universität Basel

Designation as inventor - communication under Rule 19(3) EPC

You have been designated as inventor in the above-mentioned European patent application. Below you will find the data contained in the designation of inventor and further data mentioned in Rule 143(1) EPC:

DATE OF FILING	: 24.07.15
PRIORITY	: / /
TITLE	: ALGORITHM FOR PHASE COMPUTATION IN LOCK-IN TECHNIQUE
DESIGNATED STATES	: AL AT BE BG CH CY CZ DE DK EE ES FI FR GB GR HR HU IE IS IT LI LT LU LV MC MK MT NL NO PL PT RO RS SE SI SK SM TR

INVENTOR (PUBLISHED = 1, NOT PUBLISHED = 0):

1/BUBENDORF, Alexander/Universität Basel 12, rue des orèvres/F-68480 Sondersdorf/FR
1/MEYER, Ernst/Universität Basel Apfhalterstr. 32/CH-4132 Muttenz/CH
1/GLATZEL, Thilo/Universität Basel Bützmattweg 49/D-79594 Inzlingen/DE

DECLARATION UNDER ARTICLE 81 EPC:
The applicant(s) has (have) acquired the right to the European patent as employer(s).

Receiving Section

EPO Form 1048 10.09

Appendix D

Analytical expression for normal sample stiffness

The following computation steps establish the analytical expression for normal sample stiffness. The formula is derived from the equations stated by Hurley and Turner [10] for the numerical determination of normal sample stiffness. These equations, i.e. equations (1), (2), (3), (4), (5), (6) and (7), are based on the description of the dynamics of a clamped, ideally beam-shaped cantilever elastically coupled to a sample by its tip, published by Rabe [12] and Rabe et al [13]. The model takes into account characteristics of the cantilever, such as tilt angle α and dimensions, namely total length L, length from the clamped end to the tip L_1, length from the tip to the free end L_2, tip height h, but also characteristics of the sample, i.e. normal sample stiffness $k_{sample,norm}$ and lateral sample stiffness $k_{sample,lat}$ represented by two springs

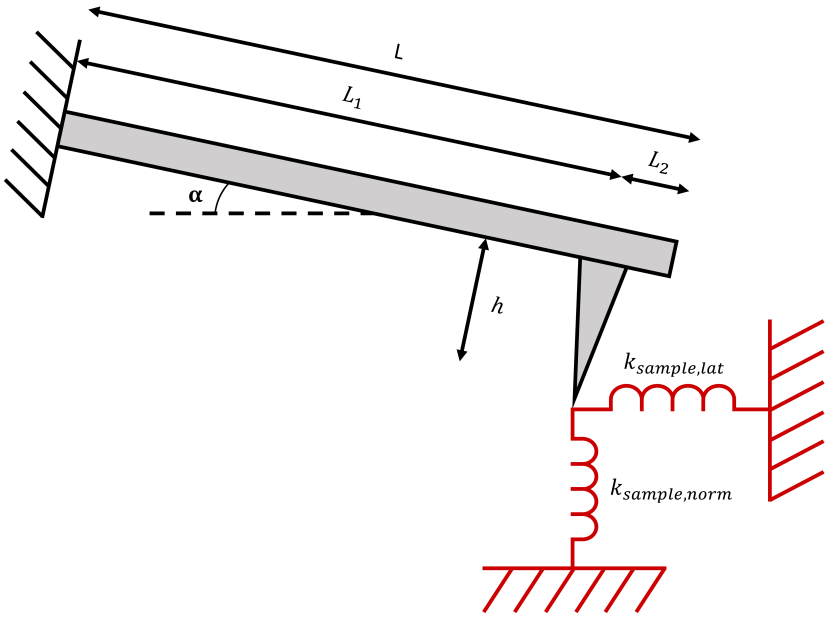

Figure 67: Modelization of clamped beam-shaped cantilever elastically coupled to a sample by its tip and used for the computation of normal sample stiffness. The cantilever characteristics, i.e. L, L_1, L_2, h and α correspond, respectively, to cantilever length, length from the clamped end to the tip, length from the tip to the free end, tip height and tilt angle. The springs $k_{sample,norm}$ and $k_{sample,lat}$ stand, respectively, for normal and lateral sample stiffnesses.

Wavenumbers x_n and y_n associated with the measured n^{th} flexural contact resonance f_n and torsional contact resonances t_n are computed by

$$x_n L = x_n^0 L \sqrt{\frac{f_n}{f_n^0}},$$

where f_n^0 is the cantilever resonance of n^{th} flexural mode in free space and x_n^0 the associated wavelength (values given in Rabe [12]) obtained from the resolution of the characteristic equation $cos(x_n L)cosh(x_n L) + 1 = 0$ and

$$y_n = \frac{(2n-1)\pi}{2}\frac{t_n}{t_n^0},$$

where t_n^0 is the cantilever resonance of n^{th} torsional mode in free space.

The normalized lateral contact stiffness is determined by

$$k_{sample,lat} = -\frac{y_n L cos(y_n L)}{sin(y_n L_1)cos(y_n L_2)}k_{lat},$$

where k_{lat} is the lateral cantilever stiffness constant.

The normal contact stiffness normalized with the cantilever flexural stiffness constant k_1 is obtained from the expression

$$\frac{k_{sample,norm}}{k_1} = \frac{-B \pm \sqrt{B^2 - 4AC}}{6A}, \tag{1}$$

where the positive root corresponds to the normalized contact stiffness and parameters A, B and C are defined by

$$A = \frac{k_{sample,lat}}{k_{sample,norm}}A', \tag{2}$$

where

$$A' = \left(\frac{h}{L_1}\right)^2 \Big(1 - cos(x_n L_1)cosh(x_n L_1)\Big)\Big(1 + cos(x_n L_2)cosh(x_n L_2)\Big),$$

$$B = B_1 + B_2 + B_3, \tag{3}$$

with

$$B_1 = \left[sin^2(\alpha) + \left(\frac{k_{sample,lat}}{k_{sample,norm}}\right)cos^2(\alpha)\right]B_1', \tag{4}$$

where

$$B_1' = \left(\frac{h}{L_1}\right)^2 (x_n L_1)^3 \Bigg[\Big(1 + cos(x_n L_2)cosh(x_n L_2)\Big)\Big(sin(x_n L_1)cosh(x_n L_1) + cos(x_n L_1)sinh(x_n L_1)\Big)$$
$$- \Big(1 - cos(x_n L_1)cosh(x_n L_1)\Big)\Big(sin(x_n L_2)cosh(x_n L_2) + cos(x_n L_2)sinh(x_n L_2)\Big)\Bigg],$$

$$B_2 = \left[\left(\frac{k_{sample,lat}}{k_{sample,norm}} - 1\right)cos(\alpha)sin(\alpha)\right]B_2', \tag{5}$$

where

$$B_2^{'} = 2\left(\frac{h}{L_1}\right)(x_n L_1)^2\Big[\Big(1 + cos(x_n L_2)cosh(x_n L_2)\Big)sin(x_n L_1)sinh(x_n L_1) + \Big(1 - cos(x_n L_1)cosh(x_n L_1)\Big)sin(x_n L_2)sinh(x_n L_2)\Big],$$

$$B_3 = \left[cos^2(\alpha) + \left(\frac{k_{sample,lat}}{k_{sample,norm}}\right)sin^2(\alpha)\right]B_3^{'}, \tag{6}$$

where

$$B_3^{'} = x_n L_1\Big[\Big(1 + cos(x_n L_2)cosh(x_n L_2)\Big)\Big(sin(x_n L_1)cosh(x_n L_1) - cos(x_n L_1)sinh(x_n L_1)\Big) - \Big(1 - cos(x_n L_1)cosh(x_n L_1)\Big)\Big(sin(x_n L_2)cosh(x_n L_2) - cos(x_n L_2)sinh(x_n L_2)\Big)\Big],$$

and

$$C = 2(x_n L_1)^4(1 + cos(x_n L)cosh(x_n L)). \tag{7}$$

Parameter B can be split into two terms, one with $k_{sample,norm}$ and the other without;

$$B = \beta_1 + \beta_2\frac{k_{sample,lat}}{k_{sample,norm}},$$

with

$$\beta_1 = sin^2(\alpha)B_1^{'} - cos(\alpha)sin(\alpha)B_2^{'} + cos^2(\alpha)B_3^{'},$$

and

$$\beta_2 = cos^2(\alpha)B_1^{'} + cos(\alpha)sin(\alpha)B_2^{'} + sin^2(\alpha)B_3^{'}.$$

By setting a new variable ϵ of expression

$$\epsilon = 6A^{'}\frac{k_{sample,lat}}{k_1},$$

we can rewrite equation (1) as

$$\epsilon + B = \pm\sqrt{B^2 - 4AC}.$$

Finally, by squaring each side of the equation and isolating $k_{sample,norm}$, we find the following expression for the normal sample stiffness

$$\boxed{k_{sample,norm} = -\frac{2A^{'}C\epsilon^{-1} + \beta_2}{0.5\epsilon + \beta_1}k_{sample,lat}.}$$

List of publications

H. Bartolf; U. Gysin; H. R. Rossmann; A. Bubendorf; T. Glatzel; T. A. Jung; E. Meyer; M. Zimmermann; S. Reshanov; A. Schöner. Development of power semiconductors by quantitative nanoscale dopant imaging. *Power Semiconductor Devices & IC's*, 2015.

H. R. Rossmann; U. Gysin; A. Bubendorf; T. Glatzel; S. Reshanov; A. Schöner; T. A. Jung; E. Meyer; H. Bartolf. Two-dimensional carrier profiling on lightly doped n-type 4H-SiC epitaxially grown layers. *Material science forum*, 821-823: 269-272, 2015.

S. Kawai; C. M. Pina; A. Bubendorf; G. Fessler; T. Glatzel; E. Gnecco; E. Meyer. Systematic study of the dolomite (104) surface by bimodal dynamic force microscopy in ultra-high vacuum. *Nanotechnology*, 24:055702, 2013

Acknowledgements

I dedicate my thesis to my parents, my brother, my sister-in-law and my little god-daughter. I would like to thank them as well as my whole family and my friends for supporting me, encouraging me and staying loyal all these years. This thesis is not only the fruit of my own work: it is also the result of enriching human exchanges and the knowledge that others were willing to share with me, and to whom I would like to express my deep gratefulness. First and foremost, I would like to thank Professor Ernst Meyer, who accepted to integrate me in his group for my PhD research work and has trusted my work ever since the days I prepared my master thesis. I would also like to extend my thanks to the following persons: Professor Alexis Baratoff, whose advice on theoretical points has always been a great help to me, Professor Christoph Gerber for lending me his microscope, Dr. Shigeki Kawai, Dr. Sascha Koch and Dr. Markus Langer-Samadaschvili for improving my skills in AFM, and Dr. Stefan Walheim from the Karlsruhe Institute of Technology (Karlsruhe, Germany) for preparating the SAM sample and for his useful complementary information concerning my explanation of the similarity between the elasticity of FDTS and SiOx holes in the SAM. Many thanks also to Dr. Wolfgang Henggeler from Unitectra AG, Zurich, Switzerland, with whom I had the pleasure to develop my patent. I am also grateful to Werner Erni, Roberto Maffiolini, Michael Steinacher, Andreas Tonin and Christoph Werle from the Electronics Workshop for sharing their extensive knowledge of electronics with me. A thank to Astrid Kalt, Barbara Kammermann, Germaine Weaver and Bernd Heimann, members of the Administrative Staff of the Department of Physics, have always been very cooperative, many thanks to them. Special thanks as well to Beat Glatz for sorting out my computer problems more than once. Last but not least, I would like to thank my colleagues Dr. Sweetlana Fremy-Koch, Sarah Freund, Dr. Agata Krywko, Elçin Külah, Dr. Sylwia Nowakowska, Olia Popova, Marwa Ben Yaala, Dilek Yildiz, Dr Aneliia Wäckerlin, Dr. Baran Eren, Dr. Gregor Fessler, Dr. Gino Günzburger, Dr. Urs Gysin, Dr. Antoine Hinaut, Res Jöhr, Dr. Marcin Kisiel, Dr. Laurent Marot, Tobias Meier, Lucas Moser, Dr. Rémy Pawlak, Dr. Harald Rossmann, Mathias Schultzendorf, Dr. Pascal Steiner, Roland Steiner, Dr. Mathias Wasem, Dr. Marco Wisse and Dr. Thilo Glatzel for many helpful and enriching discussions over the years.